Adaptive High-Order Differential Formulation for the Compressible Navier-Stokes Equations

By

Lei Shi

Submitted to the Department of Aerospace Engineering and the
Graduate Faculty of the University of Kansas
in partial fulfillment of the requirements for the degree of
Doctor of Philosophy

Committee members

Dr. Z.J. Wang, Chairperson

Dr. Saeed Farokhi

Dr. Weizhang Huang

Dr. Ray Taghavi

Dr. Xuemin Tu

Dr. Zhongquan Zheng

Date Defended: Dec 05, 2014

The Thesis Committee for Lei Shi certifies
that this is the approved version of the following project proposal :

Adaptive High-Order Differential Formulation for the Compressible Navier-Stokes Equations

Dr. Z.J. Wang, Chairperson

Date approved: Dec 05, 2014

Abstract

High-order methods have the potential to achieve higher accuracy at lower cost than lower order methods. This potential has been demonstrated conclusively for smooth problems in the 1st International Workshop on High-Order Methods. For non-smooth problems, solution based hp-adaptations offer the best promise. Adjoint-based adaptive methods have the capability of dynamically distributing computing resources to areas which are important for predicting engineering performance parameters, such as lift or drag. This thesis presents a robust and efficient adjoint-based adaptive high-order differential formulation for the compressible Navier-Stokes equations, which can rapidly determine an accurate estimate of an engineering output within a prescribed error threshold.

The flux reconstruction (FR) or the correction procedure via reconstruction (CPR) method used in this work is a high-order differential formulation. We develop a parallel adjoint-based adaptive CPR solver which can work with any element-based error estimate and handle arbitrary discretization orders for mixed elements. First, a dual-consistent discrete form of the CPR method is derived. Then, an efficient and accurate adjoint-based error estimation method for the CPR method is developed and its accuracy and effectiveness are verified for the linear and non-linear partial differential equations (PDE). For anisotropic h-adaptations, we use a local output error sampling procedure to find the optimal refinement option. The current method has been applied to aerodynamic problems. Numerical tests show that significant savings in the number of DOFs can be achieved through the adjoint-based adaptation.

Contents

List of Figures

List of Tables

Chapter 1

Introduction

1.1 Background and Significance

With increased computational power and progress in numerical methods over the past several decades, Computational Fluid Dynamics (CFD) is used routinely as the main design tool in the design of aircraft to reduce design costs and improve the final product's performance. However, the current CFD tools cannot completely satisfy the requirements of accuracy, efficiency and robustness over the entire flight envelope. The typical use of CFD in the aerospace industry still relies heavily on the experience of the CFD users to generate grids and perform error assessment, which introduce uncertainties to the final results. In the 3^{rd} AIAA Drag Prediction Workshop, a mesh refinement study was performed to two families of meshes generated by NASA Langley and Cessna Aircraft Co. separately using their best engineering practices [77]. The difference of 7 drag counts was found from a $2nd$ order CFD solver between those two sets of meshes on the finest level, whose degree of freedom is 10 times more than a typical mesh commonly used for engineering problems in practice. A difference of 7 drag counts, i.e. 7×10^{-4}, is unacceptable for engineering purposes, which can be translated into approximately 4-8 passengers for a large passenger airliner by a range-equation analysis [31, 101]. A conclusion has been drawn in [77] that a 2nd order CFD

method with best-practice meshes cannot resolve the full range of length scales shown in the turbulent flow over relevant geometries. Efficiency and robustness requirements for the high-fidelity simulations present challenges for the current CFD methods.

The objective of this work is to develop a robust and efficient CFD solver for compressible Navier-Stokes equations that can provide reliable prediction of the design parameters of interests within the engineering accuracy. A robust and efficient CFD method relies on two key ideas: efficient high-order CFD methods and automated adaptation with a rapid reliable error estimation. The solution strategy and adaptation must be fully autonomous with no user interaction and no requirements for the user's prior knowledge of the flow phenomena. This section presents motivation and a review of the background for these ideas.

1.1.1 High-Order CFD Methods

Current production CFD codes used in the aerospace industry are either first or second order accurate, which are usually called low order methods, while 3^{rd} and higher order ones are generally defined as high-order methods. A method is k^{th} order accurate if the discretization error is proportional to h^k with h being a measure of the mesh size. This means that when the mesh resolution is doubled, the solution error only decreases by a factor of 2 or 4 for 1^{st} or 2^{nd} order methods, while it can decrease by a factor of 2^k ($k > 2$) for high-order methods. Advantages of high-order methods are well recognized in the computational fluid dynamics (CFD) community especially for problems requiring a high-level of accuracy, such as vortex dominated flows, aeroacoustic noise predictions, large eddy simulation and direct numerical simulation (DNS) of turbulent flows. The results of the First and Second International High-order CFD Workshop indicate that, for smooth problems with smooth geometries, high-order methods outperform low-order ones in terms of computing efficiency and accuracy [113]. Because of the considerable potential, high-order methods have received significant research interests in the global CFD community in the last two decades. A variety of high-order methods have been developed. Refer to several books [45, 58, 116] and reviews

[27, 115] for the state of the art and recent progress in the development of such methods.

Most high-order methods employ polynomials of degree 2 or higher to approximate the solution (unknowns). In two dimensions, at least six degrees of freedom (DOFs) or solution unknowns are required to build a degree 2 polynomial. Depending on how many DOFs are available on a cell or element, multiple cells may be needed to build the solution polynomial. For example, at least 5 neighboring cells are required to reconstruct a degree 2 polynomial in a finite volume method, since each cell only has one DOF, the cell-averaged solution.

An alternative approach to build high-order polynomials is to put enough DOFs in each element. In a discontinuous Galerkin (DG) [3, 5–7, 20–22, 37, 61, 80, 82, 83, 117], residual distribution (RD) [3], spectral volume (SV) [69, 108, 114] /difference (SD) [59, 66, 69, 78, 99], each cell has enough DOFs so that neighboring data is not required in building the solution polynomial. Such methods are compact because only immediate face neighbors play a role in updating the DOFs in the current cell. Compact methods are easy to implement on CPU and GPU clusters because the amount of data communication is minimized.

In order to improve the efficiency of the DG method, high-order methods in the differential form have been developed recently. The correction procedure via reconstruction (CPR) method is a nodal differential formulation [51]. The element-wise discontinuous solution polynomial is interpolated from the unknowns at a set of solution points. Furthermore, to satisfy conservation at element interfaces, a new flux polynomial is reconstructed using a correction function and the flux jumps on the element boundaries. This formulation has some remarkable properties. The framework is easy to understand, efficient to implement and can recover several known methods such as the DG, SG or the SV/SD methods. The framework was applied to solve diffusion problems using quadrilateral meshes in [52]. Wang and Gao extended the idea to 2D triangular [107] and mixed meshes with the lifting collocation penalty (LCP) formulation. In [94], CPR was further extended to 3D hybrid meshes. Some recent developments of the CPR method can be found in [15, 16, 35, 36, 53, 54, 89, 111]. This work uses a high-order CPR discretization, and the state of the art of the CPR method is further

discussed in Chapter 2.

1.1.2 Error Estimation and Adaptation

The high-order methods have the potential of delivering higher accuracy with less CPU time than lower order methods. However, the spatial operator is also more stiff than a low order one. With the same number of DOFs, high-order methods do take longer CPU time. For non-smooth problems, the advantage of high-order methods hinges on solution based hp adaptations. The adaptive methods have the capability of dynamically distributing computing resources to a desired area to achieve the required accuracy with minimal costs [18, 24, 49, 72]. Thus, adaptive high-order methods have received considerable attention in the CFD community [28, 32, 43, 103, 104, 109, 121]. Furthermore, reliable prediction of the output of interest from the CFD simulation involves a robust and accurate error estimation.

The effectiveness of adaptive methods highly depends on the accuracy of the error estimation. There are at least three major types of adaptation criteria: gradient or feature based [4, 12, 42, 118], residual-based [1, 2, 14, 34, 55, 90], and adjoint-based [10, 19, 28, 39, 40, 43, 63, 64, 79, 102–104, 109, 122]. Heuristic feature-based criteria perform refinements around some unique flow features, such as large gradients or strong vorticity. It does not directly relate to the output of interest. Therefore, it cannot provide a universal and robust error estimation [103, 124]. The residual-based error indicator targets the elements which have large discretization errors for refinement. The locally defined element-wise error may lead to false refinements in convection-dominated problems. The dual-weighted residual method proposed by Becker and Rannacher [9] relates a specific functional output directly to the local residual by solving an additional adjoint equation. It can capture the error propagation effects inherent in the hyperbolic equations. This kind of adjoint-based error indicator has been shown very effective in driving an hp-adaptation procedure to obtain a very accurate prediction of the functional outputs [10, 13, 19, 39, 40, 110, 122]. Recently, Fidkowski and P.L Roe developed a new error indicator based on the entropy variables, which can be inter-

preted as the dual solution of the output of entropy balance on the whole domain. It can be obtained directly from the state variables without solving extra adjoint equations and has been successfully applied to inviscid, viscous and turbulence flows [29, 30].

The adjoint solution is required for the error estimate and output-based adaptation. There are two approaches to obtain the adjoint: the continuous adjoint and the discrete adjoint. It has been shown that the discrete adjoint solution leads to a more accurate error estimation for the fine grid functional, while the continuous adjoint gives a better output estimation when the primal and adjoint solutions are well resolved [65]. However, the discrete adjoint solution should be consistent with the exact adjoint from the continuous adjoint equation. It is well known that dual consistency can significantly impact the convergence rate of both the primal and adjoint approximations. There are several possible sources of dual inconsistency in a high-order discretization. A dual-consistent discretization with variational forms, such as the finite element and DG methods, were examined for the Euler and Navier-Stokes equations in the literature [39, 40, 44, 56, 84]. More recently, adjoint-based error estimation for summation-by-parts finite-difference methods have been studied [11, 46, 47]. However, the analysis of the dual consistency for compact high-order differential-type methods appears lacking. This is one of the focuses of the present study.

The high-order CPR method can handle arbitrary solution order on mixed grids. The marked candidate elements for adaptation can be modified by enriching its solution order or subdividing its element or resizing its grid. Thus, the ways to increase the discretization resolution can be generally classified into 3 categories: h-refinement, r-refinement and p-refinement. For h-refinement, subdivision is performed locally for each candidate element to increase the total DOFs. R-refinement or the moving mesh method keeps the total number of nodes the same but moves the location of the grid locally or globally [49]. With p-refinement, the local degree of approximation polynomial is modified. The moving mesh method with curved elements in 3D is till an on-going research. In this work, we only modify the solution polynomial order locally or subdivide elements hierarchically for adaptations. Intuitively,

h-refinement should be applied to the discontinuities and p-enrichment is appropriate in smooth flow regions. However, optimal choice between h- or p-refinement is not a trivial problem, which is studied in the previous research [8, 13, 19, 23, 38, 48, 58, 98, 110].

The compressible Navier-Stokes equations may produce strong directional phenomena, such as boundary layers, shear layers and shock waves. For isotropic adaptation, each cell is subdivided into four elements in 2D and eight elements in 3D, which is very costly to resolve these kind of features. In contrast, stretched elements with high aspect ratios are preferred for optimal resolution of anisotropic features. Considerable work has been devoted to the adjoint based anisotropic adaptation. A common and simple approach to incorporate the directional information for adaptation is to use the Hessian-based metric field of a single solution variable, e.g. pressure or Mach number. For this method, the metric filed can be interpreted as the interpolation error for the picked variable [18, 81]. However, it does not consider the adjoint solution and cannot provide any information for the functional error. Venditti and Darmofal [103] extended the Hessian-based metric of the Mach number to the dual weighted metrics with size information. While similar techniques have been applied in [24, 28, 33, 62, 73], their anisotropy decision requires *a priori* knowledge of the solution to pickup the representing scalar variable. The link between the directional information and the functional error is not clear. Recently, a popular approach to drive anisotropic adaptation is to perform an output error sampling procedure from a discrete set of refinement choices. The idea of guiding anisotropy adaptation for the engineering output by solving local problems was presented in [19, 38, 63, 122]. In this method, during the trial refinement process, the elemental functional error is directly estimated and monitored. In the current work, the sampling procedure is utilized to drive the anisotropic adaptation.

1.2 Objectives of the Present Research

The main objective of this work is to develop a robust, efficient and accurate adaptive high-order differential formulation for the compressible Navier-Stokes equations, which can predict an accurate engineering output. The specific objectives of the dissertation are identified as follows:

- Develop a dual-consistent discrete adjoint equation for the CPR method.
- Develop an efficient and accurate automated adjoint-based error estimation method for the CPR formulation.
- Develop an adjoint-based anisotropic adaptation strategy.
- Implement an adjoint-based hp-adaptation solver with the CPR method, which can handle arbitrary discretization orders, and compare the different adaptation strategies.
- Demonstrate the importance of hp-adaptation for the high-order CPR method to aerodynamic flows and engineering problems.

1.3 Dissertation Organization

The rest of the thesis is organized as follows. Chapter 2 reviews the high-order CPR method used in this work. Chapter 3 develops a hybrid $P_N P_M - CPR$ framework for the hyperbolic conservation laws and its extension to the Navier-Stotkes equations. The dual consistency of the CPR method is studied in Chapter 4. Chapter 5 describes the adjoint-based adaptation strategies and the local output error sampling procedures. Then several numerical tests are presented in Chapter 6 to demonstrate the effectiveness of the proposed adaptive method. Finally, conclusions and some possible future work are given in Chapter 7.

Chapter 2

The High-Order CPR Method

2.1 Introduction

Currently, one of the most developed and most widely used high-order methods for the compressible Navier-Stokes equations on unstructured grids is the DG method. In order to improve the efficiency of the DG method, a class of high-order methods in the differential form, e.g. the Staggered-grid Chebyshev multi-domain method [59] and the SD method, has been developed. Recently a new high-order differential formulation named the CPR method has been proposed. The basic methodology of the high-order CPR method was first introduced by Huynh in the form of the flux reconstruction (FR)[51]. The same author presented the extension of the CPR method to diffusion problems [52]. Wang & Gao extended it to simplex and hybrid elements under the name of the lifting collocation penalty [107]. The involved authors later decided to use the unified name CPR for the method. Haga, Gao and Wang presented the extension of the CPR method to the 3D Navier-Stokes equations on mixed grids [41, 94]. A family of energy stable CPR methods for the linear advection equation, named as Energy Stable Flux Reconstruction or VCJH scheme, was proposed by Vincent, Castonguay and Jameson [106]. It has been further studied in [54, 105] and extended to triangle elements in [16] and the linear-advection-diffusion equation in [17, 119]. Yu, Wang

and Liu presented a detailed comparison of the accuracy and computational efficiencies of the CPR method to the other high-order methods [123]. A similar computational performance study of the CPR method and the SD method was carried out by Liang [67].

The advantage of the simplicity and computational efficiency of the CPR method has drawn a lot of attentions of many researchers. Many significant contributions were made to this topic. A hybrid P_nP_m extension of the CPR method for the Euler and the Navier-Stotkes equations was developed in Ref. [88, 89, 112]. Shi & Wang presented a dual-consistent CPR formulation and studied the adjoint-based error estimation and adaptation for the CPR method [85–87]. A study of the conservative property of different discretization methods for the flux divergence term was presented in [35]. Applications of the CPR method to the problems related to the moving/deforming mesh were studied in [68]. In [14, 15], Cagnone and Nadarajah developed a CPR scheme with the interface element to handle the non-conforming surface generated after p-adaptation. The extension of the artificial viscosity approach to the CPR method for solving flow with shocks was studied in [57, 93]. Results of the large eddy simulation using the CPR method were shown in [70, 71]. A very nice overview of the CPR method and its recent developments is given in a review article by Huynh, Wang and Vincent [50].

2.2 The CPR Method via the Flux Reconstruction

The CPR method solves the partial differential equations in the differential form. In the CPR formulation, the unknowns or the DOFs are defined at a set of nodal points on each element, which are called the solution points (SPs). In each cell, a piece-wise polynomial called the solution polynomial is constructed by those DOFs. They are built by interpolating the unknowns locally without any information from their neighbors. Thus, the solution polynomials are discontinuous across cell surfaces, which forms a Riemann problem from each interface's left and right values. In addition, a piecewise continuous flux polynomial, whose

degree is one order higher than the solution polynomial, are defined by the Riemann flux at the cell interfaces together with the flux evaluated at the interior SPs. This reconstructed continuous flux polynomial incorporates the influences from the neighboring cells along the upwind directions and can satisfy the conservation requirements from the governing equation. The unknowns on the SPs are updated by taking the spatial derivatives of the reconstructed flux polynomial.

Consider the conservation law in 1D

$$\frac{\partial Q}{\partial t} + \frac{\partial F}{\partial x} = 0$$

with proper initial and boundary conditions, where Q is the state variable, and F is the flux. Here, the flux $F = F(Q)$ is a function of solution variable Q. Assume the domain of simulation is divided into N non-overlapping elements $\{V_i\}_{i=1}^{N}$. In order to achieve an efficient implementation, all elements are transformed from the physical domain x into a standard element in the computational domain $\xi \in [-1, 1]$ by

$$x = x_{i-1/2} + \frac{h_i}{2}(\xi + 1), \tag{2.1}$$

where h_i is the length of V_i and $x_{i-\frac{1}{2}}$ is the x coordinate of cell i's left boundary.

Next, denote the unknowns or the DOFs by $Q_{i,j}$, which are the solution variables at SP j of cell i, where $j = 1, ..., K$. On each cell V_i, a piecewise solution polynomial $Q_i(\xi)$ of degree $K - 1$ can be constructed by interpolating the DOFs $Q_{i,j}$ locally

$$Q_i(\xi) = \sum_{j=1}^{K} \phi_j(\xi) Q_{i,j}.$$

$\phi_j(\xi)$ is the Lagrange shape function defined on each SP j. The location of the SPs can be picked up as the standard Gauss quadrature points or Lobatto quadrature points denoted by $\{\xi_j\}$. For a linear problem, the accuracy and stability property of the CPR methods are

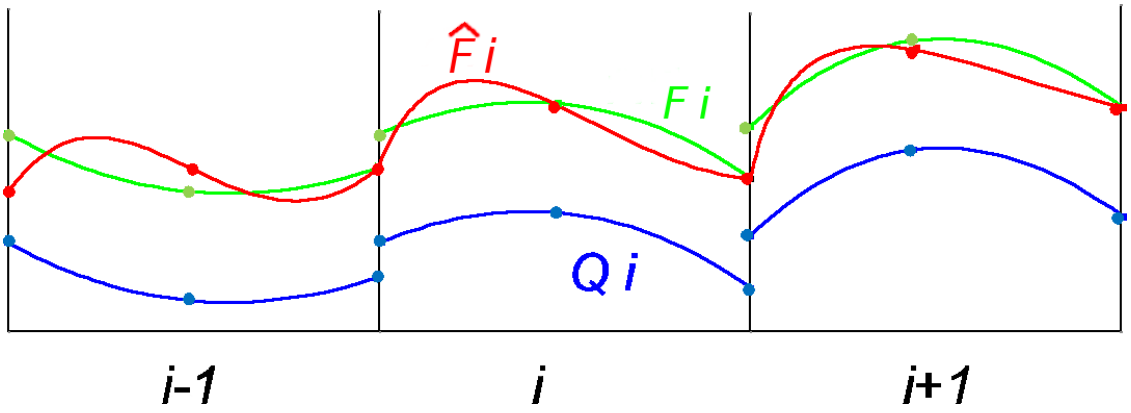

Figure 2.1: Solution and flux polynomials for a $3rd$ order CPR scheme, Lobatto points as the SPs. (Q_i: the solution polynomial; F_i: the analytical flux polynomial; $\hat{F}_i$: the reconstructed flux polynomial).

independents of the location of the SPs[51]. However, using the Gauss points as the SPs can reduce the alias error for solving the non-linear equations. Similarly, a piecewise analytical flux polynomial $F_i(\xi)$ can be built by first evaluating the flux

$$F_{i,j} = F(Q_{i,j})$$

with the solution variable $Q_{i,j}$ and then performing a Lagrange interpolation

$$F_i(\xi) = \sum_{j=1}^{K} \phi_j(\xi) F_{i,j}.$$

Note that only the local DOFs are utilized to construct the solution polynomial $Q_i(\xi)$ and the analytical flux polynomial $F_i(\xi)$ (see Figure 2.1). Thus, they are piecewise functions defined on each element and are discontinuous across cell surfaces. The solution jumps on each cell's interface leads to a Riemann problem. A common or upwind flux on interface $i + \frac{1}{2}$ denoted by $F^{com}_{i+\frac{1}{2}}$ can be defined

$$F^{com}_{i+\frac{1}{2}} = F^{com}(Q_L, Q_R)$$

with left and right solution values $Q_L = Q_{i,K}$ and $Q_R = Q_{i+1,1}$.

The key idea of the FR method is to reconstruct a continuous flux polynomial $\hat{F}(\xi)$ of degree K, which can recover the common flux at the cell interface and approximate the analytic flux polynomial $F_i(\xi)$ elsewhere in that cell (see Figure 2.1). Thus, on cell i, the reconstructed continuous flux polynomial $\hat{F}$ is defined as

$$\hat{F}_i(\xi) = F_i(\xi) + \sigma_i(\xi),$$

where $\sigma_i(\xi)$ is a correction term. According to [51], $\sigma_i(\xi)$ should approximate the zero function and satisfy the following equation

$$\sigma_i(\xi) = [F^{com}_{i-1/2} - F_i(-1)]g_L(\xi) + [F^{com}_{i+1/2} - F_i(1)]g_R(\xi).$$

Here, $g_L(\xi)$ and $g_R(\xi)$ are both degree K polynomials called correction functions with the properties

$$g_L(-1) = 1, \quad g_L(1) = 0, \quad g_R(-1) = 0, \quad g_R(1) = 1.$$

Then the CPR method for the 1D conservation law can be expressed as

$$\frac{\partial Q_{i,j}}{\partial t} + \frac{\partial F_i(\xi)}{\partial \xi}\frac{2}{h_i} + \frac{2}{h_i}[F^{com}_{i-1/2} - F_i(-1)]g'_L(\xi_{i,j}) + \frac{2}{h_i}[F^{com}_{i+1/2} - F_i(x_{i+1/2})]g'_R(\xi_{i,j}) = 0.$$

A series of correction functions with different accuracy and stability properties were developed in [51]. If the correction function g is chosen as right Radau polynomials, the DG method is recovered from the CPR scheme. In this case, the correction function denoted by g_{DG} or g_1 is perpendicular to the degree k-1 polynomial space. Similarly, a g_2 correction function is defined, which is perpendicular to the degree k-2 polynomial space. In summary, for any integer $m \geqslant 1$, a g_m correction function can be defined which is perpendicular to P^{k-m}. Figure 2.2 plots the shape of g_{DG} as the left correction functions for $K = 1 \sim 4$

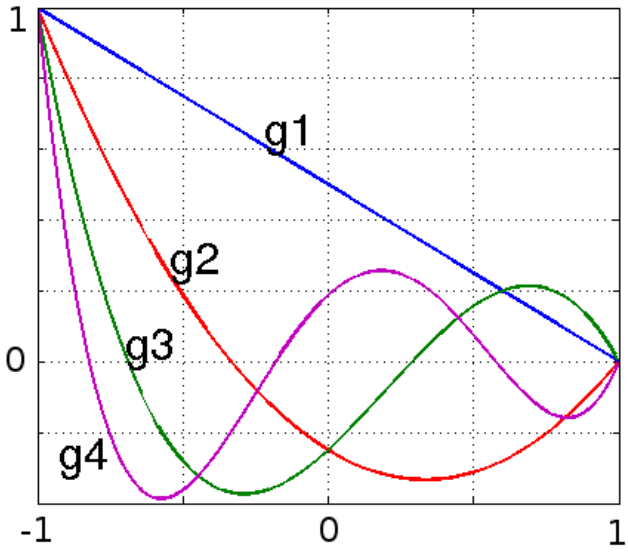

Figure 2.2: The g_{DG} correction functions for $K = 1 \sim 4$.

on domain $[-1, 1]$. Intuitively, a more steeper correction function leads to a more accurate scheme with a relatively small CFL number restriction.

The CPR method for the quadrilateral and hexahedral element is a tensor product of the 1D formulation in each axis. For quadrilateral cells, all elements are transfered from the physical domain (x, y) to the standard quadrilateral element in the computational domain (ξ, η) defined as

$$\{\vec{\xi} = (\xi, \eta) | -1 \leq \xi \leq 1, -1 \leq \eta \leq 1\}.$$

The transformed equation in the computational domain takes the following form

$$\frac{\partial \tilde{Q}}{\partial t} + \frac{\partial \tilde{F}}{\partial \xi} + \frac{\partial \tilde{G}}{\partial \eta} = 0,$$

where

$$\tilde{Q} = |J|Q,\ \vec{F} = [F, G]^T,\ \tilde{F} = \vec{S}_\xi \cdot \vec{F},\ \tilde{G} = \vec{S}_\eta \cdot \vec{F}.$$

Here, J is the Jacobian matrix of the transformation

$$J = \frac{\partial \vec{r}}{\partial \vec{\xi}} = \begin{bmatrix} x_\xi & x_\eta \\ y_\xi & y_\eta \end{bmatrix};$$

$\vec{S}_\xi$ and $\vec{S}_\eta$ are the area vectors of constant ξ and η lines defined as

$$\vec{S}_\xi = |J|\nabla\xi,\ \vec{S}_\eta = |J|\nabla\eta.$$

$\tilde{Q}_{i,j,m}$ is used to denote the DOFs, the solution point (j, m) of cell i. Then, the CPR formulation on the quadrilateral element takes the form

$$\begin{aligned} &\frac{\partial \tilde{Q}_{i,j,m}}{\partial t} + (\nabla^\xi \cdot \vec{\tilde{F}})_{j,m} \\ &\quad + [\tilde{F}_{com}(-1, \eta_{j,m}) - \tilde{F}_i(-1, \eta_{j,m})]g_L^{'}(\xi_{j,m}) + [\tilde{F}_{com}(1, \eta_{j,m}) - \tilde{F}_i(1, \eta_{j,m})]g_R^{'}(\xi_{j,m}) \\ &\quad + [\tilde{G}_{com}(\xi_{j,m}, -1) - \tilde{G}_i(\xi_{j,m}, -1)]g_L^{'}(\eta_{j,m}) + [\tilde{G}_{com}(\xi_{j,m}, 1) - \tilde{G}_i(\xi_{j,m}, 1)]g_R^{'}(\eta_{j,m}) = 0, \end{aligned}$$

where $\vec{\tilde{F}} = [\tilde{F}, \tilde{G}]$ is the transformed flux and ∇^ξ is the divergence operator taking in the computational domain. The correction for each SP is performed in a 1D approach, as shown in Figure 2.3. The extension of the CPR method to Hexahedral elements are straightforward via the tensor production of the 1D formula in the transformed ξ, η and ζ directions respectively.

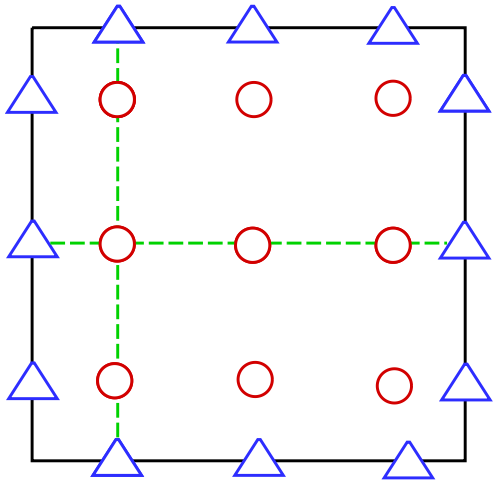

Figure 2.3: The CPR formulation on the quadrilateral element $k = 2$ (◯: SPs, △: FPs).

2.3 The CPR Method via the Lifting Collocation Penalty

In the lifting collocation penalty framework, the CPR method [51, 107] is formulated by transforming a weighted residual form into a differential one. Consider a hyperbolic conservation law

$$\frac{\partial Q}{\partial t} + \nabla \cdot \vec{F}(Q) = 0, \tag{2.2}$$

with proper initial and boundary conditions, where Q is the state vector, and $\vec{F} = (F, G)$ is the flux vector. Assume that the computational domain Ω is discretized into N non-overlapping triangular elements $\{V_i\}_{i=1}^{N}$. Let W be an arbitrary weighting or test function. The weighted residual formulation of Eq. 2.2 on element V_i can be expressed as

$$\int_{V_i} \left(\frac{\partial Q}{\partial t} + \nabla \cdot \vec{F}(Q) \right) W \mathrm{d}\Omega = 0. \tag{2.3}$$

Let Q_i be an approximate solution to the analytical solution Q on V_i. On each element, the solution belongs to the space of polynomials of degree k or less, i.e., $Q_i \in P^k(V_i)$. After applying integration by parts twice to the flux divergence and replacing the normal flux term with a common Riemann flux F_{com}^n in the above equation, we get

$$\int_{V_i} \frac{\partial Q_i}{\partial t} W \mathrm{d}\Omega + \int_{V_i} W \nabla \cdot \vec{F}(Q_i) \mathrm{d}\Omega + \int_{\partial V_i} W \left[F^n_{com} - F^n(Q_i) \right] \mathrm{d}S = 0. \tag{2.4}$$

Here the common Riemann flux F^n_{com} is defined as

$$F^n_{com} = F^n_{com}(Q_i, Q_{i+}, \vec{n}), \tag{2.5}$$

where Q_{i+} denotes the solution outside the current element V_i, and the normal flux $F^n(Q_i)$ at the interface is

$$F^n(Q_i) = \vec{F}(Q_i) \cdot \vec{n}.$$

In order to eliminate the test function, the boundary integral above is cast as a volume integral via the introduction of a "correction field" on V_i, $\delta_i \in P^k(V_i)$,

$$\int_{V_i} W \delta_i \mathrm{d}\Omega = \int_{\partial V_i} W [F^n] \mathrm{d}S, \tag{2.6}$$

where $[F^n] = F^n_{com} - F^n(Q_i)$ is the normal flux difference. Substituting Eq. 2.6 into Eq. 2.4, we obtain

$$\int_{V_i} \left(\frac{\partial Q_i}{\partial t} + \nabla \cdot \vec{F}(Q_i) + \delta_i \right) W \mathrm{d}\Omega = 0. \tag{2.7}$$

If the flux vector is a linear function of the state variable, then $\nabla \cdot \vec{F}(Q_i) \in P^k$. In this case, the terms inside the square bracket are all elements of P^k. Because the test space is selected to ensure a unique solution, Eq. 2.7 is equivalent to

$$\frac{\partial Q_i}{\partial t} + \nabla \cdot \vec{F}(Q_i) + \delta_i = 0. \tag{2.8}$$

For nonlinear conservation laws, $\nabla \cdot \vec{F}(Q_i)$ is usually not an element of P^k. As a result, Eq. 2.7 cannot be reduced to Eq. 2.8. In this case, the most obviously choice is to project

$\nabla \cdot \vec{F}(Q_i)$ into P^k. Denote $\Pi\big(\nabla \cdot \vec{F}(Q_i)\big)$ as a projection of $\nabla \cdot \vec{F}(Q_i)$ to P^k. One choice is

$$\int_{V_i} \Pi\big(\nabla \cdot \vec{F}(Q_i)\big) W \mathrm{d}\Omega = \int_{V_i} \nabla \cdot \vec{F}(Q_i) W \mathrm{d}\Omega. \tag{2.9}$$

Then Eq. 2.7 reduces to

$$\frac{\partial Q_i}{\partial t} + \Pi\big(\nabla \cdot \vec{F}(Q_i)\big) + \delta_i = 0. \tag{2.10}$$

Next, let the DOFs be the solutions at a set of solution points (SPs) $\{\vec{r}_{i,j}\}$ (j varies from 1 to $K = (k+1)(k+2)/2$). Figure 2.4 shows the configuration of the SPs and FPs for a $k = 1$ scheme using the standard Gauss quadrature points.

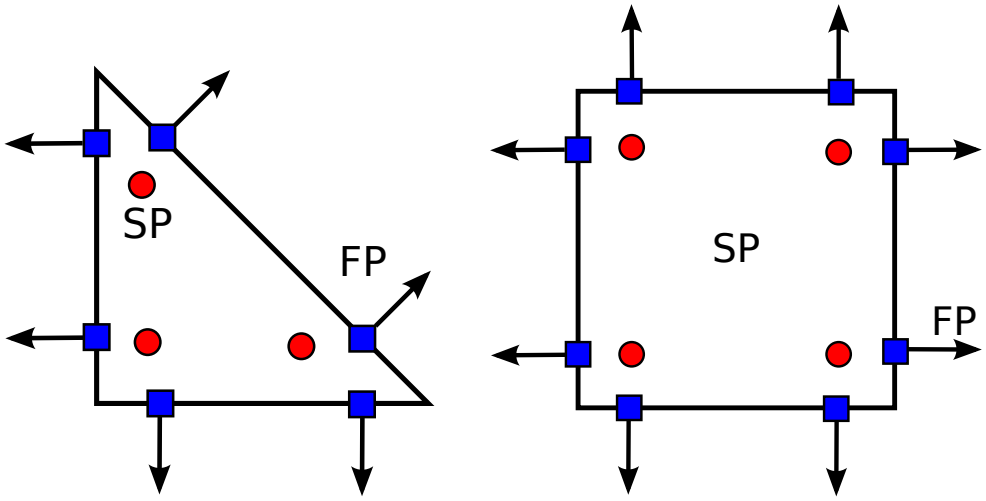

Figure 2.4: Configuration of the solution and flux points using the Gauss quadrature points for $k = 1$(◯: SPs, □: FPs).

Then Eq.2.10 is true at the SPs, i.e.,

$$\frac{\partial Q_{i,j}}{\partial t} + \Pi_j\big(\nabla \cdot \vec{F}(Q_i)\big) + \delta_{i,j} = 0, \tag{2.11}$$

where $\Pi_j\big(\nabla \cdot \vec{F}(Q_i)\big)$ denotes the values of $\Pi\big(\nabla \cdot \vec{F}(Q_i)\big)$ at SP j. The efficiency of the CPR approach hinges on how the correction field δ_i and the projection $\Pi\big(\nabla \cdot \vec{F}(Q_i)\big)$ are computed. Two approaches, the Lagrange polynomial (LP) and the chain-rule (CR) formulations, were

suggested to compute the projection of the flux divergence [107]. For the LP approach, the flux is assumed to belong to the polynomial space of degree k, e.g. $F, G \in P^k$. Therefore, the projection of the flux divergence is expressed as

$$\Pi\big(\nabla \cdot \vec{F}\big) = \nabla \cdot (\sum_j L_j \vec{F}_j),$$

where L_j is the Lagrange interpolation polynomial defined on SP j. For the CR approach, the flux divergence $\nabla \cdot \vec{F}$ is assumed to belong to the polynomial space P^k, which can be expressed as

$$\Pi\big(\nabla \cdot \vec{F}\big) = \sum_j L_j (\frac{\partial \vec{F}}{\partial Q} \cdot \nabla Q)_j.$$

Note that, for a linear conservation law, the LP and CR approaches lead to the same formulation. However, for a nonlinear flux equation, the CR approach can reduce the aliasing errors [107]. For the sake of simplicity, the projection operator Π is omitted in the rest of the paper.

To compute δ_i, we define $k+1$ points named flux points (FPs) along each interface, where the normal flux differences are computed. We approximate (for nonlinear conservation laws) the normal flux difference $[F^n]$ with a degree k interpolation polynomial along each interface,

$$[F^n]_f \approx \mathbf{I}_k [F^n]_f \equiv \sum_l [F^n]_{f,l} L_l^{FP}, \tag{2.12}$$

where f is a face (or edge in 2D) index, and l is the FP index, and L_l^{FP} is the Lagrange interpolation polynomial based on the FPs in a local interface coordinate. For linear triangles with straight edges, once the solution points and flux points are chosen, the correction at the SPs can be written as

$$\delta_{i,j} = \frac{1}{|V_i|} \sum_{f \in \partial V_i} \sum_l \alpha_{j,f,l} [F^n]_{f,l} S_f, \tag{2.13}$$

where $\alpha_{j,f,l}$ are lifting constants independent of the solution variables, S_f is the face area, $|V_i|$ is the volume of V_i. By using different lifting coefficients $\alpha_{j,f,l}$, some well know high-order methods can be casted in the CPR framework. Detailed discussion can be found in [107].

Chapter 3

The $P_N P_M - CPR$ Framework

The $P_N P_M - CPR$ formulation is an extension of $P_N P_M$ or the reconstructed discontinuous Galerkin (RDG) method to the CPR framework. It is a hybrid finite volume and discontinuous Galerkin (DG) method, in which neighboring cells are used to build a higher order polynomial than the solution representation in the cell under consideration. In this chapter, we present several $P_N P_M$ schemes under the CPR framework. Many interesting schemes with various orders of accuracy and efficiency are developed. The dispersion and dissipation properties of those methods are investigated through a Fourier analysis, which shows that the $P_N P_M - CPR$ method is dependent on the position of the solution points. Optimal solution points for 1D $P_N P_M - CPR$ schemes which can produce expected order of accuracy are identified. In addition, the $P_N P_M - CPR$ method is extended to solve 2D inviscid flow governed by the Euler equations and several numerical tests are performed to assess its performance.

3.1 Basic Ideas of the Hybrid Methods

Most high-order methods employ polynomials of degree 2 or higher to approximate the solution (unknown). In two dimensions, at least six degrees of freedom (DOFs) or solution unknowns are required to build a degree 2 polynomial. Depending on how many DOFs are

available on a cell or element, multiple cells may be needed to build the solution polynomial. For example, at least 5 neighboring cells are required to build a degree 2 polynomial in a finite volume method because each cell only has one DOF, the cell-averaged solution. In a discontinuous Galerkin (DG) [3, 5–7, 20–22, 37, 61, 80, 82, 83, 117], residual distribution (RD) [3], spectral volume (SV)[69, 108, 114] /difference (SD) [59, 66, 69, 78, 99] or the correction procedure via reconstruction (CPR) method [15, 51–53, 94, 107, 111], each cell has enough DOFs so that neighboring data is not required in building the solution polynomial. Such methods are compact because only immediate face neighbors play a role in updating the DOFs in the current cell. Compact methods are easy to implement on CPU and GPU clusters, and highly scalable because the amount of data communication is minimized.

Although 2^{nd} order finite volume schemes are not strictly compact as neighbor's neighbors are used in the solution update, they can be implemented in a "compact" manner by messaging passing through only immediate neighbors on a parallel computer. This is because the reconstruction stencil is compact, as shown in Figure 3.1, which shows both the "reconstruction stencil" and the "scheme stencil".

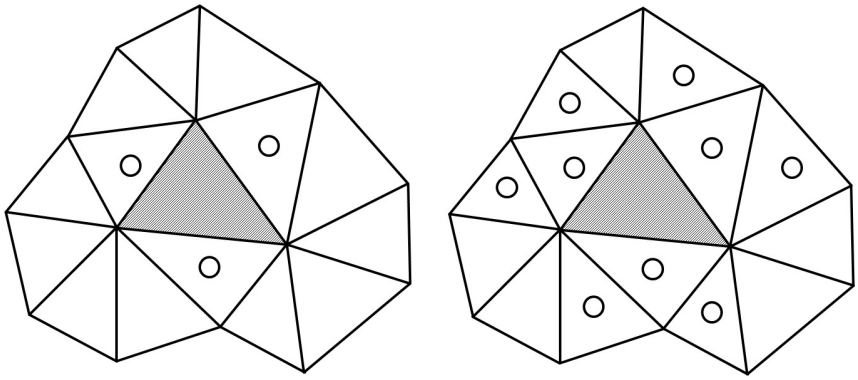

(a) The reconstruction stencil (b) The scheme stencil

Figure 3.1: The reconstruction and scheme stencils of a 2^{nd} order finite volume method.

More recently, hybrid methods named $P_N P_M$ [25, 26], reconstructed DG (RDG) [75, 76], hybrid FV/DG [125–127], weighted integral based schemes [120] have been developed. The

key idea of these methods is to use multiple DOFs on the current cell and its neighbors to build a solution polynomial higher than that with the DOFs on a single element. This solution polynomial is then used to generate high-order updates for the DOFs on the current element. This hybrid approach thus offers a whole new host of possibilities:

- How to reconstruct the solution polynomial and at what degree?
- How to update the DOFs at the current element?

The number of choices is quite large, and in fact, the FV and DG/SV/SD/CPR methods can be viewed as two extreme special cases of the new family of possible methods. As mentioned earlier, many choices have already been explored, and some unique features have been demonstrated, e.g.,

- More efficient per DOF than either the FV or DG method;
- Lower memory requirement for implicit schemes to achieve a given order of accuracy than the DG/SV/SD methods.

We attempt to maintain the simplicity in the formulation, while investigating the accuracy and stability of different choices. In the next section, we present the basic $P_N P_M - CPR$ formulation in 1D and 2D. Then we discuss the Fourier analysis of the $P_N P_M - CPR$ schemes.

3.2 Hybrid $P_N P_M - CPR$ Methods

The key idea of the hybrid $P_N P_M - CPR$ formulation is to use multiple DOFs on the current cell and its neighbors to build a solution polynomial higher than that with the DOFs on a single element. We hope to achieve higher order accuracy if the higher degree polynomial denoted as U_i is used to update the flux divergence term and penalty terms in the 1D CPR method as

$$\frac{\partial Q_{i,j}}{\partial t} + \Pi_j \left(\frac{\partial F(U_i)}{\partial x} \right) + [F^{com}_{i-1/2} - F_i(x_{i-1/2})] g'_L(x_{i,j}) + [F^{com}_{i+1/2} - F_i(x_{i+1/2})] g'_R(x_{i,j}) = 0. \quad (3.1)$$

One of the key questions for the $P_N P_M - CPR$ method is how to perform the common flux correction. For a $P_N P_M - CPR$ method, unknowns of each cell are still only determined by the local P^n polynomial, which are only required to be orthogonal to the P^n space. This leads to a L_2 projection of the correction field by the basis of the degree n polynomial space. So in 1D, the correction function of the CPR method can be directly used for the $P_N P_M - CPR$ method. However, for 2D problems, a new set of correction functions is required. The derivation is shown in detail in section 4.

The hybrid scheme is uniquely defined once the reconstruction polynomial U_i is determined. The number of DOFs in each cell is denoted by K_n and we can build a polynomial $Q_i \in P^n$ from its local SPs on V_i. In order to obtain a higher order polynomial $U_i \in P^m$ $(m \geq n)$, we need more DOFs than what a single element can provide. To determine the higher degree polynomial, first we need to define the P^m reconstruction stencil S^i for each element

$$S^i = \bigcup_{e=1}^{n_s} Q_{i(e),j(e)}. \tag{3.2}$$

Here e is a local solution index for the reconstruction stencil of V_i, n_s is the total number of DOFs within the stencil, $i(e)$ and $j(e)$ stand for the mapping from the local reconstruction index e to the global element index i and the local SP index j in that cell. For the sake of compactness, we limit the reconstruction stencil to include the current cell and its immediate neighbors only. Furthermore, the reconstruction stencil is symmetric with respect to cell i. This is because upwinding is provided by the Riemann flux so that a central reconstruction stencil is preferred for accuracy and stability.

We have two choices to distribute the solution points, as shown in Figure 3.2 for the case of n = 1. Either the Lobatto points or the Gauss points can be SPs. In order to distinguish schemes based on these two types of SPs, $P_N P_M - CPR - L$ is used to denote schemes based on the Lobatto points, while $P_N P_M - CPR - G$ is used to denote schemes based on the Gauss points. With Lobatto points as the solution points, two solution points from the neighbors coincide with those in the current element, and must be excluded from the reconstruction

stencil. We therefore prefer Gauss points as the SPs.

(a) Lobatto points as the SPs (b) Gauss points as the SPs

Figure 3.2: Schematic of Labatto and Gauss points as the solution points (◯: the current element's SPs, □: the face-neighbors' SPs).

There are quite a few choices in how to build U_i. For example, one can choose either all or part of the SPs from the neighboring cells in the stencil. Another choice is the degree of U_i, m, which can be the highest possible based on the size of the stencil, i.e., $m = n_s - 1$, or lower. If $m < n_s - 1$, a constrained least squares method is used. The constraint is the reconstructed degree m polynomial U_i should preserve the nodal value of the degree n polynomial at the cell under consideration.

In order to achieve an efficient implementation, all elements are transformed from the physical domain x into a standard element in the computational domain $\xi \in [-1, 1]$

$$x = x_{i-1/2} + \frac{h_i}{2}(\xi + 1), \tag{3.3}$$

where h_i is the length of cell i. Suppose the degree m polynomial U for element i is expressed as

$$U(\xi) = \sum_{l=1}^{K_m} c_l \phi_l(\xi), \tag{3.4}$$

where $\phi_l(\xi)$ is the basis of degree m polynomial on the computational domain, c_l is their coefficient and K_m is the total number of DOFs needed for a degree m polynomial with K_m = m+1. We employ an interpolation based reconstruction approach for simplicity as the DOFs are nodal values at a given set of points. The value of the reconstructed polynomial U at every solution points $U_{i(e),j(e)} \in S^i$ is set to be equal to the original nodal solution value $Q_{i(e),j(e)}$:

$$U(\xi_{i(e),j(e)}) = Q_{i(e),j(e)}, \quad e = 1, 2, \ldots, n_s, \tag{3.5}$$

where $\xi_{i(e),j(e)}$ denotes parametric coordinate of DOFs at the stencil index e.

When the number of equations in Eq. 3.5 is larger than the dimension of the polynomial space, such as

$$n_s > K_m, \tag{3.6}$$

Eq. 3.5 is solved using a least squares technique with constraints. The reconstructed polynomial preserves the nodal values at the local SPs exactly

$$U(\xi_{i,j}) = Q_{i,j}, \quad j = 1, 2, \cdots, K_n. \tag{3.7}$$

Next we can construct the target function $f(c_l)$ with the constrained condition Eq. 3.7 using a standard Lagrange multiplier method:

$$f(c_1, c_2, \cdots, c_{K_m}) = \sum_{e=1}^{n_s} \left(U(\xi_{i(e),j(e)}) - Q_{i(e),j(e)}\right)^2 - \sum_{j=1}^{K_n} 2\lambda_j \left(U(\xi_{i,j}) - Q_{i,j}\right). \tag{3.8}$$

With the help of Vandermode matrix A

$$A_{e,l} = \phi_l \left(\xi_{i(e),j(e)}\right) \tag{3.9}$$

$$\tilde{A}_{j,l} = \phi_l(\xi_{i,j}), \tag{3.10}$$

the target function Eq. 3.8 can be rewritten as:

$$f(c_1, c_2, \cdots, c_{K_m}) = \sum_{e=1}^{n_s} \left(\sum_{l=1}^{K_m} A_{e,l} c_l - Q_{i(e),j(e)}\right)^2 - \sum_{j=1}^{K_n} 2\lambda_j \left(\sum_{l=1}^{K_m} \tilde{A}_{j,l} c_l - Q_{i,j}\right). \tag{3.11}$$

In order to find the coefficients $c_1, c_2, \cdots, c_{K_m}$ to minimize the function $f(c_1, c_2, \cdots, c_{K_m})$, we require

$$\frac{\partial f}{\partial \vec{c}} = 2A^T A\vec{c} - 2A^T\vec{Q} - 2\tilde{A}^T\vec{\lambda} = 0, \tag{3.12}$$

$$\frac{\partial f}{\partial \vec{\lambda}} = \tilde{A}\vec{c} - \vec{\tilde{Q}} = 0, \tag{3.13}$$

where $\vec{c} = [c_1, c_2, \cdots, c_{K_m}]^T$, $\vec{\lambda} = [\lambda_1, \lambda_2, \cdots, \lambda_{K_n}]^T$,$\vec{Q} = [Q_{i(e),j(e)}]^T$ and $\vec{\tilde{Q}} = [Q_{i,j}]^T$, so Eq. 3.12 and Eq. 3.13 can be expressed in matrix form

$$\begin{bmatrix} A^T A & -\tilde{A}^T \\ \tilde{A} & 0 \end{bmatrix} \begin{bmatrix} \vec{c} \\ \vec{\lambda} \end{bmatrix} = \begin{bmatrix} A^T\vec{Q} \\ \vec{\tilde{Q}} \end{bmatrix} \tag{3.14}$$

$$\begin{bmatrix} \vec{c} \\ \vec{\lambda} \end{bmatrix} = \begin{bmatrix} A^T A & -\tilde{A}^T \\ \tilde{A} & 0 \end{bmatrix}^{-1} \begin{bmatrix} A^T & 0 \\ 0 & I \end{bmatrix} \begin{bmatrix} \vec{Q} \\ \vec{\tilde{Q}} \end{bmatrix}. \tag{3.15}$$

From Eq. 3.15, the equation of the coefficient matrix C for degree m polynomial is defined as:

$$C = \begin{bmatrix} A^T A & -\tilde{A}^T \\ \tilde{A} & 0 \end{bmatrix}^{-1} \begin{bmatrix} A^T & 0 \\ 0 & I \end{bmatrix}, \tag{3.16}$$

which is only related to the geometry information and is pre-calculated for each cell. With the coefficient matrix C, the derivative matrix and interpolation matrix can be precomputed and stored during the preprocessing.

The reconstructed higher degree polynomial U_i is then used to generate a high-order update in the CPR formulation (Eq. 3.1). First it is used to compute the analytic flux derivative $\frac{\partial F(U_i)}{\partial x}$. Next the Riemann flux is computed with the reconstructed polynomials from the current cell and its face-neighbors. For example, the common flux at interface $i+\frac{1}{2}$ is computed using

$$F^{com}_{i+\frac{1}{2}} = F^n_{com}(U_i, U_{i+1}). \tag{3.17}$$

The interior flux is also computed with the reconstructed polynomial so the flux difference on the right interface is

$$[F^n]_R = F^{com}_{i+1/2} - F(U_i)_{i+\frac{1}{2}}. \tag{3.18}$$

Finally the $P_N P_M - CPR$ scheme for the 1D conservation law can be written as

$$\frac{\partial Q_{i,j}}{\partial t} + \Pi_j \left(\frac{\partial F(U_i)}{\partial x} \right) + g'_L(x_{i,j}) \left[F^n\right]_L + g'_R(x_{i,j}) [F^n]_R = 0, \tag{3.19}$$

where the correction function $g(x) \in P^{n+1}$.

Following the rules of thumb described earlier, we can design the following schemes under the $P_N P_M - CPR$ framework

- $P_N P_M - CPR - G - C$ and $P_N P_M - CPR - L - C$
  - In those schemes, all SPs in the neighboring cells are used to reconstruct U_i. Again, G indicates the standard Gauss quadrature points are used as the solution points; L means the Lobatto points are chosen as the solution points. C stands for the complete p^m stencil.
- $P_N P_M - CPR - G - IK$
  - In those schemes, not all SPs in the neighboring cells are used in the reconstruction. Instead, only the nearest DOFs from the neighboring cells are selected to build U_i. IK stands for only K DOFs from each neighboring cell are used in this incomplete p^m stencil.

Next, we show that there are some conservation constraints for the p^m reconstruction. In order to guarantee conservation, the following conservation law needs to be satisfied exactly on each element V_i

$$\int_{V_i} \frac{\partial Q_i}{\partial t} \mathrm{d}V + \int_{\partial V_i} \vec{F_i} \cdot \vec{n} \mathrm{d}S = 0. \tag{3.20}$$

In 1D, the above equation can be written as

$$\int_{V_i} \frac{\partial Q_i}{\partial t} \mathrm{d}x + F^{com}_{i+\frac{1}{2}} - F^{com}_{i-\frac{1}{2}} = 0. \tag{3.21}$$

Consider a quadrature rule defined on the $N+1$ solution points with its suitable weights w_k. Since it is exact at least for a degree N polynomial, therefore, the above cell integration can be written as

$$\int_{V_i} \frac{\partial Q_i}{\partial t} \mathrm{d}x = \frac{h_i}{2} \sum_{k=1}^{N+1} w_k \frac{\partial Q_{i,k}}{\partial t}. \tag{3.22}$$

Substitute the $P_N P_M - CPR$ formulation

$$\frac{\partial Q_{i,j}}{\partial t} + \frac{2}{h_i} \frac{\partial \hat{F}_{i,j}(U_i)}{\partial \xi} = 0 \tag{3.23}$$

with the corrected flux polynomial

$$\hat{F}_i(U_i) = F(U_i) + g_L(\xi)[F^n]_L + g_R(\xi)[F^n]_R \tag{3.24}$$

into the Eq. 3.22. The local solution change in one cell can be expressed as the weighted summation of the corrected flux derivatives evaluated on the solution points

$$\int_{V_i} \frac{\partial Q_i}{\partial t} \mathrm{d}x = -\sum_{k=1}^{N+1} w_k \frac{\partial \hat{F}_{i,k}}{\partial \xi}. \tag{3.25}$$

If the Gauss quadrature points are chosen as the solution points, the above quadrature using $N+1$ points can be exact for a polynomial of degree up to $2N+1$. Then the following equation is exact

$$\sum_{k=1}^{N+1} w_k \frac{\partial \hat{F}_{i,k}}{\partial \xi} = \int_{-1}^{1} \frac{\partial \hat{F}_i}{\partial \xi} \mathrm{d}\xi. \tag{3.26}$$

So the left hand side of Eq. 3.21 can be written as

$$-\int_{-1}^{1}\frac{\partial \hat{F}_i}{\partial \xi}\mathrm{d}\xi + F^{com}_{i+\frac{1}{2}} - F^{com}_{i-\frac{1}{2}}. \tag{3.27}$$

With the property of the corrected flux polynomial

$$\hat{F}_i(-1) = F^{com}_{i-\frac{1}{2}} \quad \hat{F}_i(1) = F^{com}_{i+\frac{1}{2}}, \tag{3.28}$$

the above equation leads to

$$-\int_{-1}^{1}\frac{\partial \hat{F}_i}{\partial \xi}\mathrm{d}\xi + F^{com}_{i+\frac{1}{2}} - F^{com}_{i-\frac{1}{2}} = 0, \tag{3.29}$$

which means that the $P_N P_M - CPR$ method is conservative with the Gauss points as the solution points when the degree of the reconstructed polynomial $M \leq 2N + 2$. Similarly, if the solution points are Lobatto points, the schemes are conservative if $M \leq 2N$.

The above schemes are tested in a grid refinement accuracy study using the following one dimensional linear wave equation:

$$\frac{\partial Q}{\partial t} + \frac{\partial Q}{\partial x} = 0, \quad x \in [0, 1] \tag{3.30}$$

with the initial condition $Q(x, 0) = sin(2\pi x)$, and periodic boundary conditions. The time integration schemes used are the TVD Runge-Kutta schemes of 3^{rd} or 4^{th} order accuracy [91]. The computation is carried out until t = 1. The L_2 solution error is plotted in Figure 3.3. Note that the hybrid $P_N P_M - CPR$ formulation can significantly improve the order of accuracy of the original CPR schemes. With the Gauss or Lobatto points as the solution points, the highest order of accuracy is 5^{th} for the $P_1 P_M - CPR$ schemes and 8^{th} for the $P_2 P_M - CPR$ schemes. When the number of data items in the P^m reconstruction stencil is more than the DOFs needed for the higher-order polynomial, $P_N P_M - CPR$ schemes

with an incomplete stencil is more accurate than those with a complete stencil. However, it is noted that we lost 1 order of accuracy for all $P_N P_M - CPR$ schemes with Lobatto points and $P1P4 - CPR - G - C$, $P1P5 - CPR - G - C$, $P2P6 - CPR - G - I2$ and $P2P8 - CPR - G - C$ schemes with Gauss points. The reason of the accuracy loss is going to be investigated through Fourier analysis in the next Session.

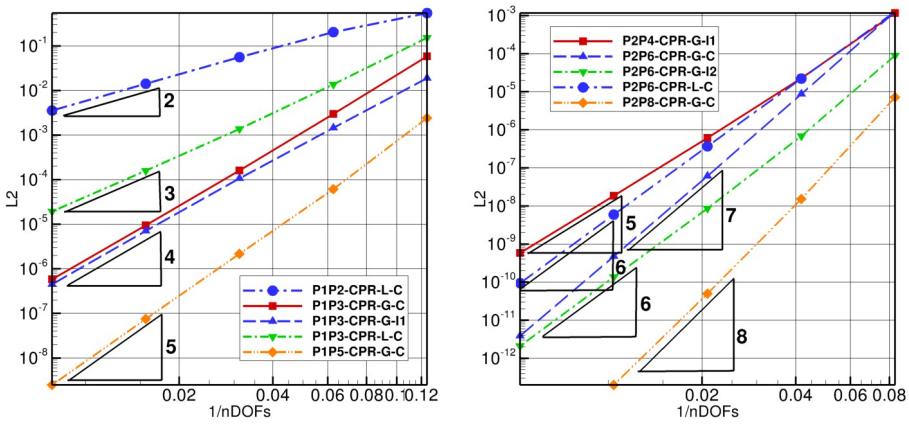

(a) $P_1P_M - CPR$ (b) $P_2P_M - CPR$

Figure 3.3: L_2 error of the $P_N P_M - CPR$ schemes for the 1D linear wave equation.

The conservation error per one cell defined as

$$Conserv. \quad Error \equiv \int_{V_i} \frac{\partial Q_i}{\partial t} \mathrm{d}x + \int_{\partial V_i} \vec{F_i} \cdot \vec{n} \mathrm{d}S \tag{3.31}$$

is monitored during the simulation and shown in Figure 3.4. Results show that the conservation error of $P_1P_4 - CPR - G$ and $P_2P_6 - CPR - G$ are always machine zero; while $P_1P_5 - CPR - G$, $P_2P_7 - CPR - G$ and $P_2P_8 - CPR - G$ are not conservative since the conservation constraints for the high-order reconstruction are not satisfied.

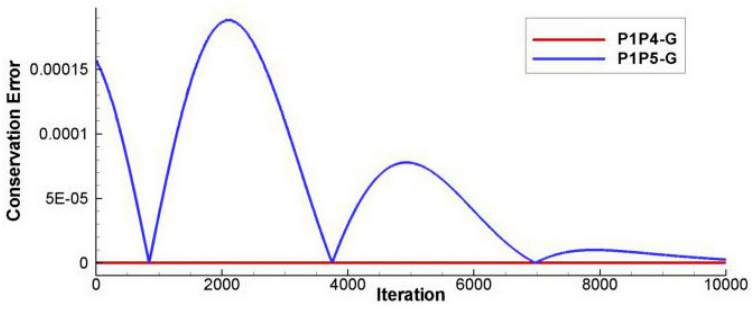

(a) $P_1P_M - CPR - G$

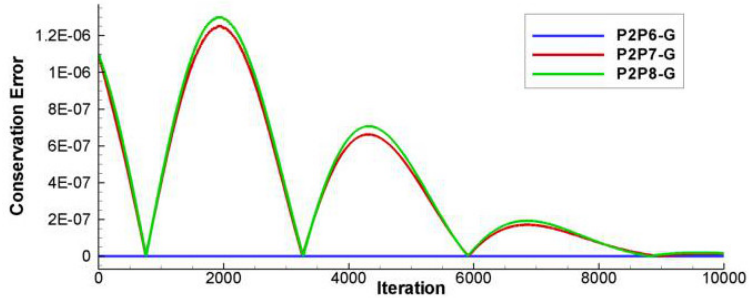

(b) $P_2P_M - CPR - G$

Figure 3.4: The history of the conservation error of one cell with $P_NP_M - CPR$ using the Gauss points as the solution points.

3.3 Fourier Analysis of the $P_NP_M - CPR$ Schemes

In order to assess the stability and accuracy of the $P_NP_M - CPR$ schemes, an analysis of the wave propagation properties for 1D schemes with different solution points and reconstruction stencil is performed. Consider the 1D linear advection equation

$$\frac{\partial Q}{\partial t} + a\frac{\partial Q}{\partial x} = 0 \tag{3.32}$$

with constant wave speed a and periodic boundary condition. The initial condition is assumed to be a harmonic wave

$$Q(x,0) = \hat{Q}e^{Ikx}, \tag{3.33}$$

where k is the wave number and $I = \sqrt{-1}$. The exact solution to Eq. 3.32 is

$$Q(x,t) = e^{-I\omega t}Q(x,0) = \hat{Q}e^{I(kx-\omega t)}. \tag{3.34}$$

Substituting Eq. 3.34 to Eq. 3.32, we obtain the exact dispersion relationship between the wave number k and the frequency ω, i.e., $\omega = ak$. Now consider a uniform mesh with element size Δx, solution points in local coordinate on element i are denoted as $\xi_j \in [-1,1], j = 1, ..., K$. The reconstructed P^m polynomial can be expressed as the summary of every unknowns times its P^m shape function

$$U_i = \sum_{j=1}^{K} Q_{i,j}\phi_{i,j} + \sum_{j=1}^{(K_m-K)/2} \left(Q_{i-1,K+1-j}\phi_{i-1,K+1-j} + Q_{i+1,j}\phi_{i+1,j}\right). \tag{3.35}$$

where $\phi_{i,j}$ are the shape functions. The upwind flux is used as the common flux as

$$F^{com}(Q_l, Q_r) = aQ_l. \tag{3.36}$$

So the discretized divergence of flux in computational domain can be written as

$$(F_\xi)_{i,j} = a(U_\xi)_{i,j} + [F^{com}_{i-1/2} - aU_i(-1)\}]g_l'(\xi_j) + [F^{com}_{i+1/2} - aU_i(1)]g_r'(\xi_j). \tag{3.37}$$

To calculate the eigenvalues of the discretized divergence operator of $P_N P_M - CPR$, the K local DOFs or unknowns are grouped together as a column vector $\mathbf{Q_i}$. From Eq. 3.34, Fourier mode of $\mathbf{Q_i}$ is given as

$$\mathbf{Q_i} = \tilde{\mathbf{Q}}e^{I(ki\Delta x-\omega t)}, \tag{3.38}$$

where $\tilde{\mathbf{Q}}$ is a complex column vector containing amplitude and phase data. So the only difference between solution vector of cell i-1 and that for the cell i is a phase shift $e^{Ik\Delta x}$, which leads to

$$\mathbf{Q_i} = e^{Ik\Delta x}\mathbf{Q_{i-1}}. \tag{3.39}$$

For the $P_N P_M - CPR$ method, the reconstructed solution polynomial U_i is used to compute the common flux. Let's assume the wave travels from left to right, the upwind common flux reduced to

$$\begin{cases} F_{i-1/2}^{upwind} = aU_{i-1}(1) \\ F_{i+1/2}^{upwind} = aU_i(1) \end{cases}, \tag{3.40}$$

which indicates only the left common flux correction need to be performed. Plug in the correction function on the left face $g_l(\xi)$ into Eq. 3.37

$$F_\xi = aU_\xi + a[U_{i-1}(1) - U_i(-1)]g_l'(\xi). \tag{3.41}$$

So the column vector $\mathbf{F}_\xi$ of flux divergence on each solution points ξ_j can be expressed as

$$\begin{aligned} \mathbf{F}_\xi &= a\mathbf{D}^-\mathbf{Q}_{i-1} + a\mathbf{D}\mathbf{Q}_i + a\mathbf{D}^+\mathbf{Q}_{i+1} \\ &+ a\mathbf{g}_\mathbf{l}'[\mathbf{R}^-\mathbf{Q}_{j-2} + \mathbf{R}\mathbf{Q}_{j-1} + \mathbf{R}^+\mathbf{Q}_j - (\mathbf{L}^-\mathbf{Q}_{j-1} + \mathbf{L}\mathbf{U}_j + \mathbf{L}^+\mathbf{Q}_{j+1})]. \end{aligned} \tag{3.42}$$

Here the $\mathbf{L}, \mathbf{R}$ stand for the reconstructed row vector at the left and right interface for every cell

$$\mathbf{L} = \{\phi_{i,j}(-1)\} \quad \mathbf{R} = \{\phi_{i,j}(+1)\} \tag{3.43}$$

as well as the derivative matrix $\mathbf{D}$

$$\mathbf{D} = \frac{\partial \phi_{i,j}(\xi_k)}{\partial \xi} \tag{3.44}$$

and correction vector $\mathbf{g}_l'$ defined as the derivative of the correction function evaluated on every solution points ξ_j

$$\mathbf{g'}_l = g_l'(\xi_j). \tag{3.45}$$

With the relationship between the current solution vector $\mathbf{Q}_i$ and the solution $\mathbf{Q}_{i-1}$ from its left neighbor (Eq. 3.39), the Flux divergence for $P_N P_M - CPR$ can be express as

$$(\mathbf{F}_\xi) = a\mathbf{S}\mathbf{Q}. \tag{3.46}$$

Here the divergence matrix $\mathbf{S}$ can be defined after introducing the dimensionless wave number $\hat{K} = k\Delta x$

$$\mathbf{S} = e^{-2I\hat{K}}\mathbf{g}_l'\mathbf{R}^- + e^{-I\hat{K}}(\mathbf{D}^- + \mathbf{g}_l'\mathbf{R} - \mathbf{g}_l'\mathbf{L}^-) + \mathbf{D} + \mathbf{g}_l'\mathbf{R}^+ - \mathbf{g}_l'\mathbf{L} + e^{I\hat{K}}(\mathbf{D}^+ - \mathbf{g}_l'\mathbf{L}^+). \quad (3.47)$$

So the semi-discretized wave equation with $P_N P_M - CPR$ method on this uniform mesh yields an expression of the following form

$$\frac{\partial \mathbf{Q}_i}{\partial t} + a\frac{2}{\Delta x}\mathbf{S}\mathbf{Q}_i = 0. \quad (3.48)$$

After introducing the dimensionless numerical frequency $\hat{\Omega} = \omega\Delta x/a$, previous equation produces a homogeneous system of linear equations

$$(-I\hat{\Omega}\mathbf{E} - 2\mathbf{S})\tilde{\mathbf{Q}} = 0. \quad (3.49)$$

For a non-trivial solution, the determinant of the corresponding matrix should be equal to zero

$$|2I\mathbf{S} - \hat{\Omega}\mathbf{E}| = 0, \quad (3.50)$$

where unknown $\hat{\Omega}$ is the eigenvalue of complex matrix $2I\mathbf{S}$ and the Fourier footprint $-I\hat{\Omega}$ can be defined. Compared with the exact dispersion relationship in dimensionless form $\hat{\Omega} = \hat{K}$, the exact Fourier footprint should be equal to $-IK$. So the real part of Fourier footprint represents the diffusive behavior which should not be positive at any wave numbers to keep the scheme stable while the imaginary part is a measure of dispersive properties of the numeric scheme.

3.3.1 P^m Reconstruction Stencil

In this section, the $P_1P_3 - CPR$ scheme is used to show the accuracy and stability of $P_NP_M - CPR$ method with different reconstruction stencils. For $P_1P_3 - CPR$ with incomplete stencils, there are three different approaches to choose the DOFs from the neighboring cells. The P^m reconstruction can be performed by symmetrically utilizing the nearest solution points from its neighbors or using one-sided DOFs from the upwind or downwind neighboring cell only. The Fourier footprint of the one sided upwind and downwind reconstruction is shown in Figure 3.5. It is seen that the $P_1P_3 - CPR$ with an upwind stencil has positive real parts of the footprint at some wave numbers, which indicates an unstable scheme, while there is no numerical dissipation for the stencil with the downwind cell. This result indicates that the interaction between neighbors should be provided through the Riemann flux only.

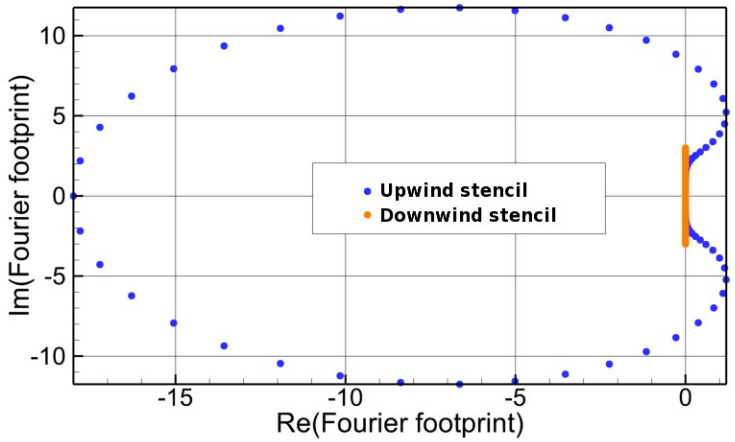

Figure 3.5: Fourier footprints of the $P_1P_3 - CPR - G - I2$ with the upwind stencil and the downwind stencil.

Figure 3.6 shows the dispersion and diffusion properties of the $P_1P_3 - CPR - G$ with complete and incomplete symmetric stencils. For symmetric stencils with Gauss points, the real parts of the footprints are always below zero and yield stable schemes. Compared

with the incomplete stencil with nearest points, the scheme with complete stencil have less dispersion error at the expense of more numerical dissipation.

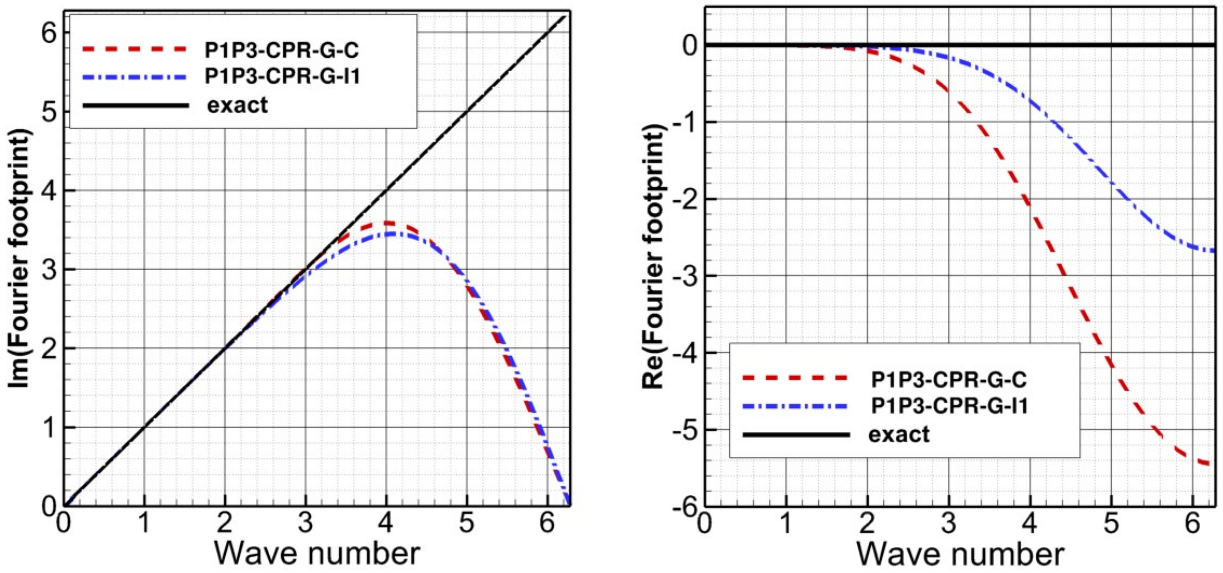

(a) $P_1P_3 - G$ $Im(-i\omega)$ vs k (b) $P_1P_3 - G$, $Re(-i\omega)$ vs k

Figure 3.6: Dispersion (left) and diffusion (right) curves of $P_1P_3{-}CPR{-}G$ with the complete and the incomplete stencils.

3.3.2 Solution Point Distribution

In [51], H.T. Huynh shows that the CPR method is independent of the solution point positions. First, we will give a brief review of his proof. For the CPR method, the approximate solution polynomial Q_i is supported by its local DOFs $\hat{\mathbf{Q}}_i = \{\hat{Q}_{i,j}\}$ only

$$Q_i = \sum_j^K \hat{Q}_{i,j}\phi_j, \tag{3.51}$$

where the Lagrangian basis denoted as ϕ_j defined on each solution points $\xi_j = \{\xi_j\}$. Assume there is another set of solution points $\tilde{\xi} = \{\tilde{\xi}_j\}$ and let $\tilde{Q}_{i,j}$ be the solution value corresponding

to $\tilde{\xi}_j$,

$$\tilde{Q}_{i,l} = \sum_{j}^{K} \hat{Q}_{i,j}\phi_j(\tilde{\xi}_l). \tag{3.52}$$

This generates the transformation relationship between the unknowns $\hat{Q}_{i,j}$ and $\tilde{Q}_{i,j}$ corresponding to the different solution points in the matrix form

$$\hat{\mathbf{Q}}_i = \mathbf{M}\tilde{\mathbf{Q}}_i, \tag{3.53}$$

where Vandermonde matrix $\mathbf{M}$ defined as $\mathbf{M} = \left\{\phi_j(\tilde{\xi}_i)\right\}$. Performing same steps for Fourier analysis of $P_N P_M - CPR$ to CPR method leads to the semi-discretized wave equation for unknowns $\tilde{\mathbf{Q}}_i$ on solution points ξ_j as

$$\frac{\partial \tilde{\mathbf{Q}}_i}{\partial t} + a\frac{2}{\Delta x}\mathbf{S}\tilde{\mathbf{Q}}_i = 0. \tag{3.54}$$

Then substitute Eq. 3.53 into Eq. 3.53, we obtain

$$\frac{\partial \hat{\mathbf{Q}}_i}{\partial t} + a\frac{2}{\Delta x}\mathbf{M}\mathbf{S}\mathbf{M}^{-1}\hat{\mathbf{Q}}_i = 0, \tag{3.55}$$

or the semi-discretized wave equation for unknowns $\hat{\mathbf{Q}}_i$ on $\hat{\xi}_j$

$$\frac{\partial \hat{\mathbf{Q}}_i}{\partial t} + a\frac{2}{\Delta x}\hat{\mathbf{S}}\hat{\mathbf{Q}}_i = 0. \tag{3.56}$$

This indicates that the discretized divergence operator $\hat{\mathbf{S}}$ defined on the new set of solution points $\tilde{\xi}$ is similar to the matrix $\mathbf{S}$

$$\hat{\mathbf{S}} = \mathbf{M}\mathbf{S}\mathbf{M}^{-1}. \tag{3.57}$$

So they have the same eigenvalues and consequently the Fourier footprint of CPR method is independent of the solution points distribution. However, this is not true for $P_N P_M - CPR$ schemes, since the reconstructed P^m polynomial U_i does not satisfy Eq. 3.53. The dispersion

and dissipation properties of $P_N P_M - CPR$ varies with the different solution points and needs to be investigated. Here Fourier analysis is also used to guide the selection of the optimal solution points. The order of accuracy of a numerical method in a Fourier analysis needs to be defined. The principal eigenvalue $S(\tilde{K})$ which approximates the exact eigenvalue $-I\tilde{K}$ of the operator $-\partial/\partial x$ can be expanded using a Taylor series in $\tilde{K}$ [51]

$$S(\tilde{K}) = -I\tilde{K} + O(\tilde{K}^{m+1}), \tag{3.58}$$

which indicates a global $m-th$ order. The error of principal eigenvalue can be defined as

$$E(\tilde{K}) = |S(\tilde{K}) + I\tilde{K}|, \tag{3.59}$$

and the order of accuracy is given by

$$m \approx Log_2\left(\frac{E(\tilde{K})}{E(\tilde{K}/2)}\right) - 1. \tag{3.60}$$

Figure 3.7 shows the order of accuracy and the maximum real part of the Fourier footprint vary with the solution points parameter ξ for $P_1 P_M - CPR$ and $P_2 P_M - CPR$. The solution points we chosen for $P_1 P_M - CPR$ are symmetrically defined as $\{-\xi, \xi\}$, while the solution points for $P_2 P_M - CPR$ are defined as $\{-\xi, 0, \xi\}$. In addition to $P_N P_M - CPR$ with the incomplete stencil using the nearest DOFs, the incomplete stencil schemes with the furthest DOFs from the neighboring cells are added here too, which can be used to analyze the accuracy of the complete stencil schemes with Lobatto points when $\xi \to 1$. The result shows that the order of accuracy of CPR schemes is independent of the solution points. Furthermore, super-convergence properties of P^1 and P^2 CPR method with DG correction functions are observed, whose order of accuracy is 4 and 6 respectively. This agrees with the super-accuracy of the CPR method, which is $2k+2$ for a P^k scheme with DG correction function [51].

Due to the P^m reconstruction, the $P_N P_M - CPR$ formula does not inherit the solution point independent property from the CPR method. As shown in Figure 3.7, the accuracy and stability of $P_N P_M - CPR$ method are highly dependent on the solution point distribution. Some solution points cannot guarantee a stable $P_N P_M - CPR$ scheme and the $P_1 P_4 - CPR$ with the complete stencil is not stable with any solution points. For the $P_N P_M - CPR$ method, the optimal order of accuracy only occurs at one special solution points distribution, which is close to the Gauss points but changes with the order of P^m reconstruction performed. The standard Gauss quadrature point is the best solution points for $P_1 P_3 - CPR - I1$ with the nearest DOFs, $P_2 P_4 - CPR - C$, $P_2 P_4 - CPR - I1$ with the nearest/furthest DOFs and $P_2 P_6 - CPR - C$. That's the reason we obtain the optimal order of accuracy with Gauss points from numerical tests for those schemes in Session 3. With the increase of SP coordinate, the $P_N P_M - CPR$ with incomplete stencil from furthest neighbor points approach the $P_N P_M - CPR$ scheme with Lobatto point. It is shown that the order of accuracy decrease with the increase of ξ when it approach 1, which explains the reason of one order of accuracy loss for $P_N P_M - CPR$ with Lobatto point in previous numerical tests.

Figure 3.8 compares the convergence rate for $P_1 P_5 - G - C$, $P_2 P_6 - G - I2$ with the nearest DOFs and $P_2 P_8 - G - C$ in Fourier analysis and numerical test. The solution points are chosen as the standard Gauss quadrature point, the optimized solution point from the Fourier analysis and the solution point with $\xi = 0.95$. Results show that at the same set of solution points, similar convergence rate in the Fourier analysis and the numerical test are obtained. In Figure 3.8, those schemes with optimized solution points can produce the expected order of accuracy, which is one order higher than those with Gauss point. Numerical results of 1D $P_N P_M - CPR$ schemes with the best solution points are summarized in Figure 3.9. To obtain the expected convergence rate, the solution points for $P_N P_M - CPR$ methods need to be chosen at the optimal position.

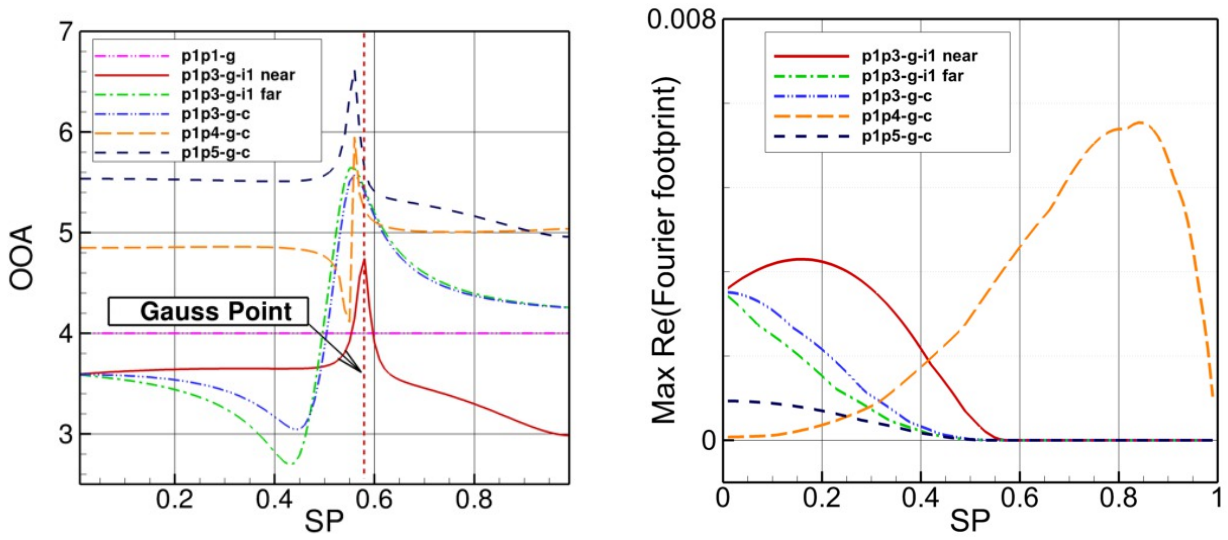

(a) $P_1P_M - G$ OOA vs SP

(b) $P_1P_M - G$ Maximum $Re(-i\omega)$ vs SP

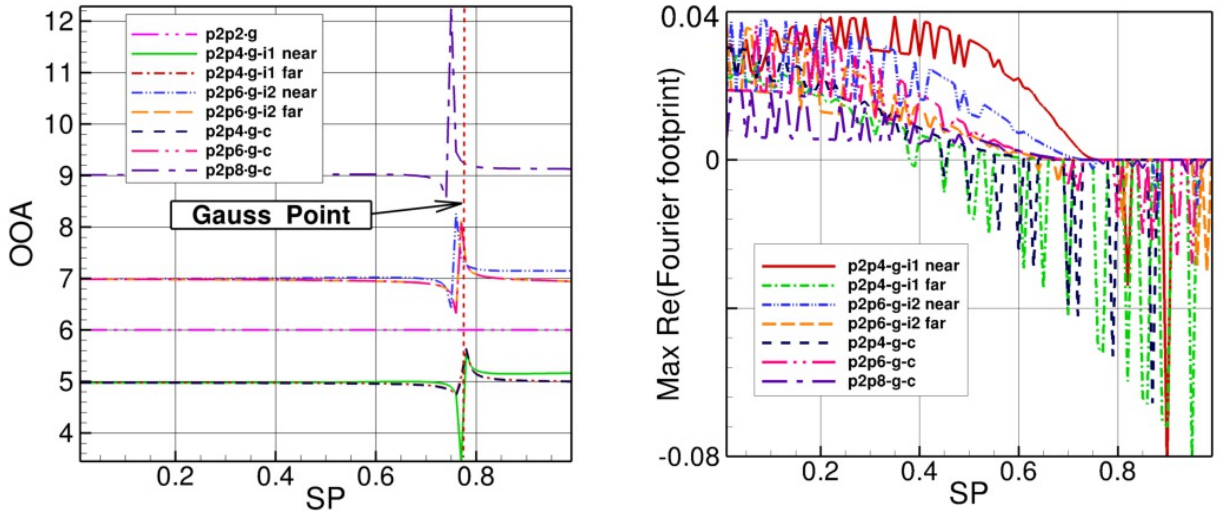

(c) $P_2P_M - G$ OOA vs SP

(d) $P_2P_M - G$ Maximum $Re(-i\omega)$ vs SP

Figure 3.7: Order of accuracy and maximum Re$(-i\omega)$ varies with solution points for $P_1P_M - G$ and $P_2P_M - G$.

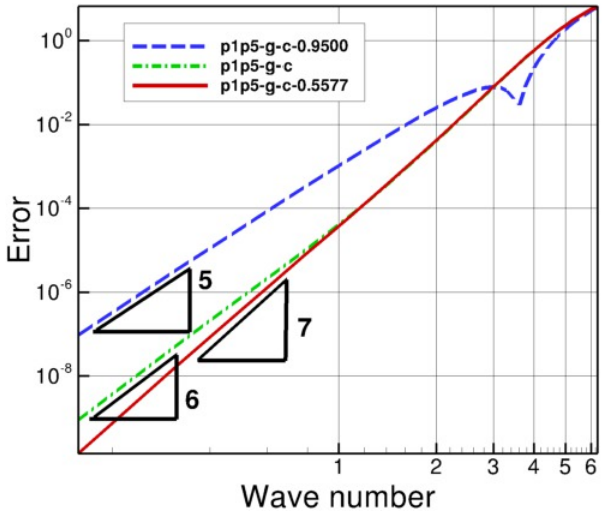

(a) P_1P_5-G-C Fourier analysis

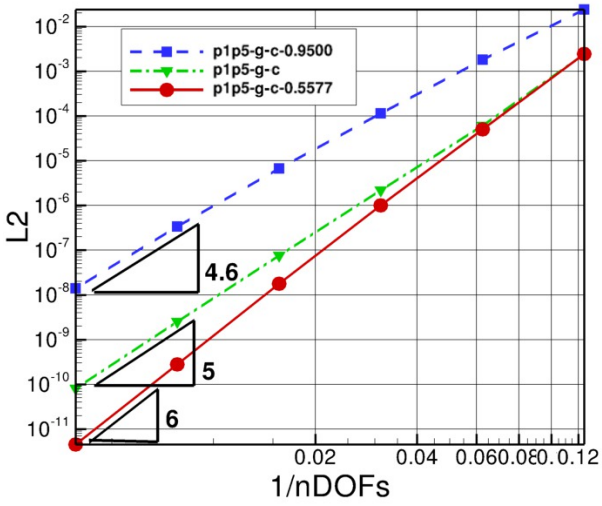

(b) P_1P_5-G-C numerical test

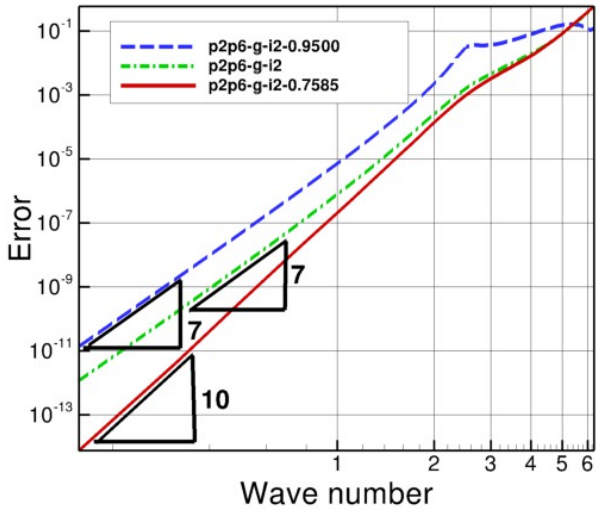

(c) P_2P_6-G-I2 Fourier analysis

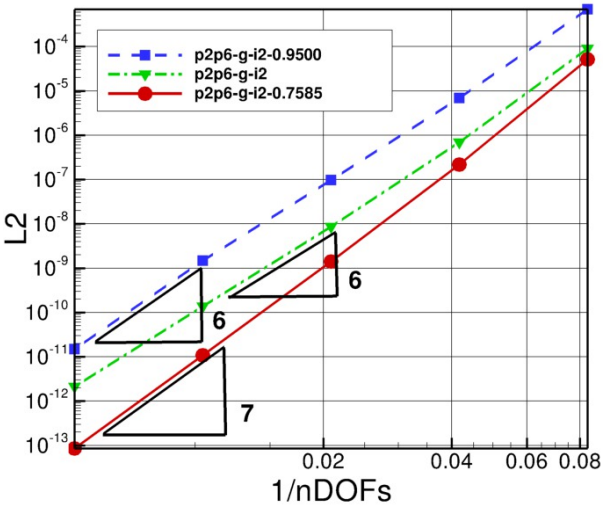

(d) P_2P_6-G-I2 numerical test

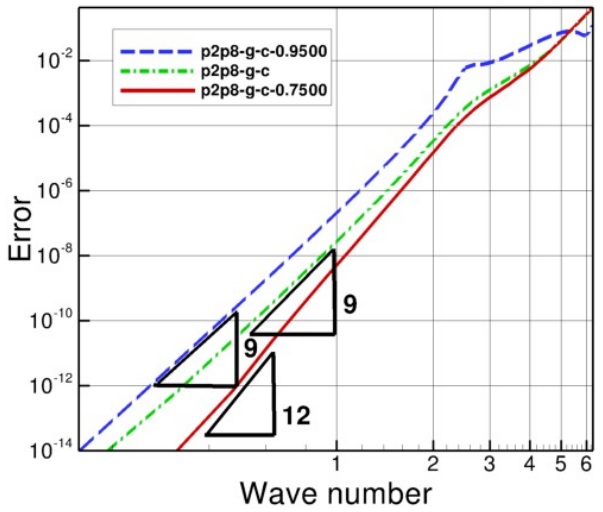

(e) P_2P_8-G-C Fourier analysis

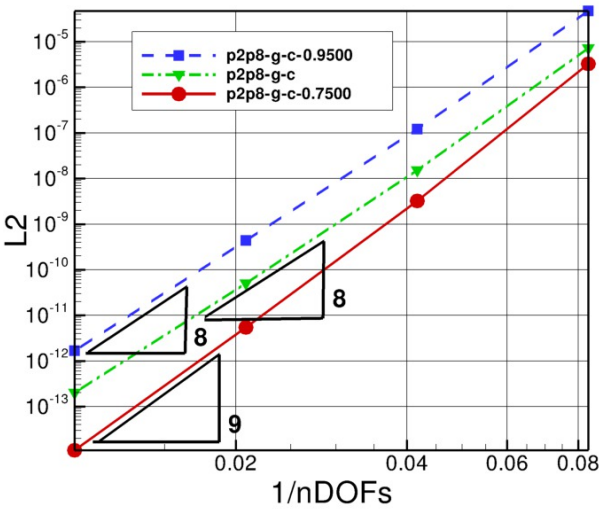

(f) P_2P_8-G-C numerical test

Figure 3.8: The convergence rate of P_1P_5-G-C, P_2P_6-G-I2 and P_2P_8-G-C with different SPs(ξ) in the Fourier analysis and the numerical tests.

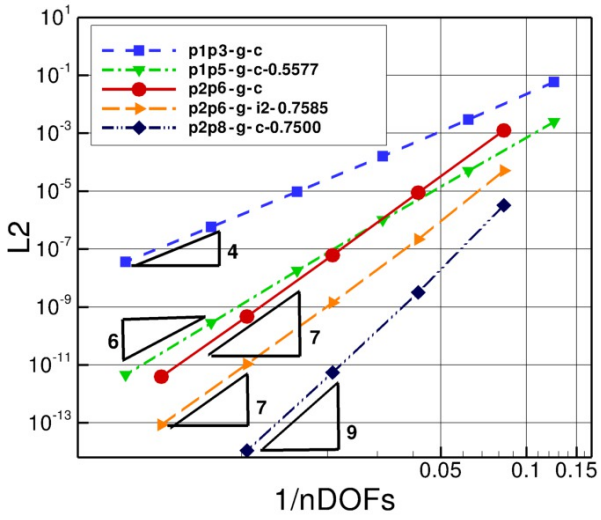

Figure 3.9: L_2 error of $P_N P_M - CPR$ with the optimal solution points for the 1D wave equation.

3.4 Extension to the Navier-Stokes Equations

3.4.1 2D Formulation for the Simplex

The extension of the $P_N P_M - CPR$ schemes to a simplex is similar to the 1D formulation. Again we have two choices to distribute the solution points, as shown in Figure 3.10. In order to maintain compactness of the reconstruction stencil, we limit it to include the current cell and its immediate face neighbors only. For the 2D triangle mesh we have at most 3 face neighbors for each element, and total number of $n_s = 4K_n$ SPs in the stencil with Gauss points. In this case, flux points are located at Gauss points along each edge, and Gauss quadrature points given in Ref. [96] are used as the SPs. If the SPs are Lobatto points, along each edge, the flux points are located at Legendre-Gauss-Lobatto points, while the interior solution points given in Ref. [45] are used. For Lobatto points, we cannot include all of the SPs to the stencil because many are collocated, therefore, the total number of DOFs

available in the P^m reconstruction stencil decreases to $n_s = 4K_n - 3(n+1)$. For both cases, the corresponding quadrature weights can be obtained using the standard quadrature rule.

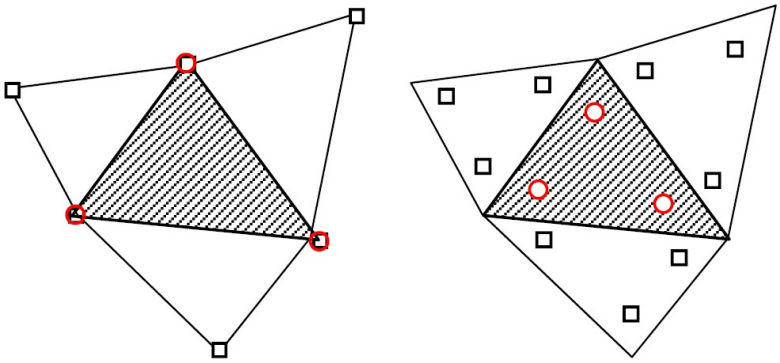

(a) Lobatto points as SPs (b) Gauss points as SPs

Figure 3.10: Schematic of Labatto and Gauss points as the solution points (◯: the current element's SPs, □: the neighbors' SPs).

As shown in Figure 3.11, all elements in the P^m stencil are transformed from the physical domain $\vec{r} = (x, y)$ into the computational domain by the current element's mapping function, which converts the current cell into a standard right triangle defined as

$$T = \left\{ \vec{\xi} = (\xi, \eta) | (\xi, \eta) \geq 0; \xi + \eta \leq 1 \right\}. \tag{3.61}$$

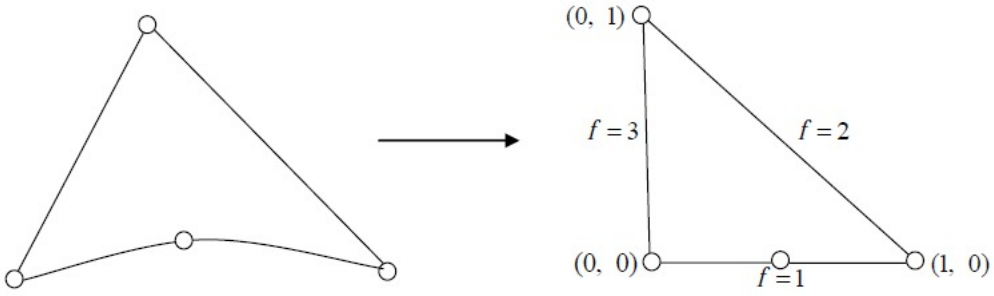

Figure 3.11: Transformation of general elements to the standard element.

Sometimes we do not have enough neighbors at the boundary. In this case, we need to use a different approach to perform the reconstruction near the boundary. There are at least

two approaches for the P^m reconstruction at the boundary cells. One is using local DOFs only for boundary cells and the other is to perform one-sided P^m reconstruction, as shown in Figure 3.12. For one-sided P^m reconstruction, in order to increase the number of DOFs in the stencil, the computational grid should be generated to make sure every boundary cell has at most one boundary face. With a local reconstruction approach, we should put more DOFs at the boundary cells and use a degree m polynomial to maintain the order of accuracy near the boundaries and flux conservation between boundary cells and interior cells. From numerical tests, both of them can achieve the optimal order of accuracy. However, the local reconstruction approach is more stable than the one-sided P^m reconstruction, especially for curved boundaries.

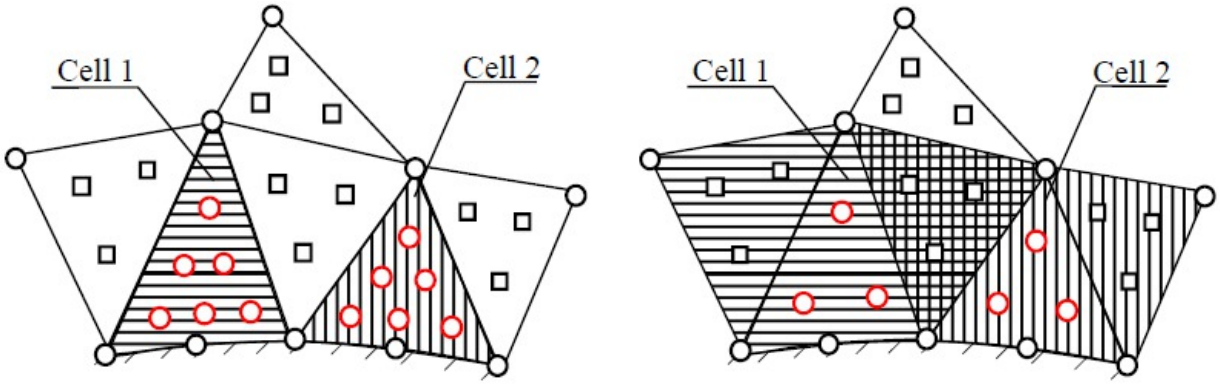

(a) Local P^m reconstruction (b) One-sided P^m reconstruction

Figure 3.12: P^m reconstruction for P1P2-G at the boundary cells (◯: the current element's SPs, □: the neighbors' SPs)

With the proper reconstruction stencil, the degree m polynomial can be built following the same constrained least squares technique for the 1D $P_N P_M - CPR$ schemes. The hybrid schemes are uniquely defined once the reconstruction polynomial U_i is determined.

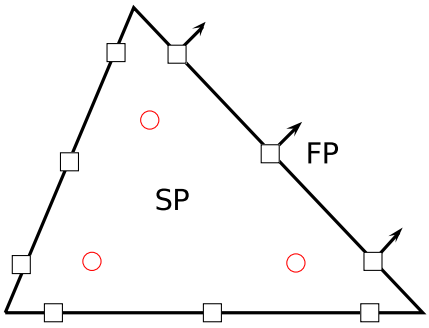

Figure 3.13: SPs and FPs for the $P_1P_2 - CPR - G$ scheme with Gauss points.

To correct the flux divergence, first the normal flux difference is assumed to be of order m along each face, as shown in Figure 3.13. As a result, extra flux points are added on the faces to support a degree m polynomial. Then new correction coefficients $\alpha_{j,f,l}$ are derived from the lifting operator given in Eq. 2.6. Obviously, the reconstruction polynomial is used to compute the flux difference at all the flux points. Similar to the 1D $P_NP_M - CPR$ schemes, the reconstructed polynomial U_i is used to compute the flux divergence, perform surface corrections and finally generate a high-order update for the DOFs as:

$$\frac{\partial Q_{i,j}}{\partial t} + \Pi_j \left(\vec{\nabla} \cdot [\vec{F}^i(U_i)] \right) + \frac{1}{|V_i|} \sum_{f \in \partial V_i} \sum_l \alpha_{j,f,l} [F^n(U_i, U^+, \vec{n})]_{f,l} S_f = 0. \tag{3.62}$$

The above 2D schemes are tested with a 2D linear wave equation:

$$\frac{\partial Q}{\partial t} + \frac{\partial Q}{\partial x} + \frac{\partial Q}{\partial y} = 0 \quad x \in [-1, 1], \; y \in [-1, 1] \tag{3.63}$$

under the initial condition $Q(x, y, 0) = sin\pi(x + y)$. The computation is carried out on a set of irregular triangular mesh, as shown in Figure 3.14. The L_2 errors are plotted in Figure 3.14. The results show that we get an extra order of accuracy with the $P_1P_M - CPR$ and $P_2P_M - CPR$ schemes. In order to enhance the robustness of the P^m reconstruction, we need to use more DOFs in P^m stencil than needed. Also, the incomplete stencils are more accurate than the complete stencil. This is similar to the 1D results.

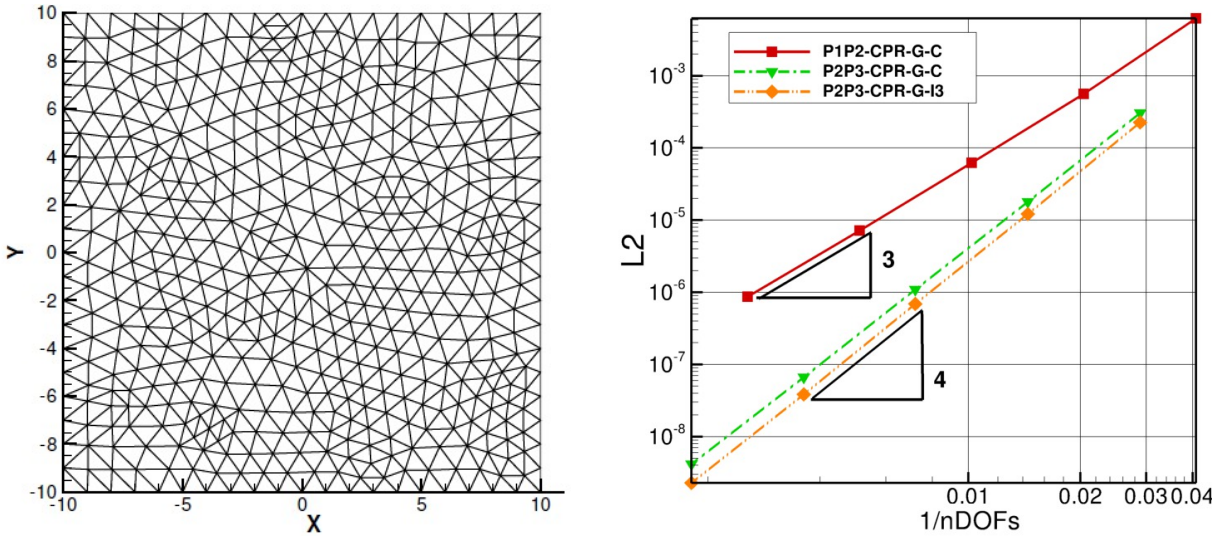

(a) Mesh (b) L_2error

Figure 3.14: Computational mesh and L_2 error of $P_N P_M - CPR$ for the 2D wave equation.

3.4.2 Extension to the Navier-Stokes Equations

With the description given for the $P_N P_M - CPR$ formulation for conservation laws, the extension to the Navier-Stokes equations is straightforward. The 2D compressible Navier-Stokes equations can be expressed as the following conservation form:

$$\frac{\partial Q}{\partial t} + \frac{\partial F(Q, \nabla Q)}{\partial x} + \frac{\partial G(Q, \nabla Q)}{\partial y} = 0, \tag{3.64}$$

where the state variables $Q = [\rho, \rho u, \rho v, E]^T$ is the vector of conserved variable, F and G includes both the inviscid and the viscous flux vectors, i.e., $F = F^i - F^v$, $G = G^i - G^v$. The inviscid flux vectors are defined by

$$F^i = \begin{pmatrix} \rho u \\ p + \rho u^2 \\ \rho uv \\ u(E+p) \end{pmatrix}, G^i = \begin{pmatrix} \rho v \\ \rho uv \\ p + \rho v^2 \\ v(E+p) \end{pmatrix}, \tag{3.65}$$

and the viscous flux vectors can be written as

$$F^v = \mu \begin{pmatrix} 0 \\ 2u_x + \lambda(u_x + v_y) \\ v_x + u_y \\ u\left[2u_x + \lambda(u_x + v_y)\right] + v(v_x + u_y) + \frac{c_p}{Pr} T_x \end{pmatrix},$$

$$G^v = \mu \begin{pmatrix} 0 \\ v_x + u_y \\ 2v_y + \lambda(u_x + v_y) \\ u(v_x + u_y) + v\left[2u_y + \lambda(u_x + v_y)\right] + \frac{c_p}{Pr} T_y \end{pmatrix}. \tag{3.66}$$

Here, p, u, v, ρ and E are pressure, velocity component in x and y directions, density and total energy respectively. The total energy is related to the other variables according to

$$E = \frac{p}{\gamma - 1} + \frac{1}{2}\rho(u^2 + v^2). \tag{3.67}$$

In Eq. 3.66, μ is the dynamic viscosity, c_p is the specific heat at constant pressure, Pr is the Prandtl number, and T is the temperature. The ratio of specific heats γ is assumed to be a constant, which is 1.4 for air.

For hybrid $P_N P_M - CPR$ formulation, all of conserved variables Q, except the unsteady time variation term $\frac{\partial Q}{\partial t}$, are approximated by the reconstructed degree m polynomial U. The viscous fluxes F^v and G^v are functions of both the conserved variables U and their gradient ∇U. For the divergence of the viscous flux, we follow the formulation in Ref. [5], by adding

a new variable

$$R = \nabla U$$

to convert the Navier-Stokes equations from 2^{nd} order partial derivative equation (PDE) into 2 coupled 1st order PDEs

$$\begin{cases} \frac{\partial Q}{\partial t} + \frac{\partial F^i(U)}{\partial x} + \frac{\partial G^i(U)}{\partial y} + \frac{\partial F^v(U,R)}{\partial x} + \frac{\partial G^v(U,R)}{\partial y} & = 0 \\ R - \nabla U & = 0 \end{cases}.$$

Then R is solved in the $P_N P_m - CPR$ framework, this will result in a collocation penalty formulation

$$R_{i,j} = (\nabla U_i)_j + \frac{1}{|V_i|} \sum_{f \in \partial V_i} \sum_l \alpha_{j,f,l} [\tilde{U}]_{f,l} S_f, \tag{3.68}$$

where $[\tilde{U}]_{f,l} = U^{com}_{f,l} - [U_i]_{f,l}$, $U^{com}_{f,l}$ is the common solution on interface f, and $[U_i]_{f,l}$ is the solution within cell i on face f. The definition of $U^{com}_{f,l} = U^{com}(U^+_{f,l}, U^-_{f,l}, \vec{n_f})$ varies with different approaches to discretize the viscous terms.

After this, the viscous fluxes at solution points are evaluated by

$$F^v_{i,j} = F^v(U_{i,j}, R_{i,j}),\ G^v_{i,j} = G^v(U_{i,j}, R_{i,j}). \tag{3.69}$$

And with the viscous fluxes evaluated at the solution points, $\frac{\partial F^v}{\partial x}$ and $\frac{\partial G^v}{\partial y}$ can be easily obtained through the same approach of reconstructing degree m polynomial U from Q. Besides those analytic derivatives at SPs, common viscous fluxes at the interfaces are also needed for correcting the interior divergence of the viscous flux, which are defined

$$F^{v,com}_{i,j} = F^v(U^{com}_{i,j}, \nabla U^{com}_{i,j}),\ G^{v,com}_{i,j} = G^v(U^{com}_{i,j}, \nabla U^{com}_{i,j}).$$

Finally the $P_N P_M - CPR$ formulation for the Navier-Stokes equations is expressed as:

$$\frac{\partial Q_{i,j}}{\partial t} + \Pi_j \left(\vec{\nabla} \cdot [\vec{F}^i(U_i)] \right) - \Pi_j \left(\vec{\nabla} \cdot [\vec{F}^v(U_i, R_i)] \right) + \frac{1}{|V_i|} \sum_{f \in \partial V_i} \sum_l \alpha_{j,f,l} [F^n]_{f,l} S_f = 0, \quad (3.70)$$

where the total flux differences is

$$[F^n] = F^{i,n}_{com} - F^{i,n}(U_i) - F^{v,n}_{com} + F^{v,n}(U_i, R_i)$$

In the current framework, the different approaches to discretize the viscous terms only depends on how to compute the common solution U_{com} and common gradient $\nabla U^{com}_{f,l} = \nabla U^{com}(\nabla U^+_{f,l}, \nabla U^-_{f,l}, U^+_{f,l}, U^-_{f,l}, \vec{n}_f)$ at the cell interface. In the following sections, the ways to define U_{com} and ∇U^{com} in both BR2 and interior penalty approaches are described.

3.4.2.1 The BR2 Method

The common solution in BR2 is simply the average solution on two sides of the face

$$U^{com}_{f,l} = \frac{U^-_{f,l} + U^+_{f,l}}{2}$$

For the common gradient, the definition can be written as

$$\nabla U^{com}_{f,l} = \frac{1}{2}(\nabla U^-_{f,l} + \lambda^-_{f,l} + \nabla U^+_{f,l} + \lambda^+_{f,l})$$

where $\nabla U^-_{f,l}$ and $\nabla U^+_{f,l}$ are the gradients from the reconstruction of the left and right cells, while $\lambda^-_{f,l}$ and $\lambda^+_{f,l}$ are corrections to the gradients only due to the common solution on face f

$$\lambda^-_{f,l} = \frac{1}{|V^-|} \sum_m \beta_{f,l,m} [\tilde{U}]^-_{f,m} \vec{n}_{f,m} S_f,$$

$$\lambda_{f,l}^{+} = \frac{1}{|V^{+}|} \sum_{m} \beta_{f,l,m} [\tilde{U}]_{f,m}^{+} (-\vec{n}_{f,m}) S_f,$$

where $[\tilde{U}]_{f,l}^{-} = U_{f,l}^{com} - U_{f,l}^{-}$, $[\tilde{U}]_{f,l}^{+} = U_{f,l}^{com} - U_{f,l}^{+}$. $\beta_{f,l,m}$ is the coefficient of correction due to face f. $\beta_{f,l,m}$ can be extracted from coefficients $\alpha_{j,f,l}$. Due to the symmetry of triangles, $\beta_{f,l,m}$ for any face f is identical for a fixed distribution of flux points, therefore the face index in β is omitted here on.

3.4.2.2 The Interior Penalty Method

In BR2, the penalty at one FP is a linear combination of the solution differences of all FPs on that face. In interior penalty (IP) method, the correction is computed in a 1D manner which only depends on the solution difference at that point.

The IP uses the same average to calculate the common solution as BR2 method, which is just the average of solutions on two sides of the common face

$$U_{f,l}^{com} = \frac{U_{f,l}^{-} + U_{f,l}^{+}}{2}.$$

And the common gradient is still of the form

$$\nabla U_{f,l}^{com} = \frac{1}{2} (\nabla U_{f,l}^{-} + \lambda_{f,l}^{-} + \nabla U_{f,l}^{+} + \lambda_{f,l}^{+})$$

However, it comes with simplified correction terms $\lambda_{f,l}^{-}$ and $\lambda_{f,l}^{+}$ defined as

$$\lambda_{f,l}^{-} = \frac{1}{|V^{-}|} \beta_l [\tilde{U}]_{f,l}^{-} \vec{n}_{f,l} S_f,$$

$$\lambda_{f,l}^{+} = \frac{1}{|V^{+}|} \beta_l [\tilde{U}]_{f,l}^{+} (-\vec{n}_{f,l}) S_f,$$

where β_l is a constant for any l. For the $P_N P_M - CPR$ method with the IP, we need to use a bigger correction coefficient β_l than the conventional CPR method to enhance the stability.

3.5 Numerical Results

In this section, numerical experiments are carried out for the compressible Euler and Navier-Stokes equations.

3.5.1 Accuracy Study with the Vortex Propagation Problem

First, we test the accuracy of the $P_N P_M - CPR$ schemes for the 2D Euler equations. The isotropic vortex propagation problem from Ref. [92] is used. The initial condition has a mean flow of $\{\rho, u, v, p\} = \{1, 1, 1, 1\}$ onto which an isotropic vortex is added. The isotropic vortex consists of perturbations in u, v and temperature T, but no perturbation in entropy $S = p/\rho^r$:

$$(\delta u, \delta v) = \frac{\epsilon}{2\pi} e^{0.5(1-r^2)}(-y, x), \tag{3.71}$$

$$\delta T = -\frac{(\gamma - 1)\epsilon^2}{8\gamma\pi^2} e^{1-r^2}, \tag{3.72}$$

$$\delta S = 0, \tag{3.73}$$

where $r^2 = x^2 + y^2$ and the vortex strength $\epsilon = 5$. The exact solution of this problem is just the passive convection of the isotropic vortex with the mean velocity. Figure 3.15 shows the density contours at different time steps.

In the numerical simulation, the computational domain is taken to be $[-10, 10] \times [-10, 10]$ with periodic boundary conditions imposed on all of the outer boundaries. The same irregular computational meshes for the 2D wave equation are used here (Figure 3.14). The computation is carried out until t = 1. The L_2 error is plotted in Figure 3.15. For the Euler equations, we can still get 1 order benefit for $P_1 P_M - CPR$ schemes and $P_2 P_M - CPR$

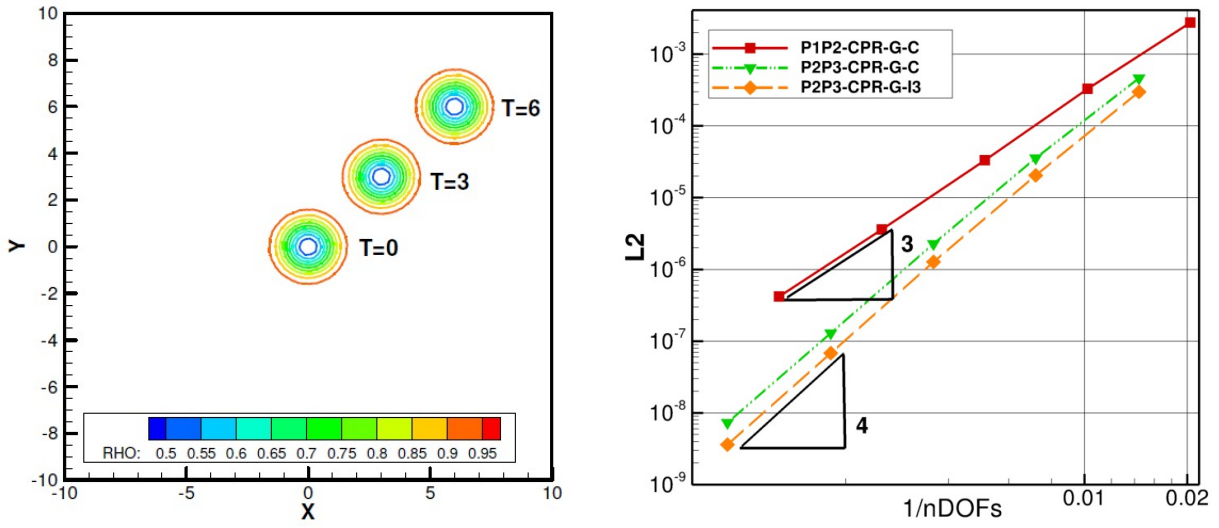

(a) density contour

(b) L_2error

Figure 3.15: Density contours and L_2 error of the vortex propagation problem.

schemes. Furthermore, the results with the incomplete stencil are more accurate than the complete stencil which is the similar to the previous test.

3.5.2 Flow in a Channel with a Smooth Bump

This internal aerodynamic problem is selected to test the order of accuracy of $P_N P_M - CPR$ schemes with curved boundaries. The channel has a height of 0.8 unit and a length of 3 unit. The bump is defined as

$$y = 0.0625e^{-25x^2}. \tag{3.74}$$

The coarsest computational mesh which has a total of 220 cells is shown in Figure 3.16. The smooth bump is represented with quadratic segments. Note that the mesh has mixed P^1/P^2 elements and the P^2 elements are used only at the wall boundary. Characteristic boundary conditions are used at both the inlet and outlet. The simulation is started from a uniform free stream with Mach number 0.5 everywhere.

In order to increase the number of DOFs in the one-sided P^m reconstruction stencil, the computational grid is generated to make sure every boundary cell has at most one boundary

face. The computed Mach contour of $P_2P_3 - CPR - G$ scheme is shown in Figure 3.16. The L_2 norms of entropy error are plotted in Figure 3.17. Since the biggest entropy error is near the wall boundary, the proper P^m reconstruction on the boundary cells are needed to achieve the optimal order of accuracy for P_1P_2 and P_2P_3 CPR schemes. The results indicate that with the same degree of freedom, $P_NP_M - CPR$ schemes with wall boundaries can achieve 1 order higher than the original CPR schemes.

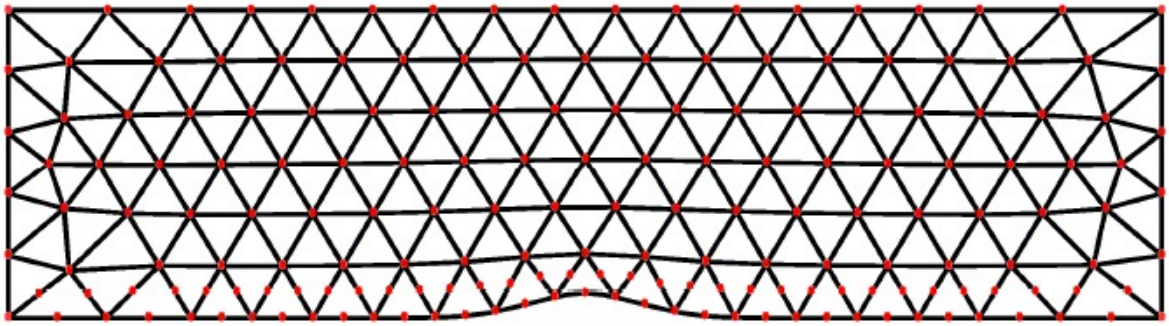

(a) Coarsest mesh

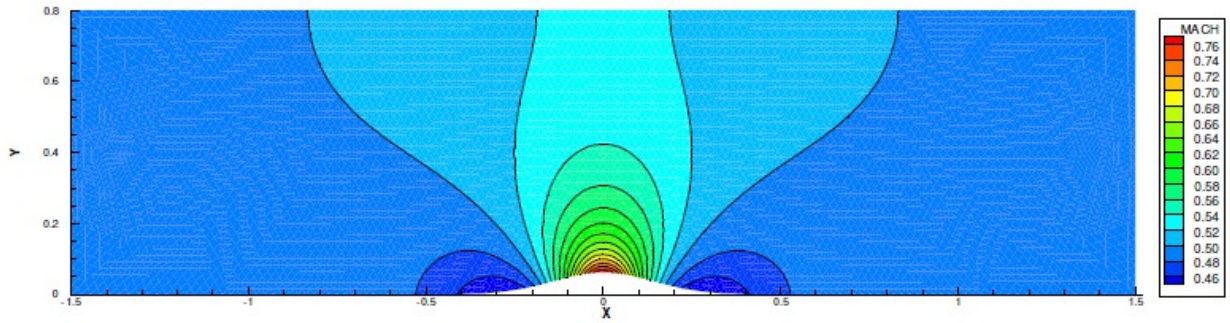

(b) Mach contour

Figure 3.16: The computational mesh and Mach contours of $P_2P_3 - CPR - G - C$ for the smooth bump problem.

3.5.3 Accurate Study with the 2D Compressible Couette Flow

The compressible Couette flow is used to assess the accuracy of the $P_NP_M - CPR$ method for 2D Navier-Stokes equations. In this problem, the laminar flow is driven by viscous force

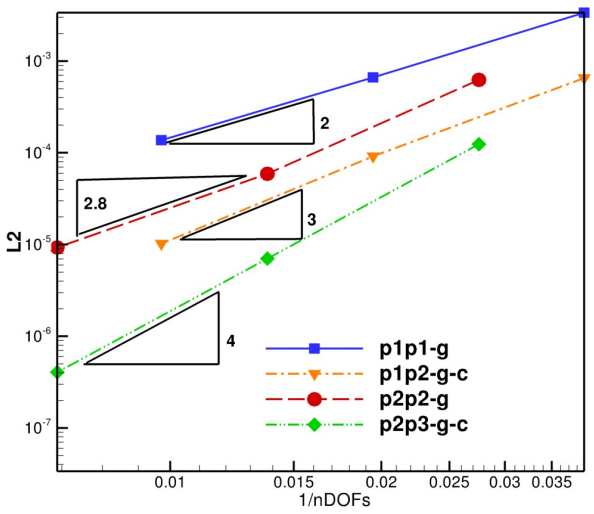

Figure 3.17: L_2 error of the $P_N P_M - CPR$ schemes for the smooth bump problem.

in the space between two parallel moving plates. The speed of the upper wall is set to be U=0.3 with constant temperature $T_1 = 0.85$. The lower wall is fixed and the temperature is set to be $T_0 = 0.8$. The dynamic viscosity of the fluid is $\mu = 0.01$. The analytic solution is:

$$u = \frac{U}{H} y,\ v = 0,$$

$$p = const,\ \rho = \frac{p}{RT},$$

$$T = T_0 + \frac{y}{H}(T_1 - T_0) + \frac{\mu U^2}{2k}\frac{y}{H}(1 - \frac{y}{H}),$$

where R is the gas constant and k is the thermal conductivity. The flow variables at the boundary are fixed to the exact solution. The computational domain is chosen as a 4×2 rectangle. A sequence of successively refined meshes is used in this test. Figure 3.18 shows the coarsest triangle mesh.

Both BR2 and IP methods are tested for the accuracy. All the test cases presented below are obtained with an implicit Lower-Upper Symmetric Gauss Seidel (LU-SGS) time integration. In order to compare the accuracies of the scheme with different sets of solution

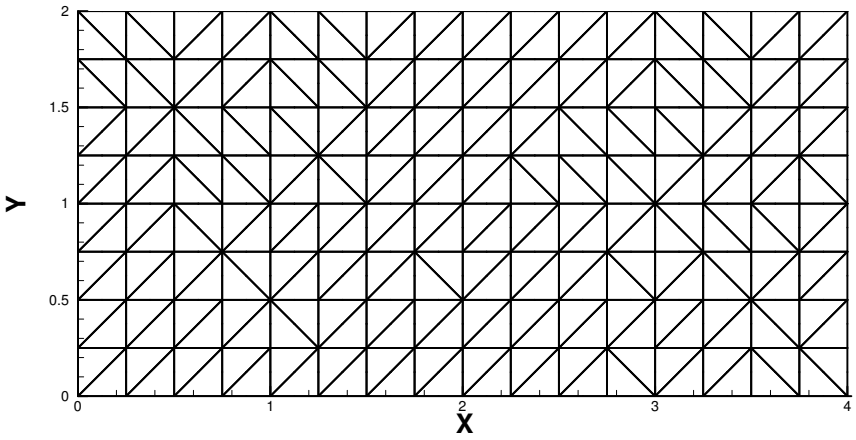

Figure 3.18: The coarsest triangular Mesh (8×16×2) for the 2D compressible Couette flow.

points, the $L2$ density errors defined as:

$$L_2(\Omega) = \left[\frac{\sum_{i=1}^{N} \int_{V_i} (\rho - \rho^{exact})^2 dV}{\sum_{i=1}^{N} |V_i|} \right] \tag{3.75}$$

are used for accuracy evaluation. In Eq. 3.75, the integral on each element is computed with a 33 points Gauss quadrature formula to make sure it is nearly independent of the quadrature rule. The h-refinement results for $P_N P_M - CPR$ with BR2 and IP schemes are shown Figure 3.19 respectively. The results show that the $P_N P_M - CPR$ with BR2 and IP is capable of achieving the optimum orders of accuracy $m + 1$ in almost all of the cases. Figure 3.19a indicates that BR2 performs a little bit better than IP. However, there is no significant difference between them either in the error magnitude or in the order of accuracy. Figure 3.19b shows the convergence of both the $P_N P_M - CPR$ and the classic CPR method with different solution points in the L2 norm. Here, only the BR2 results are shown. For the classic CPR method, the L2 errors with Lobatto and Gauss solution points are almost the same. However, it is not true for $P_N P_M - CPR$ methods. Due to the limited number of DOFs from its immediate neighbors, we lost some accuracy using P1P2-CPR with Lobatto points.

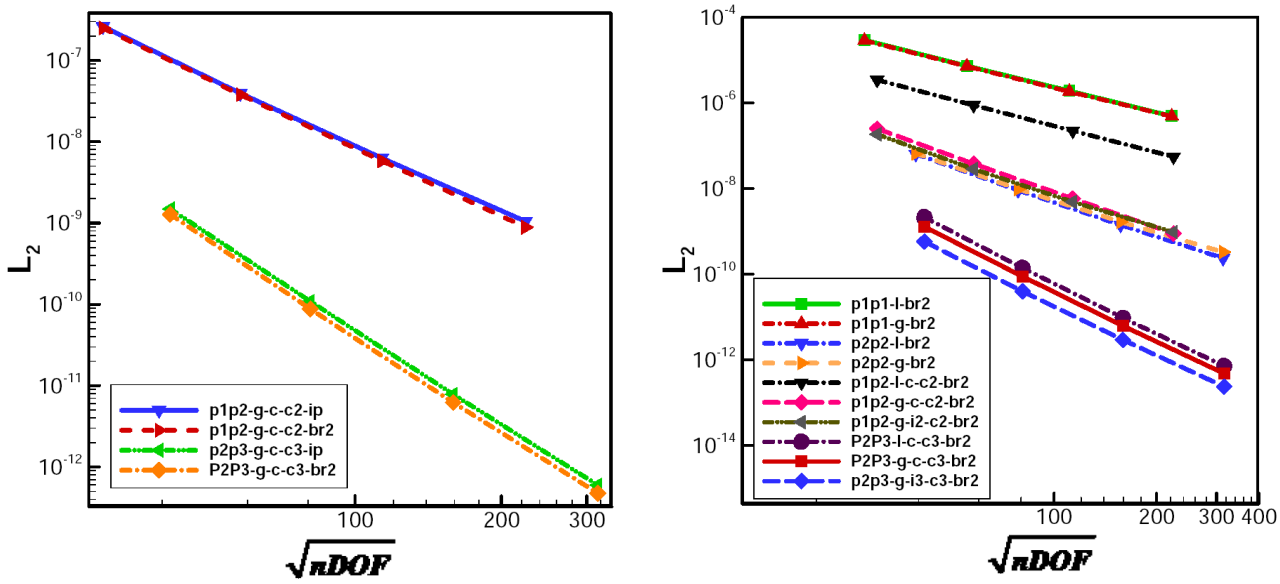

(a) $P_N P_M - CPR$ with IP and BR2 (b) $P_N P_M - CPR$/BR2 with different SPs

Figure 3.19: Density L2 error for the 2D compressible Couette flow.

3.5.4 Subsonic Viscous Flow Over a Circular Cylinder

Viscous flow over a circular cylinder is a classical benchmark case, which can represent general behavior of a bluff body flow. The flow past a cylinder becomes unstable around Reynolds number $Re = 40$. In this test, both steady and unsteady laminar flows around the cylinder are simulated using the $P_N P_M - CPR$ method with the BR2 approach. The inflow Mach number is set to be $Mach = 0.2$. Reynolds numbers which are based on the cylinder diameter are 20 and 75, respectively, for those two cases. Figure 3.20 shows the computational domain with 3964 triangle elements. It is an irregular unstructured mesh with refinements near the cylinder and in the wake region.

1. Steady Flow (Re=20)

   A symmetric steady separation bubble is expected to be formed in the wake of the cylinder at Reynolds number Re=20. The Mach number contours around the cylinder predicted with the $P_1P_2 - CPR$ and $P_2P_3 - CPR$ with a quadratic wall boundary rep-

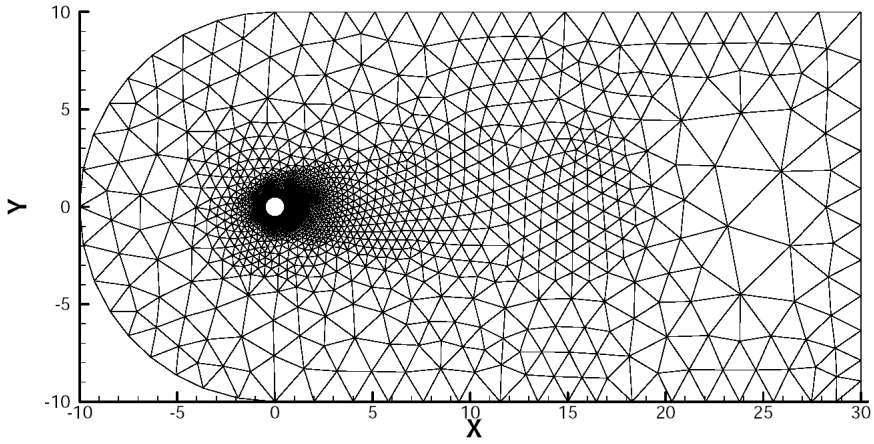

Figure 3.20: Triangle mesh for flow around a cylinder.

resentation are shown in Figure 3.21. Figure 3.22 presents the streamlines in the wake region. In both plots, steady separation bubbles are observed. The drag coefficient and the aspect ratio (the dimensionless separation bubble length, S/d) is shown in Table 3.1. The predicted drag coefficient is 2.171 from both of the schemes which is close to the value of 2.22 measured by Tritton[97]. The aspect ratio from both schemes agrees well with the experimental results of 0.935 obtained by Takami and Keller[95].

Table 3.1: Results for steady flow around a cylinder (Re=20, inflow Mach=0.2).

Schemes	C_D	S/d
P_1P_2-CPR	2.171	0.931
P_2P_3-CPR	2.171	0.932

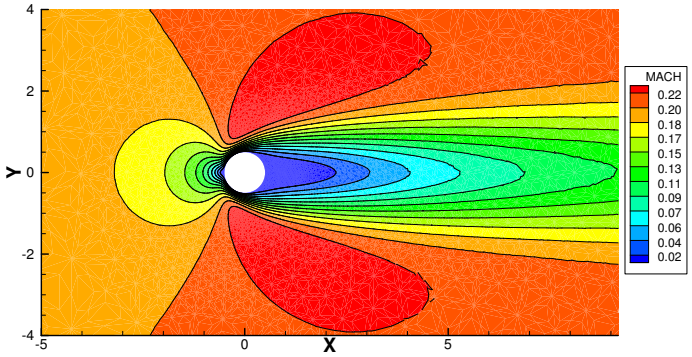

(a) P_1P_2-CPR

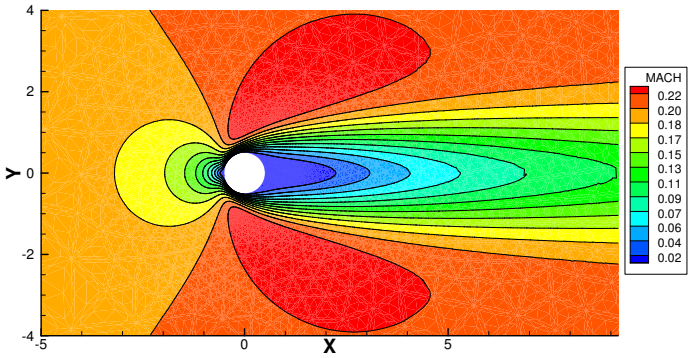

(b) P_2P_3-CPR

Figure 3.21: Mach number contours for flow over a cylinder at Re=20 and inflow Mach=0.2.

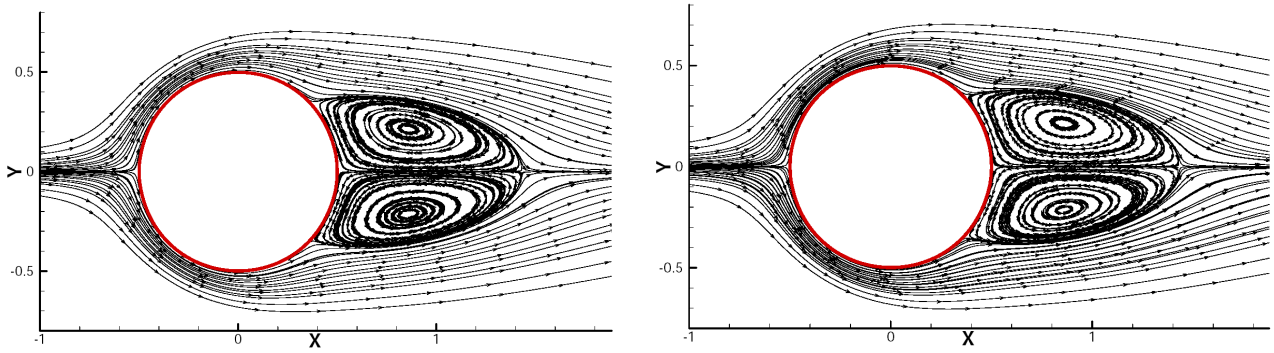

(a) P_1P_2-CPR (b) P_2P_3-CPR

Figure 3.22: Streamlines plots for flow over a cylinder at Re=20 and inflow Mach=0.2.

1. Unsteady Flow (Re=75)

A vortex street is expected to be formed in the wake of the cylinder at Reynolds number Re=75. The frequency of the vortex shedding can be denoted by the Strouhal number, defined by

$$St = \frac{f_s L_c}{U_\infty},$$

where the length scale L_c here is just the diameter of the cylinder.

Both $P_1P_2 - CPR$ and $P_2P_3 - CPR$ methods are tested to demonstrate the accuracy and robustness for unsteady laminar flows. A subsonic far field boundary condition is used at the outer boundary of the domain, and an adiabatic wall condition is used for the cylinder surface. A 2^{nd} order unsteady implicit LU-SGS solver is used for time integration. Piecewise quadratic polynomials are used to represent the curved cylinder boundary.

The converged flow filed at Re=20 from the previous section is used as the initial condition. The computed lift and drag coefficient on the cylinder versus non-dimensional time using $P_2P_3 - CPR$ are shown in Figure 3.23. The Von Kármán vortex street is fully developed after a time of 150. Figure 3.24 present instantaneous Mach number contours in one cycle of the vortex shedding using $P_2P_3 - CPR$.

Table 3.2 shows the average drag coefficient C_D and computed St for $P_1P_2 - CPR$ and $P_2P_3 - CPR$. They agree well with the experimental results by Williamson48, where St was found to be 0.148.

Table 3.2: Results for unsteady flow around a cylinder (Re=75, inflow Mach=0.2).

Schemes	$\overline{C_D}$	St
P_1P_2-CPR	1.417	0.151
P_2P_3-CPR	1.419	0.150

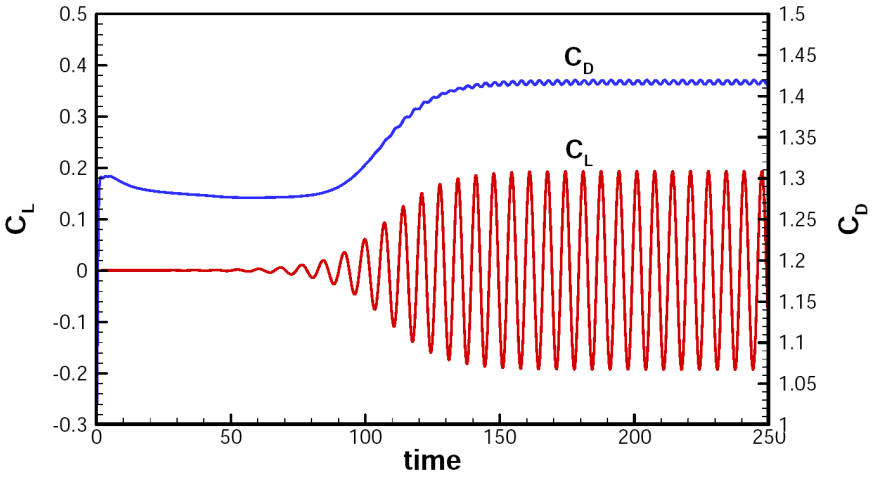

Figure 3.23: The lift and drag coefficients versus non-dimensional time for flow over a circular cylinder using $P_2P_3 - CPR$ (Re=75, inflow Mach=0.2).

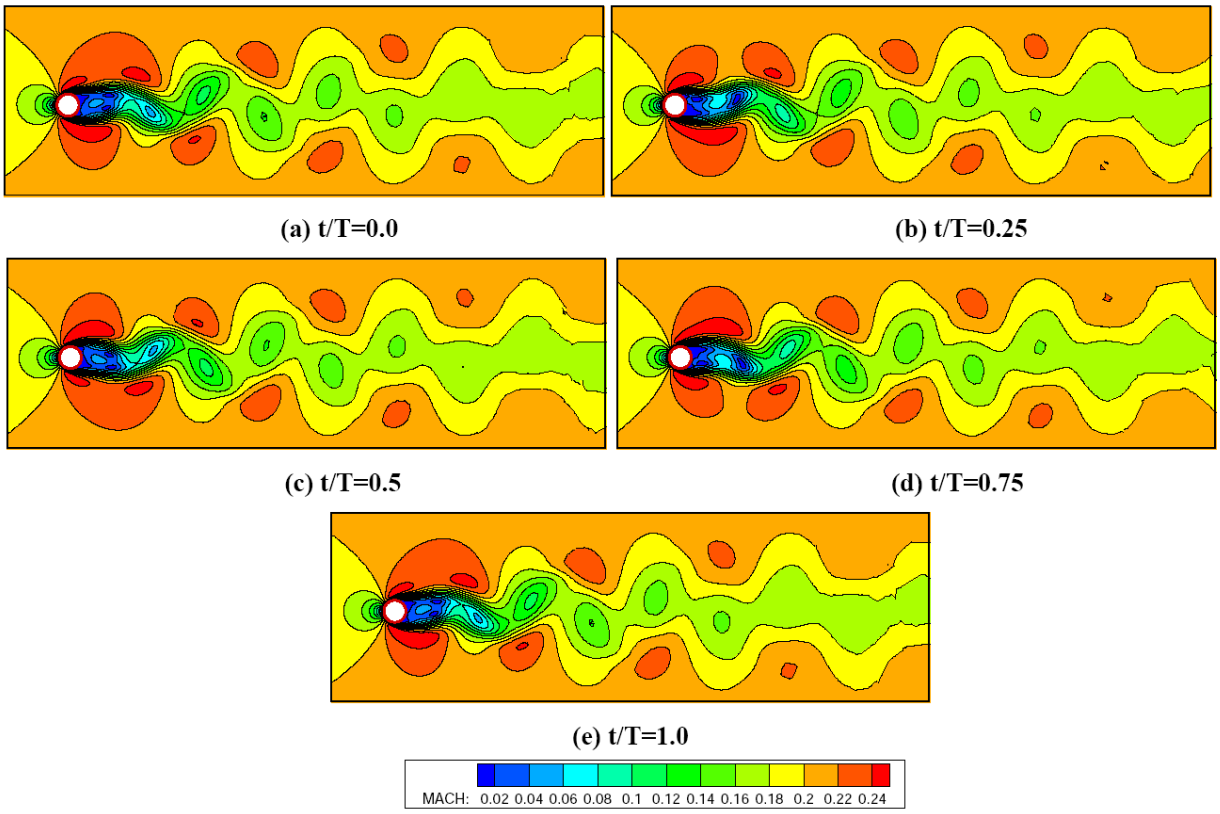

Figure 3.24: Mach number contours showing one cycle of vortex shedding from a circular cylinder using $P_2P_3 - CPR$ (Re=75, inflow Mach=0.2).

3.5.5 Laminar Flow Around a NACA0012 Airfoil

The laminar flow around a NACA 0012 airfoil is simulated by $P_N P_M - CPR$ method with the BR2 approach. $P_1P_1 - CPR$, $P_2P_2 - CPR$, $P_1P_2 - CPR$ and $P_2P_3 - CPR$ schemes are tested. The flow conditions are Mach = 0.5 and Re = 5000, with an angle of attack of 1 degree. Under such conditions, steady laminar separations are expected for both upper and lower surfaces of the airfoil.

Adiabatic no-slip wall condition is prescribed at the airfoil surface, which is represented by piecewise quadratic polynomials. The subsonic characteristic far field condition is used at the outer surface of the computational domain. The computational domain extends 50 chord lengths away from the center of the airfoil. The triangle mesh of 3584 cells is shown in Figure 3.25 with some refinement near the wall and at the trailing edge. An implicit LU-SGS solver is used for the time integration, and all cases converge to machine zero.

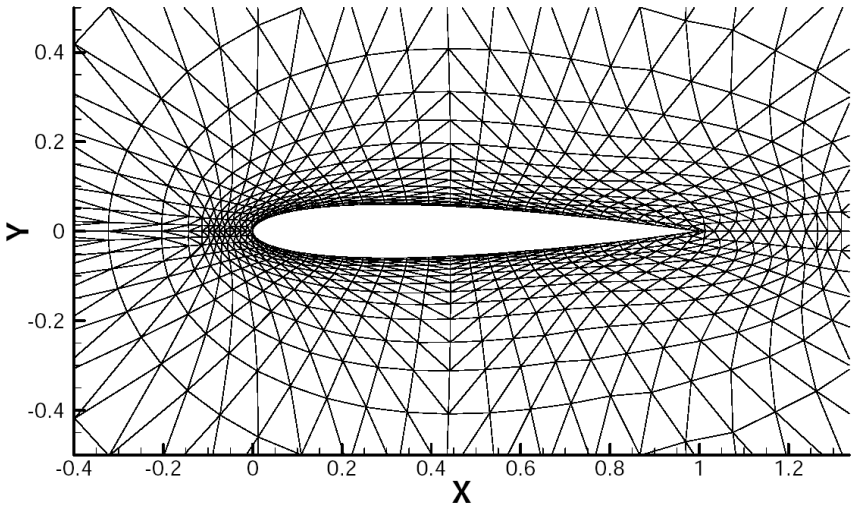

Figure 3.25: Computational mesh for subsonic laminar flow over the NACA0012 airfoil.

The computed Mach number contours of $P_1P_1 - CPR$, $P_2P_2 - CPR$, $P_1P_2 - CPR$ and $P_2P_3 - CPR$ method are shown in Figure 3.26. Only BR2 results are shown, since IP results

are similar. Due to the coarse mesh, results of $P_1P_1 - CPR$ and $P_1P_2 - CPR$ are not very smooth, especially at the wake region. Note that for $P_2P_2 - CPR$ and $P_2P_3 - CPR$, the contour lines are more smooth in the wake region. Visually, $P_2P_2 - CPR$ and $P_2P_3 - CPR$ results are very close to each other.

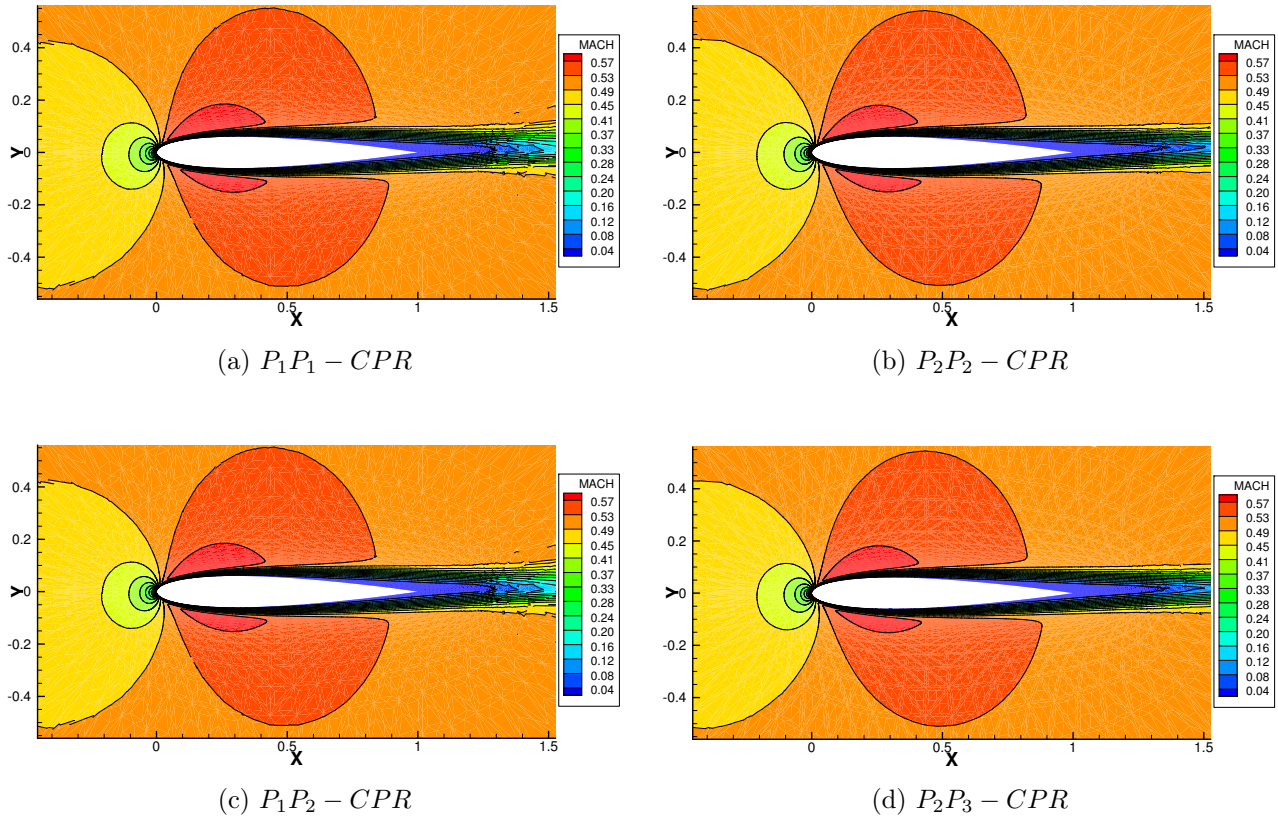

(a) $P_1P_1 - CPR$ (b) $P_2P_2 - CPR$

(c) $P_1P_2 - CPR$ (d) $P_2P_3 - CPR$

Figure 3.26: Mach number contours for flow around the NACA0012 airfoil (Inflow Mach=0.5, α=1^0, Re=5000).

The pressure coefficient C_p distribution and friction coefficient C_f distribution along the airfoil computed by all of the schemes are shown in Figure 3.27 and Figure 3.28. They are defined as

$$C_f = \frac{\tau_w}{\frac{1}{2}\rho U_\infty^2}, \; C_p = \frac{p}{\frac{1}{2}\rho U_\infty^2}, \; \tau_w = \mu \frac{\partial V}{\partial n}$$

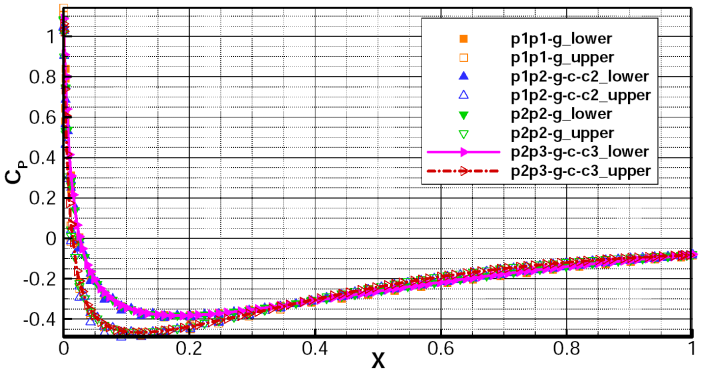

Figure 3.27: The pressure coefficient distributions along the NACA0012 airfoil (Mach=0.5, α=1^0, Re=5000).

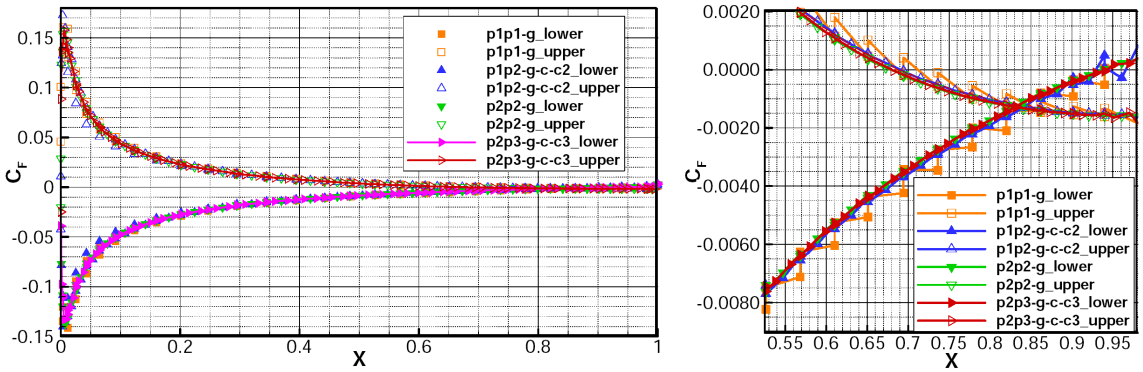

(a) C_f versus x coordinates

(b) Near the separation points

Figure 3.28: The skin coefficient distributions along the NACA0012 airfoil (Mach=0.5, α=1^0, Re=5000).

where the τ_w is the shear stress at wall. There is a close agreement in the computed C_f and C_f distribution especially for the solution with high-order polynomials. This demonstrates the accuracy of the $P_N P_M - CPR$ schemes.

3.5.6 Accuracy Study with 3D Vortex Propagation Problem

To assess the order of accuracy of the CPR method in 3D, the 2D vortex propagation problem in section 3.5.1 on page 51 is extended to the 3D domain $[0, 10] \times [0, 10] \times [0, 10]$. The accuracy

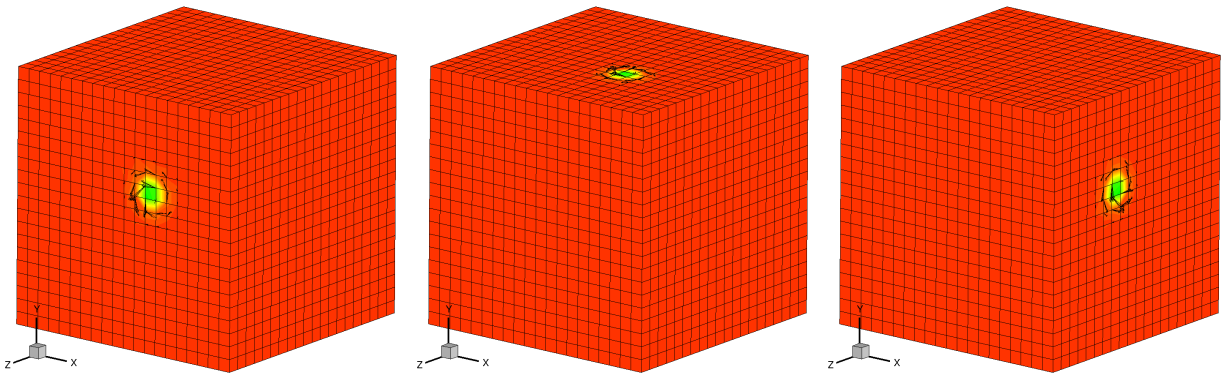

(a) XY (b) XZ (c) YZ

Figure 3.29: 3D vortex propagation in three different directions.

studies are performed on three different vortex transportation directions $(u, v, w) = (1, 1, 0)$, $(u, v, w) = (1, 0, 1)$ and $(u, v, w) = (0, 1, 1)$, as shown in Figure .

The 3^{rd} order Runge-Kutta explicit scheme is used for the time integration. The numerical simulation is carried out until $t = 1$. An set of uniformly refined hex mesh are employed. The CPR scheme with Gauss points as the SPs and FPs is used here. And the LP approach is employed for the flux divergence discretization. Figure 3.30 on the next page shows the L_2 density errors for $k = 1 \sim 5$. The optimal order of accuracy are obtained, and the errors remain the same when we change the propagation directions.

3.5.7 Accuracy Study with 3D Couette Flow Problem

To assess the accuracy of the CPR method for the viscous term in 3D, a laminar flow between two parallel walls is simulated on a cube of $[0, 10] \times [0, 10] \times [0, 10]$. This test case is a simple extension of the 2D problem in section 3.5.3 on page 53, therefore, the solution only changes in the y-direction. Figure 3.31 on page 66 shows the density on the coarsest mesh. The LU-SGS scheme is used for the time integration, and all of the cases are converged to the

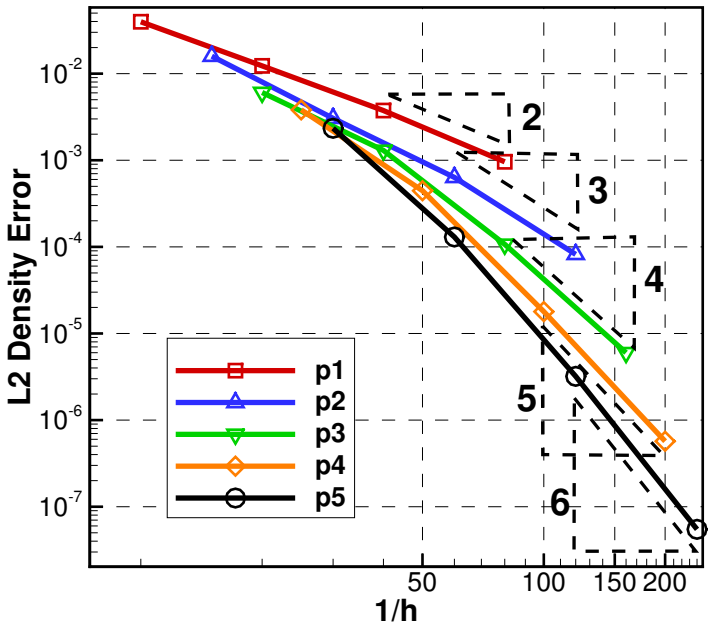

Figure 3.30: L_2 density errors for the CPR method with Gauss points as the SPs and FPs ($k = 1 \sim 5$).

machine zero. The CPR scheme with Gauss points as the SPs and FPs is used here. The exact solution is used to specify the flow variables at the boundary faces. Three successively refined hex grids with $N = 4$, 8, 16 are generated. Figure plots the density L_2 norm $p = 1-4$, which indicates the nearly optimal order of accuracy is achieved.

3.5.8 Direct Numerical Simulation of the Taylor-Green Vortex

A direct numerical simulation of a 3D transitional flow is carried out to test the DNS capabilities of the CPR method. The problem is the Taylor-Green vortex at $Re = 1600$. The flow is computed within a periodic square box defined as $-\pi L \leq x, y, z \leq \pi L$. The initial flow field is given by

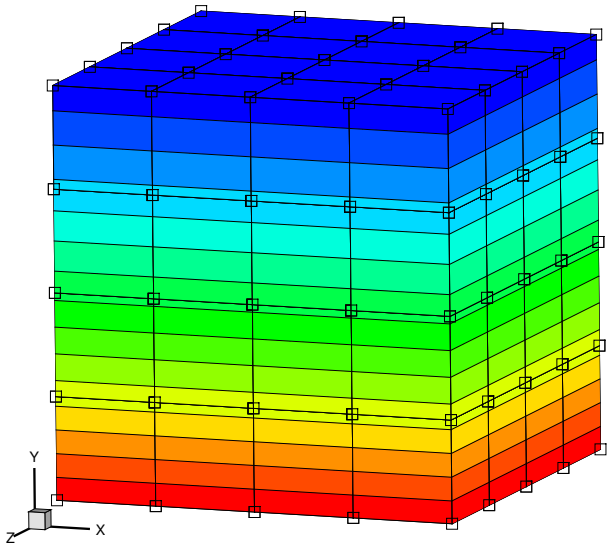

Figure 3.31: Density contours of the 3D couette flow problem on the coarsest mesh.

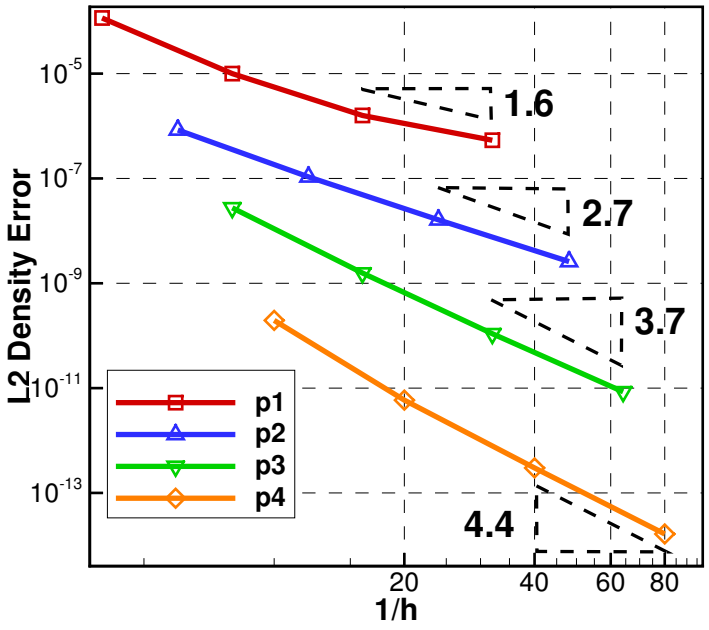

Figure 3.32: L_2 density errors for the CPR method with Gauss points as the SPs and FPs ($k = 1 \sim 5$).

$$
\begin{aligned}
u &= V_0 sin(\frac{x}{L}) cos(\frac{y}{L}) cos(\frac{z}{L}), \\
v &= -V_0 cos(\frac{x}{L}) sin(\frac{y}{L}) cos(\frac{z}{L}), \\
w &= 0 \\
p &= p_0 + \frac{\rho_0 V_0^2}{16} \left(cos(\frac{2x}{L}) + cos(\frac{2y}{L}) \right) \left(cos(\frac{2z}{L}) + 2 \right).
\end{aligned}
$$

Here, $M_0 = \frac{V_0}{c_0} = 0.1$, $T_0 = \frac{p_0}{R\rho_0}$ and L is the length of the cube. The Reynolds number of the flow is defined as $Re = \frac{\rho_0 V_0 L}{\mu} = 1600$, and the Prandtl number $Pr = \frac{\mu c_p}{k} = 0.71$ is used. The initial temperature and density field are set to be $T = T_0$ and $\rho = \frac{p}{RT_0}$ respectively. The initial solution only contains a single length scale L. However, it evolves into an isotropic, homogeneous turbulence rapidly due to the non-linear interactions of the newly generated eddies. Figure 3.33 shows the iso-surfaces of the Q-criteria magnitude colored by the z-component of the vorticity at different times using an 3^{rd} order CPR method.

A characteristic convection time can be defined as $t_c = \frac{L}{V_0}$. The computation are carried out until $t = 20t_c$. To reduce the computational time, the simulations are run in parallel with the domain decomposition. The explicit 3^{rd} order Runge-Kutta scheme is used for the time integration.

The CPR method with the Gauss points as the SPs and the LP approach for the flux divergence are tested for this problem. A p-refinement study of $k = 1$ to 3 is conducted on a 64^3 hex mesh. Figure 3.34 shows the temporal evolution of the kinetic energy integrated on the whole domain Ω defined as

$$
E_k = \frac{1}{\rho_0 \Omega} \int_\Omega \rho \frac{\vec{v}^2}{2} d\Omega.
$$

Figure 3.35 shows the results of the kinetic energy dissipation rate

$$\epsilon = -\frac{dE_k}{dt}$$

over the simulated time. The dissipation rates are computed by a one-sided finite differences method for each time step. For both of the kinetic energy and the dissipation rates, the results for the $k = 3$ CPR method are very close to the DNS results obtained using the pseudo-spectral method by van Rees et al. in [100].

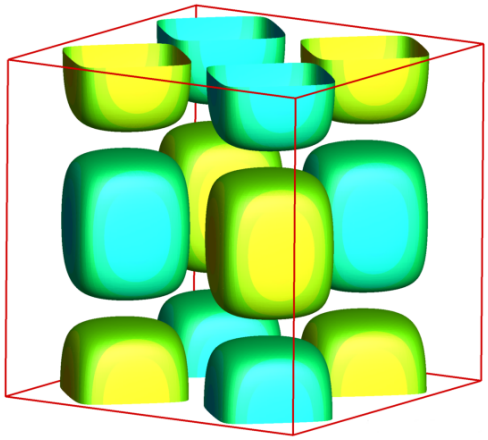

(a) time=0 sec

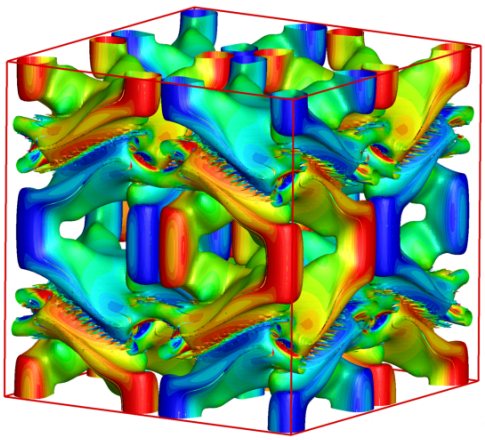

(b) time=15 sec

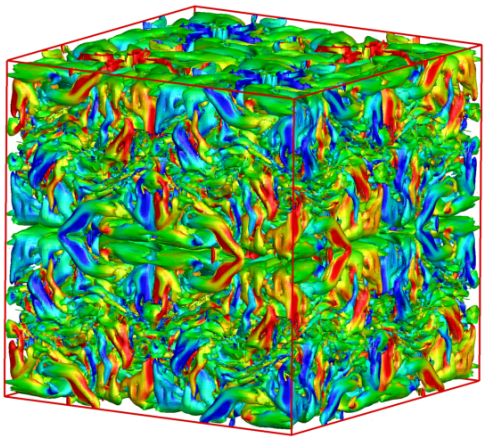

(c) time=60 sec

Figure 3.33: Iso-surfaces of the Q-criteria colored by the z-component of the vorticity for the Taylor-Green vortex at $Re = 1600$.

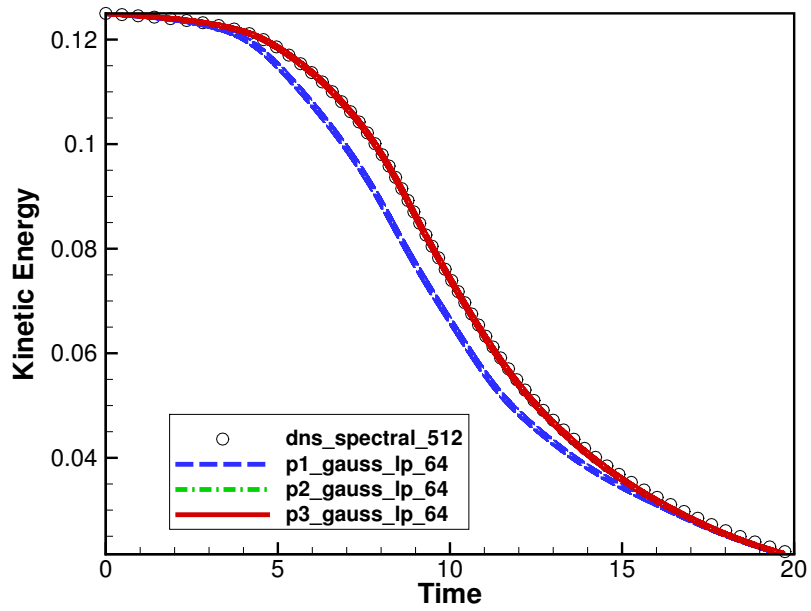

Figure 3.34: Evolution of the dimensionless kinetic energy as a function of the dimensionless time (DNS result is from [100]).

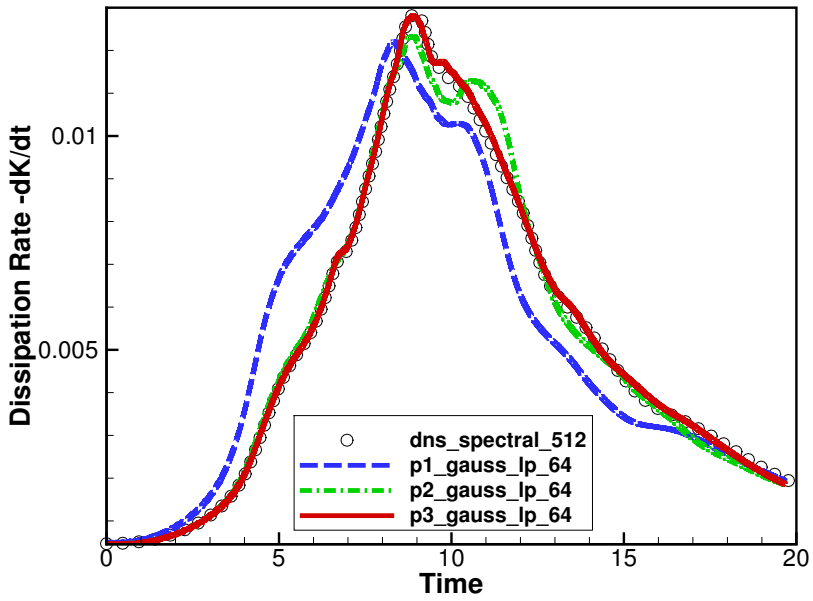

Figure 3.35: Evolution of the dimensionless kinetic energy dissipation rate as a function of the dimensionless time (DNS result is from [100]).

Chapter 4

The Dual-consistent CPR Formulation

Aircraft design engineers are usually interested in some scalar engineering design parameters, such as lift or drag coefficients, generated from CFD simulations. An adjoint solution can directly relate the local residual to the engineering output. Adjoints have been used in a wide range of applications including optimal controls, design optimization, data assimilation and error estimation. There are two approaches to obtain an adjoint solution. One can solve the continuous adjoint equation, which is a partial differential equation using any numerical method, or directly solve the discrete adjoint equation derived from the discretized primal equation. As for the primal problem, a numerical scheme is defined as a consistent method if its discrete operator converges to the continuous operator, or the exact solution satisfies the discrete numerical formulation as the mesh size approaches zero. Similarly, for a dual-consistent adjoint formulation, the exact adjoint solution from the continuous adjoint equation should satisfy the discrete adjoint equation in the limit of vanishing mesh size. The dual-consistency of a discrete adjoint operator from a numerical discretization is a key component to ensure that the optimal convergence rate is achieved for an engineering output. To establish a robust and accurate functional error estimation procedure for the CPR method, a dual-consistent CPR formulation is developed in this section.

4.1 The Dual Problem and Adjoint-based Error Estimation

4.1.1 Linear PDEs

First, we review the dual problem in the theory of output-based error estimation. A detailed discussion can be found in a series of articles [39, 40] and references therein. Consider a linear differential equation

$$LQ = f \quad \text{on}\,\Omega,$$

with a homogeneous boundary condition, where $Q \in V$ is the solution, V is the infinite dimensional solution space and $f \in L_2(\Omega)$. Suppose the output functional of interest $\mathcal{J}$ is given as an inner product of a smooth function g and the solution Q

$$\mathcal{J}(Q) = (g, Q) \equiv \int_\Omega gQdV,$$

over the entire domain Ω. The dual problem is introduced by adding a weighted residual to the functional

$$\mathcal{J}(Q) = (g, Q) + (\psi, f - LQ).$$

where ψ is an arbitrary function for now. If the solution Q satisfies the linear differential equation, this weighted residual does not affect the value of the original functional. Denote L^* the adjoint differential operator with respect to L defined according to $(\psi, LQ) = (L^*\psi, Q)$ with homogeneous boundary conditions. Then we have

$$\mathcal{J}(Q) = (g, Q) + (\psi, f) - (\psi, LQ) = (g, Q) + (\psi, f) - (L^*\psi, Q) = (\psi, f) - (L^*\psi - g, Q). \quad (4.1)$$

Let ψ be the adjoint solution computed using

$$L^*\psi = g \quad \text{on}\,\Omega.$$

Then the last term in Eq. 4.1 vanishes, and we obtain

$$\mathcal{J}(Q) = (\psi, f).$$

Obviously, J is independent of Q, but depends on ψ now. So we call J a function of ψ, i.e.,

$$\mathcal{J}(\psi) = (\psi, f) - (L^*\psi - g, Q). \tag{4.2}$$

Therefore, the duality of the functional is

$$\mathcal{J}(Q) = (g, Q) \quad if \quad LQ = f \quad \text{on}\,\Omega$$

or

$$\mathcal{J}(\psi) = (\psi, f) \quad if \quad L^*\psi = g \quad \text{on}\,\Omega.$$

Suppose Q_h and ψ_h are the discrete primal solution and the discrete adjoint solution obtained with a numerical method, and both of them belong to the discrete solution space V_h. Then, the discrete source term for the primal equation is $f_h = LQ_h$. The functional error can be estimated by

$$\begin{aligned}\delta\mathcal{J} = (g, Q_h) - (g, Q) &= (g, Q_h - Q) \\ &= (L^*\psi, Q_h - Q) \\ &= (\psi, L(Q_h - Q)) \\ &= \underbrace{(\psi_h, f_h - f)}_{computable\,error} + \underbrace{(\psi - \psi_h, f_h - f)}_{remaining\,error}, \end{aligned} \tag{4.3}$$

where the linearity of the inner product and the adjoint definition are used. Note that the first term on the RHS of Eq. 4.3 is defined as the computable error, since it does not involve any analytical primal solution. If a numerical method possesses the Galerkin orthogonality property,

$$(v_h, f_h - f) = 0, \quad \text{for all } v_h \in V_h,$$

the computable error vanishes since we take ψ_h in space V_h. Therefore, there is no need to evaluate the computable error, and the order of the output error only depends on the remaining error term. If we use a degree k polynomial to approximate the primal and adjoint solution and assume the optimal order of accuracy can be achieved, we obtain

$$\|Q_h - Q\| = O(h^{k+1}), \quad \|\psi_h - \psi\| = O(h^{k+1}).$$

Here$\|.\|$ is a L_2 norm. In addition, for an n^{th} order differential PDE, we have $\|f_h - f\| = O(h^{k+1-n})$. So the order of the computable error is $O(h^{2k+2-n})$, which leads to a superconvergent functional of order $O(h^{2k+2-n})$. To estimate the output error, we need to evaluate the computable error. A common approach is to use an adjoint solution from a finer approximation space, e.g. $p = k + 1$. Then the computable error is not equal to 0, and we can use this error estimate to correct the original output

$$\mathcal{J}_{corr} \equiv \mathcal{J}(Q_h) + (\psi_h, f_h - f).$$

The convergence rate of this corrected output is two orders higher than the original output, which is $O(h^{2k+4-n})$. A rigorous proof can be found in Ref. [48].

4.1.2 Nonlinear PDEs

Consider a non-linear differential equation

$$\mathcal{N}(Q) = 0, \quad \text{on}\,\Omega. \tag{4.4}$$

Suppose an output functional of interest is given as $\mathcal{J}(Q)$. A dual problem is introduced by defining a Lagrangian of the output with the constraint of the solution Q satisfying the primal equation $\mathcal{N}(Q) = 0$

$$\mathcal{L} = \mathcal{J}(Q) + \int_\Omega \psi \mathcal{N}(Q) \mathrm{d}\Omega. \tag{4.5}$$

Here $\psi \in V$ has two roles. First, ψ is the adjoint solution. Second, it also serves as a Lagrange multiplier. After performing the linearization and enforcing stationary of $\mathcal{L}$ to a solution perturbation $\delta Q \in V$, we obtain

$$\delta\mathcal{L} = \mathcal{L}'[Q](\delta Q) = \mathcal{J}'[Q](\delta Q) + \int_\Omega \psi \mathcal{N}'[Q](\delta Q) \mathrm{d}\Omega = 0 \quad \forall \delta Q \in V, \tag{4.6}$$

where the primed notation denotes Frechét linearization with respect to an argument in the square bracket. Eq. 4.6 defines the dual problem in a variational form by finding ψ such that

$$\mathcal{J}'[Q](v) + \int_\Omega \psi \mathcal{N}'[Q](v) \mathrm{d}\Omega = 0 \quad \forall v \in V. \tag{4.7}$$

Let Q_h denote an approximate solution to the analytical solution Q. The difference

between them can be interpreted as a solution perturbation $Q_h = Q + \delta Q$. The output error defined as $\delta\mathcal{J} = \mathcal{J}(Q_h) - \mathcal{J}(Q)$ can be estimated by the adjoint weighted residual method

$$\delta\mathcal{J} \approx \mathcal{J}'[Q](\delta Q) = -\int_\Omega \psi\mathcal{N}'[Q](\delta Q)\mathrm{d}\Omega \approx -\int_\Omega \psi(\mathcal{N}(Q_h) - \mathcal{N}(\mathrm{Q}))\mathrm{d}\Omega = -\int_\Omega \psi\mathcal{N}(Q_h)\mathrm{d}\Omega. \tag{4.8}$$

4.2 The Continuous Adjoint Equation

We consider the following conservation law

$$\mathcal{N}(Q) \equiv \nabla \cdot \vec{\mathcal{F}}(Q), \tag{4.9}$$

as an example to develop the continuous adjoint equation. Eq. 4.7 leads to

$$\mathcal{J}'[Q](v) + \int_\Omega \psi \left(\frac{\partial}{\partial Q} \left(\nabla \cdot \vec{\mathcal{F}} \right) \right) (v)\mathrm{d}\Omega = 0 \quad \forall v \in V. \tag{4.10}$$

Suppose the output functional $\mathcal{J}(Q)$ consists of surface ($\partial\Omega$) and volume (Ω) integrals

$$\mathcal{J}(Q) = \int_\Omega gQ\mathrm{d}\Omega + \int_{\partial\Omega} j_\tau(Q)\mathrm{d}s,$$

where j_τ is a boundary operator. Substituting the definition of $\mathcal{J}$ into Eq. 4.10, and performing integration by parts, we get

$$\int_\Omega (g - \nabla\psi \cdot \frac{\partial\vec{\mathcal{F}}}{\partial Q})\mathrm{d}\Omega + \int_{\partial\Omega} (\frac{\partial j_\tau}{\partial Q} + \psi\frac{\partial\vec{\mathcal{F}}}{\partial Q} \cdot \vec{n})\mathrm{d}s = 0.$$

The above equation yields the governing equation for the continuous adjoint

$$\nabla\psi \cdot \frac{\partial\vec{\mathcal{F}}}{\partial Q} = g, \tag{4.11}$$

which is a linear partial differential equation for ψ, and the corresponding boundary conditions are from the surface integral

$$\int_{\partial\Omega}(\frac{\partial j_\tau}{\partial Q}+\psi\frac{\partial\vec{\mathcal{F}}}{\partial Q}\cdot\vec{n})\mathrm{d}s=0. \tag{4.12}$$

4.3 The Dual-Consistent CPR Formulation

The discrete adjoint equation is obtained directly by linearizing the discretized primal equation. Consider a discretized formulation of the primal Eq. 4.4

$$\mathcal{N}_h(Q_h)=0,\quad Q_h\in V_h$$

with mesh h, and a discrete solution perturbation $\delta Q_h\in V_h$. Linearizing the discrete residual $\mathcal{R}_h\equiv-\mathcal{N}_h(Q_h)$ and the discrete output $\mathcal{J}_h$, we get

$$\delta\mathcal{R}_h=\mathcal{R}_h(Q_h+\delta Q_h)-\mathcal{R}_h(Q_h)\approx\frac{\partial\mathcal{R}_h}{\partial Q_h}\delta Q_h$$

$$\delta\mathcal{J}_h=\mathcal{J}_h(Q_h+\delta Q_h)-\mathcal{J}_h(Q_h)\approx\frac{\partial\mathcal{J}_h}{\partial Q_h}\delta Q_h.$$

The discrete adjoint $\tilde{\psi}_h$ is defined as the sensitivity of output perturbation $\delta\mathcal{J}_h$ to the primal residual perturbation $\delta\mathcal{R}_h$

$$\delta\mathcal{J}_h\equiv-\tilde{\psi}_h^T\delta\mathcal{R}_h,$$

which leads to

$$\frac{\partial\mathcal{J}_h}{\partial Q_h}\delta Q_h\approx\delta\mathcal{J}_h=-\tilde{\psi}_h^T\delta\mathcal{R}_h\approx-\tilde{\psi}_h^T\frac{\partial\mathcal{R}_h}{\partial Q_h}\delta Q_h.$$

We obtain the discrete adjoint equation by canceling the solution perturbation δQ_h

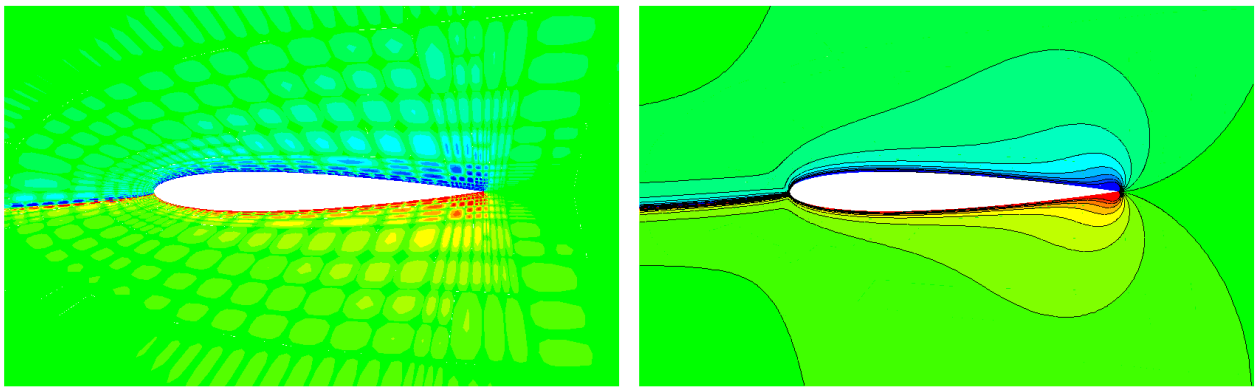

(a) The discrete adjoint (b) The discrete adjoint in variational forms

Figure 4.1: The C_L adjoint for a subsonic NACA0012 airfoil.

$$-\frac{\partial \mathcal{R}_h}{\partial Q_h}^T \tilde{\psi}_h = \frac{\partial \mathcal{J}_h}{\partial Q_h}^T. \tag{4.13}$$

For numerical methods with a weak form, e.g. FEM or DG methods, after choosing a proper basis, Eq. 4.13 is equivalent to its variational formulation. A detailed derivation can be found in Ref. [32, 44]. So the discrete adjoint equation for numerical methods in semi-linear form is consistent with the continuous adjoint equation. However, this is not true for numerical methods in a differential form, such as the CPR method, which does not possess a variational form.

Substituting a pointwise residual $r_{i,j}$ defined on each solution point j of cell i arising from a differential scheme, we obtain

$$-\sum_i \sum_j \frac{\partial r_{i,j}}{\partial Q_l} \tilde{\psi}_{i,j} = \frac{\partial \mathcal{J}}{\partial Q_l}, \tag{4.14}$$

where l is the global index of the DOFs in the entire domain. Figure 4.1a shows the x-momentum component of the lift adjoint for a subsonic airfoil using the discrete adjoint equation with the CPR method. It has a very oscillatory distribution in each cell, which indicates dual-consistency violations.

Since the CPR method is not in a variational form, its discrete adjoint equation should

be directly derived from the linearized Lagrangian. Assume the adjoint solution belongs to the same space of the primal solution, the adjoint variable ψ_i of cell i can be approximated using the Lagrange basis L_j

$$\psi_i = \sum_j L_j \hat{\psi}_{i,j}.$$

Directly discretizing the linearized Lagrangian, Eq. 4.7, with a quadrature rule, we obtain

$$-\sum_i \sum_j \frac{\partial r_{i,j}}{\partial Q_l} \omega_j |J_{i,j}| \hat{\psi}_{i,j} = \frac{\partial \mathcal{J}}{\partial Q_l}, \tag{4.15}$$

where ω_j and $|J_{i,j}|$ are the quadrature weight and the element Jacobian at the solution point. Comparing with Eq. 4.14, the following relation can be derived from the discrete adjoint $\tilde{\psi}_{i,j}$ and the discrete adjoint $\hat{\psi}_{i,j}$ in the integral form

$$\tilde{\psi}_{i,j} = \omega_j |J_{i,j}| \hat{\psi}_{i,j}.$$

It is obvious that the discrete adjoint formula for a numerical scheme in a differential form is not consistent with the continuous adjoint equation. The inconsistent adjoint is related to the consistent counterpart in terms of the quadrature weight ω and the cell Jacobian $|J|$. This integral equation can be interpreted as an explicitly defined variational form for the CPR method. In this paper, we call it dual-consistent discrete adjoint formula. Figure 4.1b shows the consistent discrete adjoint solution with the CPR method. Clearly the consistent adjoint solution is smooth.

4.4 Analysis of Dual-Consistency for the CPR Method

For a dual-consistent discretization, the discrete adjoint solution should approach the continuous adjoint solution when the mesh size diminishes. In other words, the analytic primal solution Q and the analytic dual solution ψ should satisfy the discrete adjoint equation when

the mesh size goes to zero. Substituting the discrete residual of the CPR method into the discrete adjoint equation for the conservation law leads to

$$\sum_i \sum_j \frac{\partial}{\partial Q_l} \left(\nabla \cdot \vec{F}(Q)_{i,j} + \delta_{i,j} \right) \omega_j |J_{i,j}| \hat{\psi}_{i,j} = -\frac{\partial \mathcal{J}}{\partial Q_l}, \tag{4.16}$$

where $\delta_{i,j}$ is the correction term. For a 1D CPR formulation, the above equation can be further expressed as

$$\sum_i \sum_j \left(\sum_k \frac{\partial F_{i,k}}{\partial Q_l} \frac{dL_k(\xi_j)}{d\xi} + \frac{\partial}{\partial Q_l} [F]_{i-\frac{1}{2}} g'_L(\xi_j) + \frac{\partial}{\partial Q_l} [F]_{i+\frac{1}{2}} g'_R(\xi_j) \right) \omega_j \xi_{x,i,j} \hat{\psi}_{i,j} = -\frac{\partial \mathcal{J}}{\partial Q_l}. \tag{4.17}$$

Here, g'_L, g'_R and ψ_i belong to $P^k(\Omega_i)$. $\frac{dL}{d\xi}$ is a degree $k-1$ polynomial. Therefore, the degree of the integrand is at least $2k$. Assume that the quadrature rule defined on the solution points is exact at least for a degree $2k$ polynomial. Then we have

$$\sum_i \int_{\Omega_i} \psi_i \sum_k \frac{\partial F_{i,k}}{\partial Q_l} \frac{dL_k}{d\xi} \xi_x \mathrm{d}x + \sum_i \int_{\Omega_i} \psi_i \left(\frac{\partial}{\partial Q_l} [F]_{i-\frac{1}{2}} g'_L + \frac{\partial}{\partial Q_l} [F]_{i+\frac{1}{2}} g'_R \right) \xi_{\mathrm{x}} \mathrm{d}x = -\frac{\partial \mathcal{J}}{\partial Q_l}.$$

Performing integration by parts on the LHS, we obtain

$$\begin{aligned} LHS = &- \sum_i \int_{\Omega_i} \frac{\partial F}{\partial Q} \frac{d\psi}{dx} \mathrm{d}x + \sum_i \psi \frac{\partial \mathcal{F}}{\partial Q} |_{i-\frac{1}{2}}^{i+\frac{1}{2}} \\ &+ \sum_i \frac{\partial [F]_{i-\frac{1}{2}}}{\partial Q} \left(\psi_i g_L |_{-1}^1 - \int_{-1}^1 \psi'_i \mathrm{g_L} \mathrm{d}\xi \right) + \sum_i \frac{\partial [F]_{i+\frac{1}{2}}}{\partial Q} \left(\psi_i g_R |_{-1}^1 - \int_{-1}^1 \psi'_i \mathrm{g_R} \mathrm{d}\xi \right). \end{aligned} \tag{4.18}$$

Recall that, for the CPR method, the correction functions satisfy

$$g_L(-1) = g_R(1) = 1$$

$$g_L(1) = g_R(-1) = 0.$$

Furthermore, a DG correction function g_{DG} of degree $k+1$ is orthogonal to P^{k-1}, i.e.,

$$\int_{-1}^{1} g_{DG}(\xi)\phi(\xi)\mathrm{d}\xi = 0, \quad ,\forall\phi \in P^{k-1}.$$

Therefore, if a DG correction function is used, Eq. 4.18 can be simplified to

$$LHS = -\sum_i \int_{\Omega_i} \frac{\partial F}{\partial Q}\frac{d\psi}{dx}\mathrm{d}x + \sum_i \psi\frac{\partial \mathcal{F}}{\partial Q}|_{i-\frac{1}{2}}^{i+\frac{1}{2}} - \sum_i \frac{\partial [F]_{i-\frac{1}{2}}}{\partial Q}\psi_{i-\frac{1}{2}} + \sum_i \frac{\partial [F]_{i+\frac{1}{2}}}{\partial Q}\psi_{i+\frac{1}{2}}, \quad (4.19)$$

or equivalently,

$$LHS = -\sum_i \int_{\Omega_i} \frac{\partial F}{\partial Q}\frac{d\psi}{dx}\mathrm{d}x + \sum_i \frac{\partial F^{com}_{i+\frac{1}{2}}}{\partial Q}\psi_{i+\frac{1}{2}} - \sum_i \frac{\partial F^{com}_{i-\frac{1}{2}}}{\partial Q}\psi_{i-\frac{1}{2}}. \quad (4.20)$$

The first term is the governing equation for the continuous adjoint equation, which vanishes for the analytic adjoint solution. Notice that

$$\begin{aligned}\sum_i \frac{\partial F^{com}_{i+\frac{1}{2}}}{\partial Q}\psi_{i+\frac{1}{2}} - \sum_i \frac{\partial F^{com}_{i-\frac{1}{2}}}{\partial Q}\psi_{i-\frac{1}{2}} &= \frac{\partial F^{com}_{N+\frac{1}{2}}}{\partial Q}\psi_{N+\frac{1}{2}} - \frac{\partial F^{com}_{\frac{1}{2}}}{\partial Q}\psi_{\frac{1}{2}} + \sum_{i=1}^{N-1}(\psi_i(1) - \psi_{i+1}(-1))\frac{\partial F^{com}_{i+\frac{1}{2}}}{\partial Q} \\ &= \frac{\partial F^{com}_{N+\frac{1}{2}}}{\partial Q}\psi_{N+\frac{1}{2}} - \frac{\partial F^{com}_{\frac{1}{2}}}{\partial Q}\psi_{\frac{1}{2}}\end{aligned}$$

when $\psi_i(1) = \psi_{i+1}(-1)$ for the analytical adjoint solution. So the final equation is

$$\frac{\partial F^{com}_{N+\frac{1}{2}}}{\partial Q}\psi_{N+\frac{1}{2}} - \frac{\partial F^{com}_{\frac{1}{2}}}{\partial Q}\psi_{\frac{1}{2}} = -\frac{\partial \mathcal{J}}{\partial Q}. \quad (4.21)$$

As discussed in Ref. [44, 74], a well-defined dual-consistent boundary flux should only be a function of the boundary state $F^{com} = F^{com}(Q_{bc}(Q_L))$, and a properly-defined dual-consistent output functional leads to Eq. 4.21 and is consistent with the dual boundary condition for the continuous adjoint equation (Eq. 4.12). Therefore, Eq. 4.16 can be satisfied exactly with an analytical adjoint solution. A similar procedure can be applied to the system of equations in 2D. The corresponding equation to Eq. 4.21 is

$$\int_{\Gamma} \psi^T \frac{\partial F^{com}}{\partial Q} \mathrm{d}s = \frac{\partial \mathcal{J}}{\partial Q}, \tag{4.22}$$

which will be used to analyze the dual consistency for the 2D linear wave equation and the Euler equations in the next section.

Based on the analysis, the key factors to ensure a dual-consistent CPR formulation are summarized next.

1. In order to ensure the integral accuracy of the discrete adjoint equation in a variational form, an accurate quadrature rule defined on the solution points should be exact for a degree $2k$ polynomial. Recall that a k+1 point Gaussian quadrature rule can yield an exact integration of a degree $2k+1$ polynomial. Therefore, the Gauss quadrature points are preferred as the solution points. The Lobatto quadrature rule can only integrate a degree $2k-1$ polynomial exactly. If the Lobatto points are used as the solution points, the CPR formulation will have an accuracy loss for the discrete adjoint solution and the corresponding error estimation.

2. The correction function g in the CPR method must be orthogonal to the derivatives of the adjoint solution

$$\int_{\Omega} g\psi' \mathrm{d}\Omega = 0. \tag{4.23}$$

If we assume that the discrete adjoint ψ belongs to the same space of the primal

solution, the degree of the derivative ψ' is $k-1$. Then the only qualified correction function is the DG correction function g_{DG}, which is orthogonal to P^{k-1}. On the other hand, the degree of the adjoint solution ψ is determined by the specific correction function. Suppose we use the g_2 correction function, which is only orthogonal to P^{k-2}. To satisfy this condition, the degree of the discrete adjoint solution ψ is automatically degenerated to $k-1$. In summary, for a CPR scheme with a correction function g_m, the discrete adjoint $\psi \in P^{k+1-m}$.

3. The Lagrange polynomial (LP) approach is required to evaluate the flux divergence term in the CPR formulation, instead of the chain rule (CR) approach. This requirement is very similar to the conservation requirements for the CPR scheme. Therefore, a similar fix can be obtained by following the conservation fix of the CR approach [35]. However, the numerical results in the next section show that the dual-inconsistent violation by the CR approach is relatively weak.

4. A properly defined common numerical flux on the boundaries, and a well-defined output functional, are critical in making the boundary terms in the adjoint equation vanish.

4.5 Numerical Tests

4.5.1 Linear Advection Equation

First, the dual-consistent CPR discretization and the error estimation are verified with a first-order hyperbolic partial differential equation (PDE). Consider a 2D linear wave equation

$$\nabla \cdot \vec{c}Q = f, \quad x \in \Omega$$

with a Dirichlet boundary condition

$$Q(\vec{x}) = B(\vec{x}), \quad x \in \partial\Omega^{-}$$

given on the inflow boundaries $\partial\Omega^- = \{\vec{x} \in \partial\Omega |\ \vec{n} \cdot \vec{c} < 0\}$, where $\vec{n}$ is the outward surface normal direction and $\vec{c}$ is the advection velocity (Figure 4.2a) prescribed as

$$\vec{c} = (e^{-x}, e^{y}).$$

The solution is set to be

$$Q(\vec{x}) = e^{y}\sin(\frac{\pi(e^{x}-1)}{e-1}),$$

which determines the source term f by the method of manufactured solutions [47].

The simulation is performed on a unit square $\Omega = [0,1]^2$ filled with quadrilateral elements. The output of interest is defined on the outflow boundaries $\partial\Omega^+ = \{\vec{x} \in \partial\Omega |\ \vec{n} \cdot \vec{c} > 0\}$ as

$$\mathcal{J}(Q) = \int_{\partial\Omega^+} g(\vec{x})(\vec{n} \cdot \vec{c}Q)ds,$$

where the weighting function

$$g(\vec{x}) = \frac{\pi e^{x-y}}{e-1}.$$

The exact value of the output is $\mathcal{J} = 2e$.

In this case, Eq. 4.22 leads to

$$\int_{\partial\Omega^+} \psi \frac{\partial F^{com}}{\partial Q} ds = -\frac{\partial}{\partial Q} \int_{\partial\Omega^+} g(\vec{x})(\vec{n} \cdot \vec{c}Q)ds,$$

which is equivalent to the boundary condition for the continuous adjoint equation

$$\int_{\partial\Omega^+} (\vec{n} \cdot \vec{c})\, \psi + (\vec{n} \cdot \vec{c}) g(\vec{x}) ds = 0.$$

The common flux $F^{com}(Q_{BC}(Q_L), \vec{n}) = \vec{n} \cdot \vec{c}Q_L$ is chosen for the boundaries to ensure that the CPR method for the linear wave equation with this output is a dual-consistent formulation.

The contours of the primal solution and the adjoint solution are shown in Figure 4.2.

Based on the dual-consistency analysis, we choose the Gauss points as the solution points and the DG correction function g_{DG}. Figure 4.3 shows the convergence rate of the primal solution, the output functional and the error estimate using the CPR method. The optimal order $O(h^{k+1})$ is obtained for the primal solution. Super convergence of the output functional and the error estimate is good indicator of a dual-consistent discretization. For this case, a super convergence of $O(h^{2k+1})$ is observed for both of the output error and the adjoint-based output error estimate. The corrected output converges 2 orders faster than the original output, which is $O(h^{2k+3})$. The results of the CPR method with Lobatto points and g_{dg} is shown in Figure 4.4a. Comparing with the results of the Gauss points, the accuracy loss of the quadrature rules defined on the Lobatto points leads to one order loss in the output functional, the error estimate and the corrected functional.

Now we test the influence of the correction functions on the output functional and the error estimate. As discussed in [51], for an integral $m \geq 1$, a correction function g_m of degree $k+1$ is orthogonal to P^{k-m}, and the Fourier analysis indicates that the order of the corresponding scheme is $O(h^{2k+2-m})$. The previous analysis shows that the approximation order of the adjoint solution ψ is determined by the correction function g_m as $O(h^{k+1-m})$.

Figure 4.4 shows the convergence rates using the g_2 and g_3 correction functions with the Gauss points as the solution points. Similar relationships are obtained between the order of accuracy of the functional outputs, the error estimate and the correction functions. For the advection equation, the output functional and the adjoint-based error estimate with the Gauss points and g_m are accurate to order $O(h^{2k+2-m})$. Furthermore, the corrected outputs of the corresponding schemes are accurate to order $O(h^{2k+4-m})$. The convergence rates with the different CPR schemes are summarized in Table 4.1. Those results are consistent with the analysis in section 4.3.

For a linear partial differential equation, the discrete adjoint based output error estimation should recover the exact output error obtained by a finite difference method. Table 4.2 compare the true output error between k = 1 and k = 2 results and the adjoint-based output

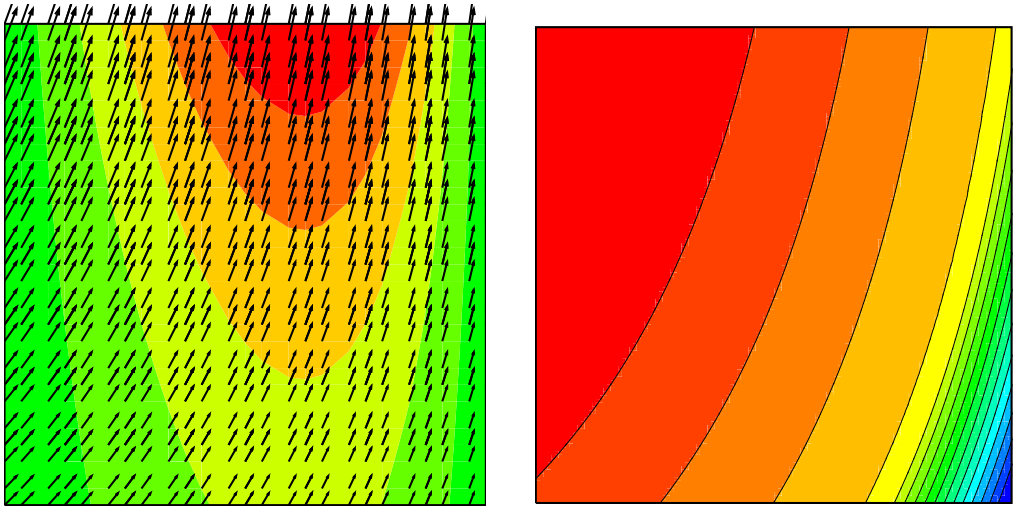

(a) Primal solution (b) Adjoint solution

Figure 4.2: The primal and adjoint solution of the linear advection equation.

SPs	g	primal L_2 err.	output error	output error est.	corrected output error
Gauss	DG	k+1	2k+1	2k+1	2k+3
Lobatto	DG	k+1	2k	2k	2k+2
Gauss	G2	k+1	2k	2k	2k+2
Gauss	G3	k+1	2k-1	2k-1	2k+1

Table 4.1: Convergence rates for the linear wave equation with different schemes.

error. The difference between them are within machine zero.

4.5.2 The Supersonic Vortex Transportation Problem

Second, we test the present adjoint-based error estimation for the Euler equations with curved elements. The problem we consider is a 2D supersonic vortex transported in a circular sector. The computational domain is defined on a section of an annulus with the inner radius of $r_{in} = 1$ and the outer radius of 1.384. The initial mesh consists of $k = 4$ quadrilateral elements and is shown in Figure 4.5a. The isentropic vortex rotates around the center of the circular sector. The density ρ is only a function of the radius r (Figure 4.5b)

$$\rho(r) = \rho_{in}(1 + \frac{\gamma - 1}{2} M_{in}^2 (1 - \frac{r_{in}^2}{r^2}))^{\frac{1}{\gamma - 1}},$$

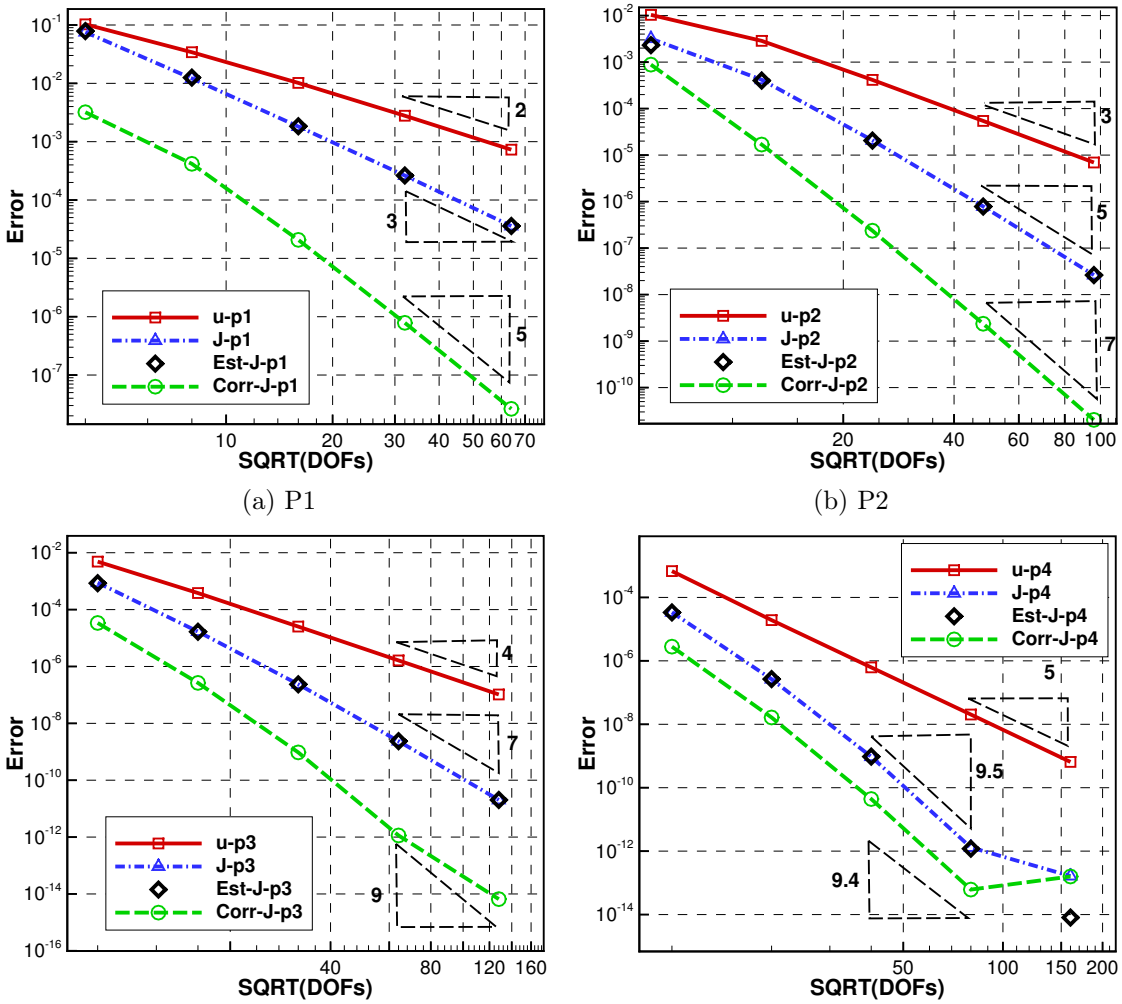

(a) P1 (b) P2

(c) P3 (d) P4

Figure 4.3: Results for the linear advection equation using a CPR scheme with the Gauss points and g_{dg}.

where γ is the ratio of heat capacities and the remaining parameters are the flow conditions on the inner surface chosen as $\rho_{in} = 2$, $M_{in} = 2$ and $p_{in} = \frac{1}{\gamma}$. The other variables can be computed with the isentropic relations. Characteristic boundary conditions with the analytical solution are used at both the inlet and the outlet, and slip wall boundary conditions are applied on the inner and the outer boundaries. The output of interest is the force in the x direction on the inner surface, where the pressure is equal to $\frac{1}{\gamma}$, so the exact value of the output is $\mathcal{J} = -\frac{1}{\gamma}$.

The output boundary operator j_τ is defined as $j_\tau = p\vec{n}\cdot\vec{i}_{dir}$, where $\vec{i}_{dir} = [1, 0]$. Therefore,

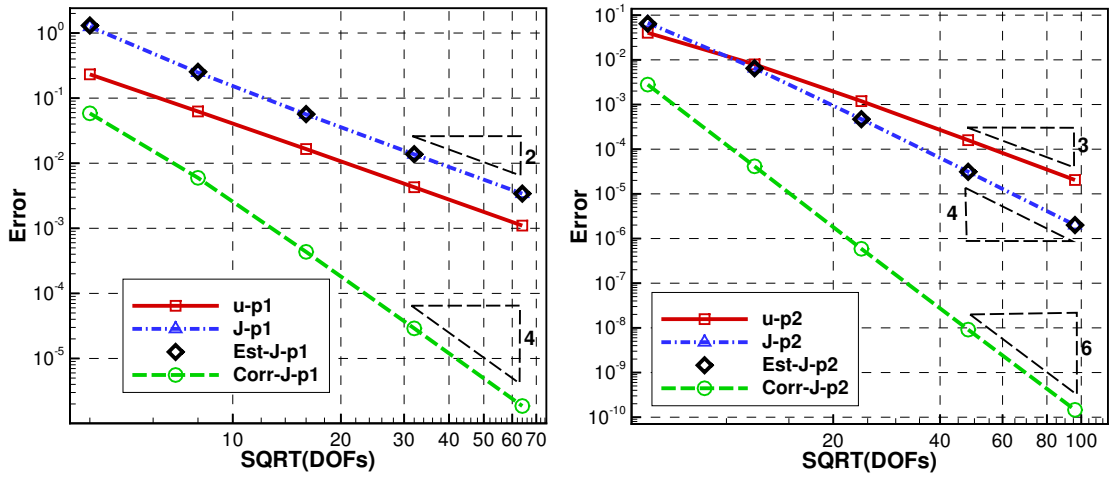

(a) Lobatto points with g_{dg} as the correction function

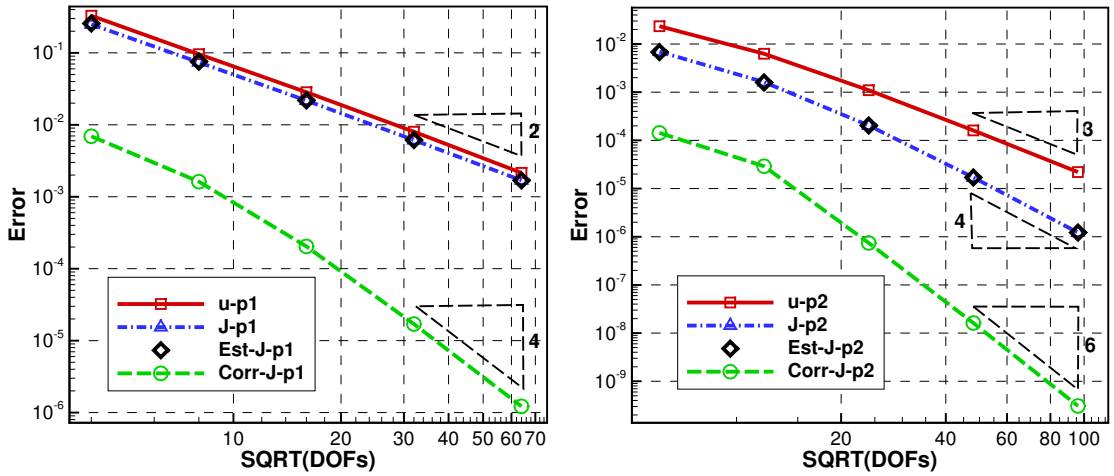

(b) Gauss points with g_2 as the correction function

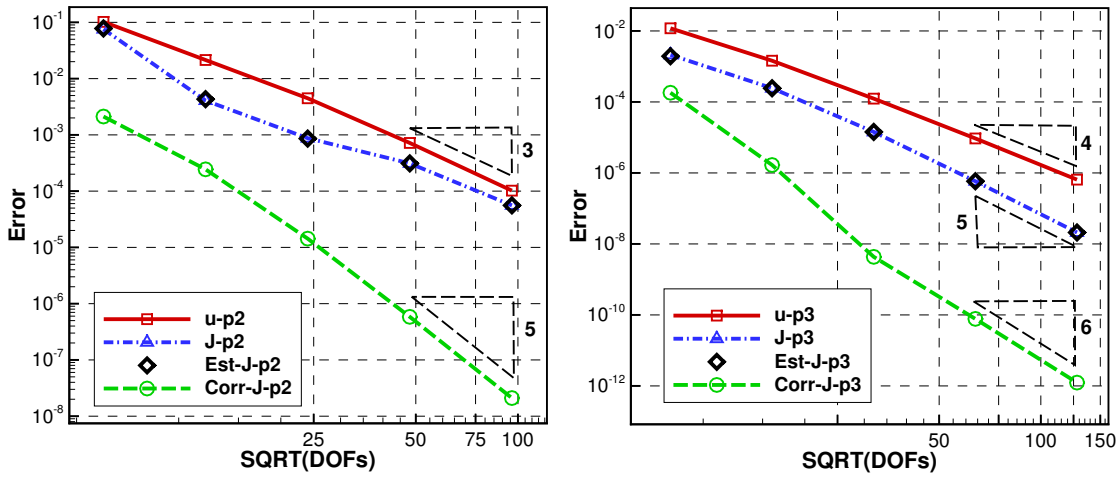

(c) Gauss points with g_3 as the correction function

Figure 4.4: Results for the linear advection equation with different correction functions.

Cells	$\mathcal{J}_H(Q_H) - \mathcal{J}_h(Q_h)$	$-(\psi_h)^T R_h(Q_h^H)$
4	-7.85516345138E-002	-7.85516345117E-002
16	-1.25394717994E-002	-1.25394717999E-002
64	-1.83796281052E-003	-1.83796281080E-003
256	-2.63400045419E-004	-2.63400045485E-004
1024	-3.58710248100E-005	-3.58710248149E-005

Table 4.2: The output error by the finite difference method and adjoint-based error estimation (coarse space $k = 1$, fine space $k = 2$).

the corresponding equation to Eq. 4.21 in 2D is

$$\int_{\partial\Omega} \psi^T \frac{\partial F^{com}}{\partial Q} ds = -\int_{\partial\Omega} \frac{\partial p}{\partial Q} (\vec{n} \cdot \vec{i}_{dir}) ds,$$

which is equivalent to the boundary condition for the continuous adjoint equation

$$\int_{\partial\Omega} \psi^T \frac{\partial p}{\partial Q} \begin{bmatrix} 0 \\ n_x \\ n_y \\ 0 \end{bmatrix} + (\vec{n} \cdot \vec{i}_{dir}) \frac{\partial p}{\partial Q} ds = 0,$$

with the flux

$$F^{com}(Q_{BC}(Q_L), \vec{n}) = \vec{n} \cdot \vec{F}(Q_{BC}(Q_L)) = p \begin{bmatrix} 0 \\ n_x \\ n_y \\ 0 \end{bmatrix},$$

chosen as the common flux on the boundaries. This ensures that the CPR method for the Euler equations with this output definition is a dual-consistent formulation.

The adjoint solution with the dual-consistent boundary conditions and dual-inconsistent boundary conditions are shown in Figure 4.5. The dual-inconsistent boundary conditions generated some spurious oscillations near the wall, while the adjoint solution from the dual-consistent boundary conditions was very smooth. Figure 4.6 displays the solution error, the output error and the adjoint-based error estimate. The optimal order of accuracy $k+1$ in L_2

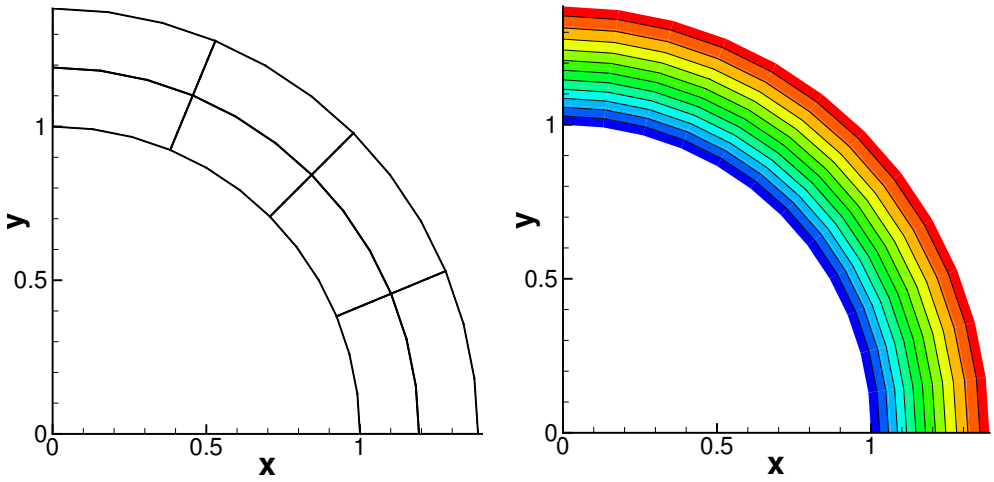

(a) The initial mesh

(b) Density

(c) Adjoint solution ψ_1 with dual-consistent BCs

(d) Adjoint solution ψ_1 with dual-inconsistent BCs

Figure 4.5: The primal and adjoint solution for the supersonic vortex transportation problem (Gauss points, g_{dg},$k = 3$).

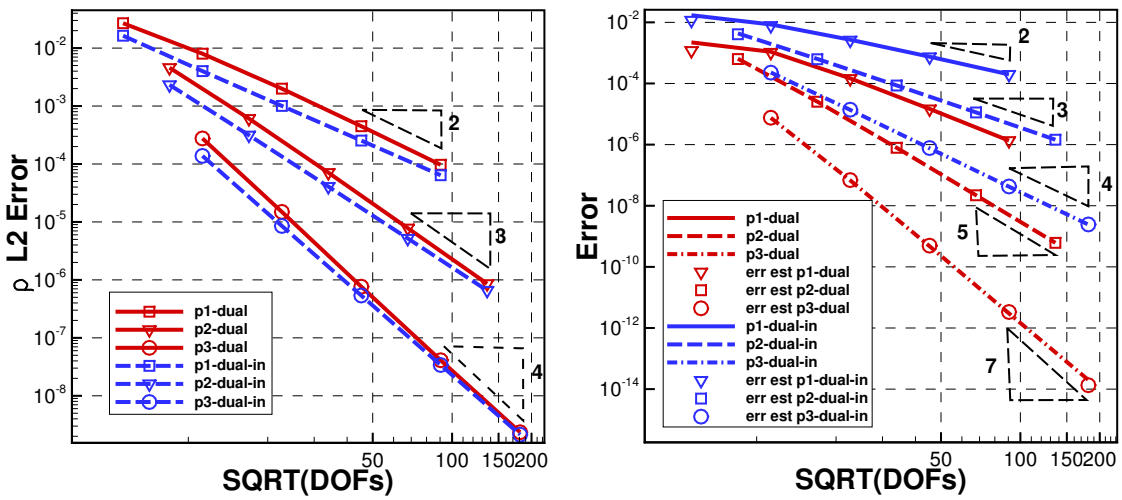

(a) L_2 density error

(b) Output error

Figure 4.6: The results of the supersonic vortex transportation problem using the dual-consistent BC and the dual-inconsistent BC (Gauss points, g_{dg}).

norm was obtained by both the dual-consistent and inconsistent boundary conditions in the primal solution. However, a super convergence of order $2k+1$ was observed for the output with the dual-consistent boundary condition only. The spurious adjoint oscillation caused by the dual-inconsistent boundary condition degraded the adjoint solution, and destroyed the super convergence property of the output functional.

Figure 4.7 and 4.8 show the convergence rates of the CPR method with different solution points using both the LP and the CR approaches. Similar results were obtained with the LP and CR approaches for the Gauss points: a super-convergence of order $2k+1$ for the output functional and the error estimate and a super convergence of $2k+3$ for the corrected output. This indicates that the dual-consistency violation of the CR approach is relatively weak, and does not affect the adjoint-based error estimate. However, with the Lobatto points and the LP approach, accuracy loss did occur. The super convergence of the corrected output is lost for the $k = 1$ scheme. The CPR schemes with Lobatto points and the CR approach can reduce the alias error generated by the non-linear fluxes. Even though the CR approach is not fully dual-consistent, the super convergence rates are recovered for the Lobatto points, whose output functional and the error estimate are accurate to a super convergence order

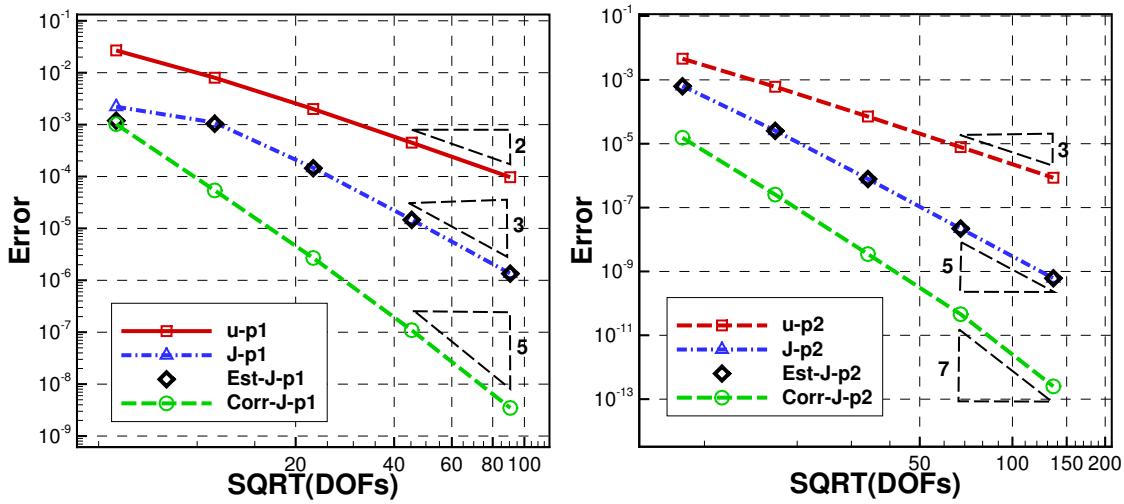

(a) Gauss points, LP and g_{dg}

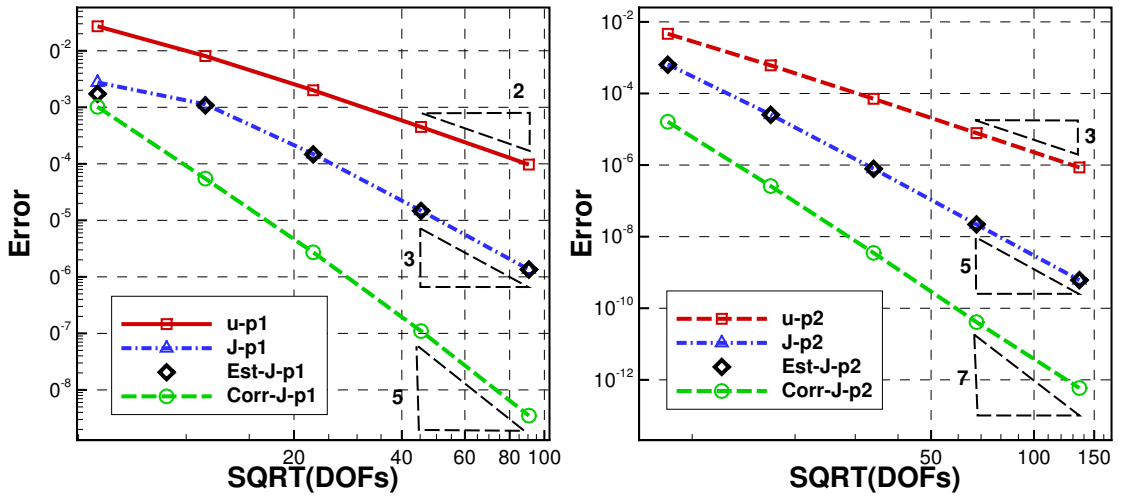

(b) Gauss points, CR and g_{dg}

Figure 4.7: The results of the supersonic vortex transportation problem with the Gauss points.

of $2k$ and the order of the corrected output is $2k+1$. Figure 4.9 shows the results of the CPR method with different correction functions. Similar results as for the linear advection equation are obtained. For the Euler equations, the output functional and the adjoint-based error estimate with the Gauss point and g_m are accurate to order $O(h^{2k+2-m})$. Furthermore, the corrected outputs of the corresponding schemes are accurate to order $O(h^{2k+4-m})$. The convergence rates with the different CPR schemes are summarized in Table 4.3. The results of this test case indicate that the dual-consistent formulation performs as expected for a non-linear equations and curved elements.

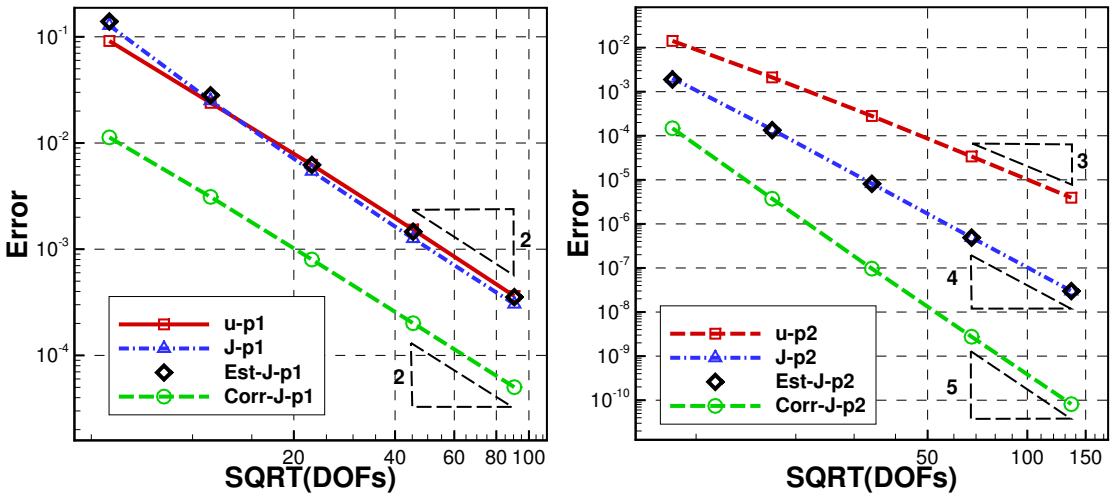

(a) Lobatto points, LP and g_{dg}

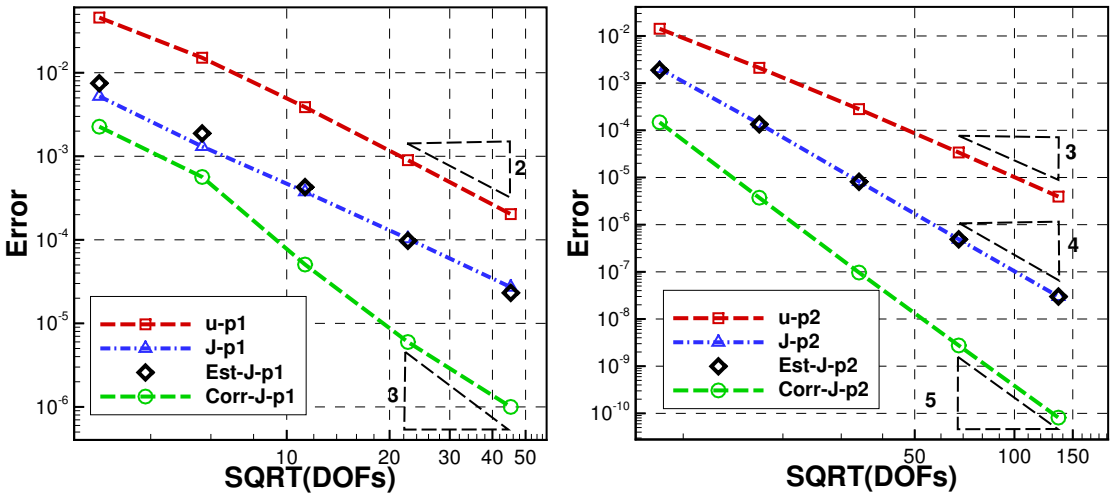

(b) Lobatto points, CR and g_{dg}

Figure 4.8: The results of the supersonic vortex transportation problem with the Lobatto points.

Table 4.3: Order of accuracy for the supersonic vortex transportation problem.

SPs	g	$\nabla \cdot \vec{F}$	primal L_2 err.	output error	output error est.	corrected output error
Gauss	DG	LP	k+1	2k+1	2k+1	2k+3
Gauss	DG	CR	k+1	2k+1	2k+1	2k+3
Lobatto	DG	LP	k+1	2k	2k	$\approx 2k+1$
Lobatto	DG	CR	k+1	2k	2k	2k+1
Gauss	G2	LP	k+1	2k	2k	2k+2
Gauss	G3	LP	k+1	2k-1	2k-1	2k+1

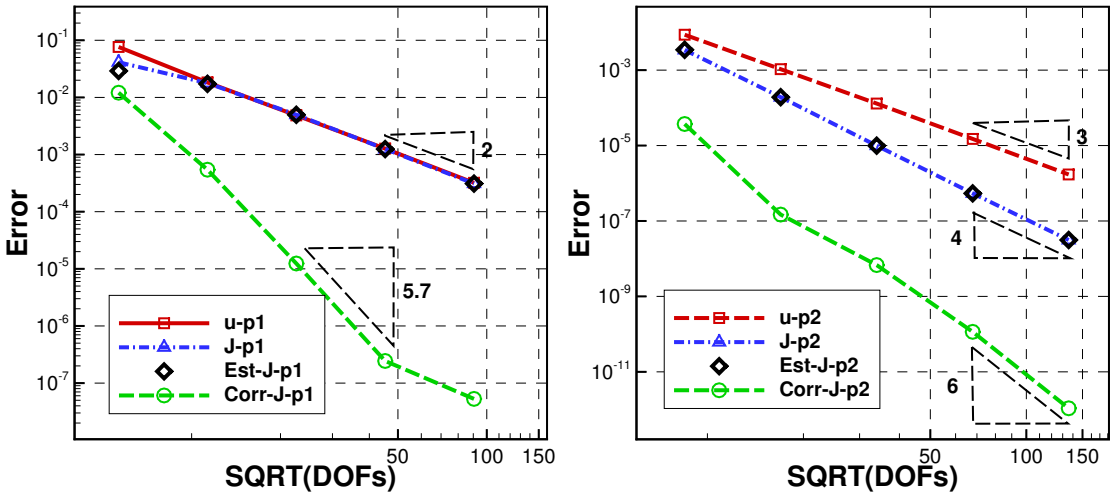

(a) Gauss points, LP and g_2

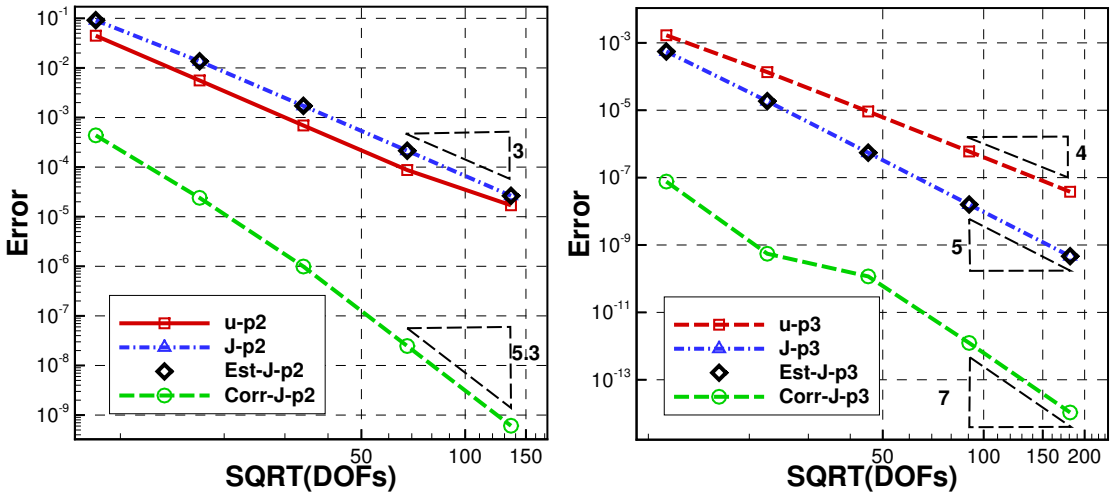

(b) Gauss points, LP and g_3

Figure 4.9: The results of the supersonic vortex transportation problem.

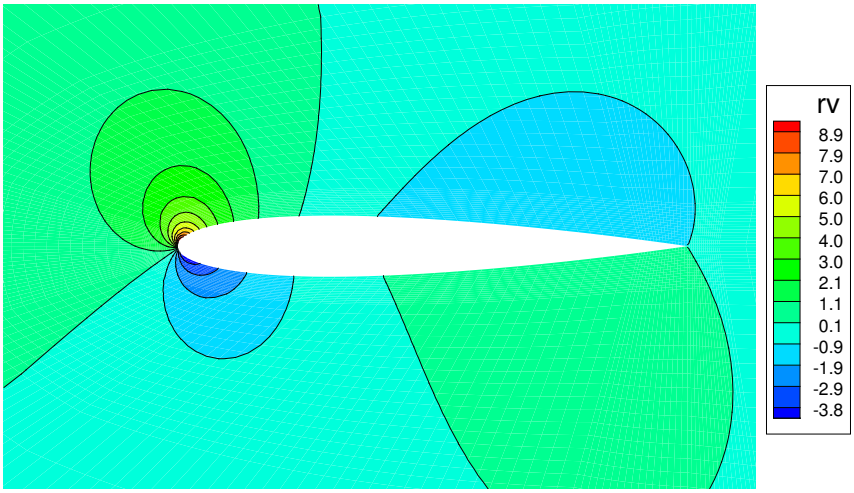

Figure 4.10: The 3^{rd} component of the C_D adjoint of an inviscid NACA 0012 airfoil at $M_\infty = 0.5, \alpha = 2°$.

4.5.3 Inviscid Flow over the NACA0012 Airfoil

The last test case in this section is a subsonic flow over a NACA0012 airfoil with a free-stream Mach number of $M_\infty = 0.5$ and an angle of attack, $\alpha = 2°$. It is used to further assess the accuracy of the adjoint-based error estimation for a problem with a geometric singularity. The output of interest is chosen as the lift or drag of the airfoil. The contours of the C_L adjoint and the C_D adjoint are shown in Figure 4.1b and Figure 4.10. In this test case, the error in the functional $\mathcal{J}_H(Q_H) - \mathcal{J}_h(Q_h)$ is computed using p-enrichment from $p = 2$ to $p = 3$ and the effectivity index of the error estimation is defined as

$$\eta_H^e = \frac{-\sum_j \omega_j |J_{i,j}| \, (\psi_h)_{i,j} \, r_{i,j}(Q_h^H)}{\mathcal{J}_H(Q_H) - \mathcal{J}_h(Q_h)}.$$

Due to the geometry singularity, the super convergence of the output functional and its error estimate is lost. Table 4.4 shows the results with 4 levels of uniformly refined meshes. Note that the error of the initial estimates on the very coarse meshes is large; however, the effectivity index η_H^e approaches unity as the mesh is refined for both C_L and C_D. In addition,

the error estimate with the C_D adjoint is more accurate than with the C_L adjoint. This is due to the fact that the regularity of the C_L adjoint is low because of the singularity along the stagnation streamline from the leading edge, while the C_D adjoint is relatively smooth.

Table 4.4: Adjoint-based error estimate for an inviscid NACA 0012 airfoil at $M_\infty = 0.5, \alpha = 2^\circ$ (coarse space $k = 2$, fine space $k = 3$).

Cells	C_L			C_D		
	$\mathcal{J}_H(Q_H) - \mathcal{J}_h(Q_h)$	$-(\psi_h)^T R_h(Q_h^H)$	η_H^e	$\mathcal{J}_H(Q_H) - \mathcal{J}_h(Q_h)$	$-(\psi_h)^T R_h(Q_h^H)$	η_H^e
280	-8.90E-03	-1.84E-02	2.064	8.39E-03	8.51E-03	1.015
1120	-5.52E-03	-7.15E-03	1.295	1.93E-03	1.95E-03	1.011
4480	-1.59E-03	-1.68E-03	1.058	2.29E-04	2.29E-04	1.002
17920	-3.08E-04	-3.24E-04	1.049	2.13E-05	2.13E-05	0.999

Chapter 5

Output-based Error Estimation and Adaptation

5.1 Adjoint-based Adaptation and Error Indicators

An adjoint-based error estimation relates a specific functional output error directly to the local residual error. Therefore, it can be used to construct a very effective error indicator to drive an adaptive procedure for any engineering output. From Eq. 4.8, the output error can be estimated by performing a quadrature rule as

$$\delta \mathcal{J}_h(Q_h) \approx -\sum_i \sum_j \omega_j |J_{i,j}| \psi_{i,j} r_{i,j}(Q_h^H).$$

The continuous adjoint solution ψ is approximated by solving ψ_h on the finer space through enriching the degree of the solution polynomial. The finer solution Q_h is obtained by performing several iterations of GMRES relaxation after prolongating from the coarse solution Q_H

$$Q_h^H = I_h^H Q_H,$$

with an injection operator I_h^H. The adjoint-based local error indicator η_i used in the present study is defined by taking an absolute value of the elemental output error contribution

$$\eta_i = |\sum_j \omega_j |J_{i,j}| \left(\psi_h - I_h^H \psi_H\right)_{i,j} r_{i,j}(Q_h^H)|.$$

To achieve a better estimate, the adjoint defect between the coarse level and fine level $\psi_h - I_h^H \psi_H$ is used. For a system of equations, the local error indicator is formed by summing together every component's contribution to the functional error estimate.

5.2 The Local Output-error Sampling Procedure

The error indicators defined above are used to drive a fixed-fraction anisotropic h-adaptation. In this approach, a certain fraction f of the current elements with the largest local error indicators η are marked for h-refinements. Then the anisotropic adaptation decision is driven by an error sampling procedure for choosing the optimal refinement from a discrete set of adaptation choices. The idea of guiding anisotropy adaptation for the engineering output by solving local problems has been previously proposed in [19, 38, 63, 122]. The elemental functional error is directly estimated and monitored during the sampling process. For quadrilaterals, as shown in Figure 5.1, three local refinement options are available: isotropic-refinement, x-refinement, y-refinement. For a simplex element, we consider four local refinement options by splitting the edges, as shown in Figure 5.2.

Mesh refinement is performed in the original element's polynomial space using the reference coordinates. So the refined elements inherit the same geometry approximation order. However, for elements on the geometry boundaries, the newly generated vertex on the boundary edge may not be exactly on the real geometry. An extra remapping process is employed to snap the boundary points to the truth geometry during each adaptation level. As shown in Figure 5.3, non-conforming interfaces between cells with different h levels are created during the adaptation process. In order to maintain the smoothness of the solution, at most one

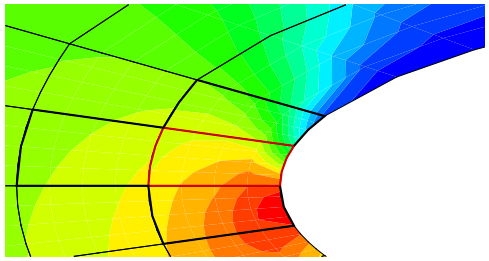

(a) Primal sol. $Q_H = \rho$, the coarse mesh

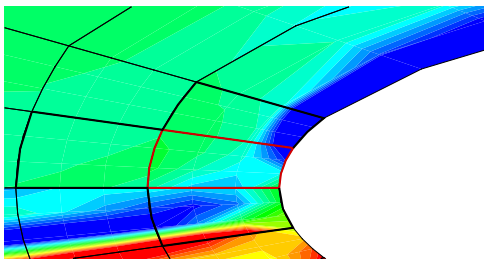

(b) Adjoint sol. $\hat{\psi}_H$, the coarse mesh

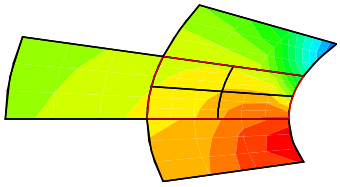

(c) $Q^H_{\kappa_0}$, iso

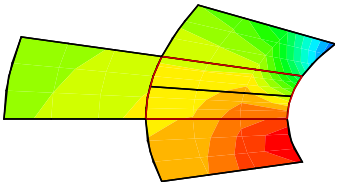

(d) $Q^H_{\kappa_1}$, x-ref

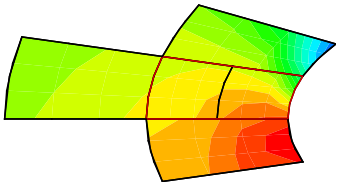

(e) $Q^H_{\kappa_2}$, y-ref

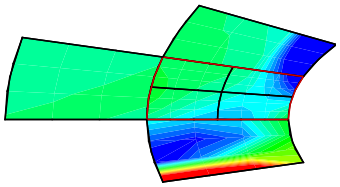

(f) $\hat{\psi}^H_{\kappa_0}$, iso

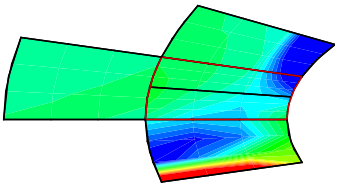

(g) $\hat{\psi}^H_{\kappa_1}$, x-ref

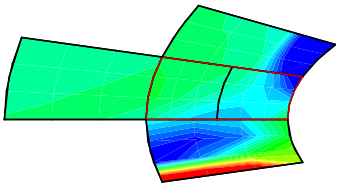

(h) $\hat{\psi}^H_{\kappa_2}$, y-ref

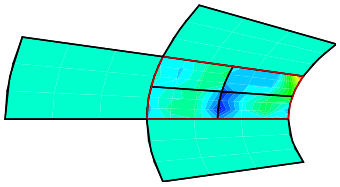

(i) Residual $\mathcal{R}_{\kappa_0}(Q^H_{\kappa_0})$, iso

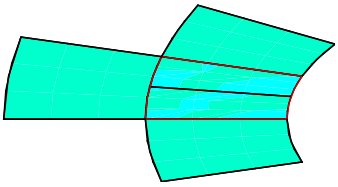

(j) Residual $\mathcal{R}_{\kappa_0}(Q^H_{\kappa_1})$, x-ref

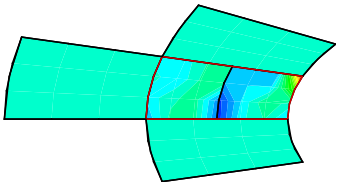

(k) Residual $\mathcal{R}_{\kappa_0}(Q^H_{\kappa_2})$, y-ref

Figure 5.1: The local output error sampling procedure for quadrilateral elements.

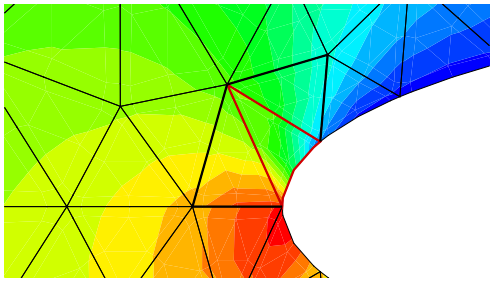

(a) Primal sol. ρ, the coarse mesh

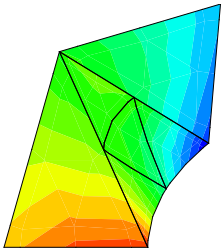

(b) Iso refinement

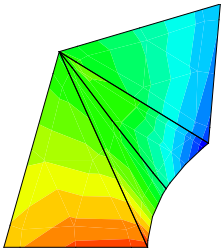

(c) Edge 1 Split

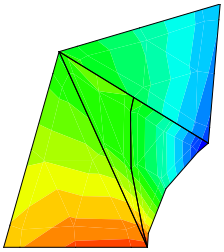

(d) Edge 2 Split

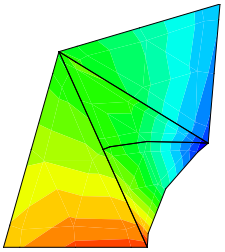

(e) Edge 3 Split

Figure 5.2: The simplex refinement options for probing the local functional error behavior.

level of difference is allowed for h-refinement. For the simplex anisotropic adaptations, as shown in Figure 5.4, the hanging nodes can be completely removed by refining its face neighbors. This is in contrast to the quadrilateral meshes which always generates the hanging nodes after refinements.

For each refinement option denoted as κ_j of the candidate element i marked by the local error indicators η, an element-wise local problem is created and solved dynamically at each adaptation step. As shown in Figure 5.1, all of elements in the stencil of the candidate element i are created and the current primal solution Q_H and adjoint solution $\hat{\psi}_H$ are injected by the prolongating operator $I^H_{\kappa_j}$

$$Q^H_{\kappa_j} = I^H_{\kappa_j} Q_H \tag{5.1}$$

and

$$\hat{\psi}^H_{\kappa_j} = I^H_{\kappa_j} \hat{\psi}_H. \tag{5.2}$$

The residual or perturbation created by the refinement option κ_j is evaluated. Then the

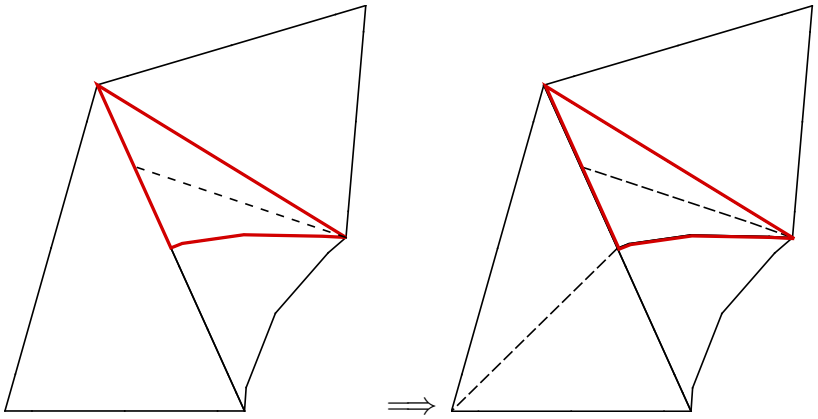

(a) Triangle elements

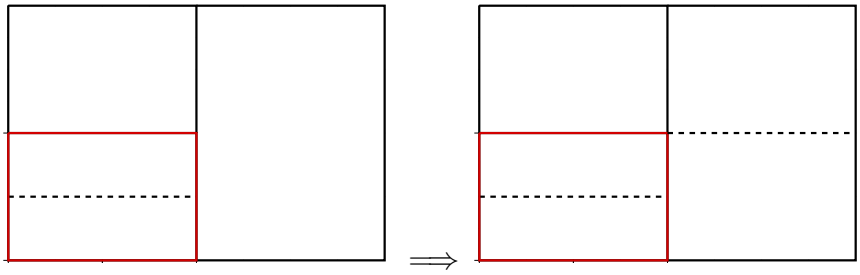

(b) Quadrilateral elements

Figure 5.3: Hanging nodes with the one level difference restriction.

locale functional error indicator can be obtained using

$$\eta_{\kappa_j} = |(\hat{\psi}^H_{\kappa_j})^T \mathcal{R}_{\kappa_j}(Q^H_{\kappa_j})|. \tag{5.3}$$

Finally, a simple merit indicator m_{κ_j} defined as

$$m_{\kappa_j} = \frac{benefit}{cost} = \frac{\eta_{\kappa_j}}{DOF^2}. \tag{5.4}$$

are used to pick up a particular refinement option in this paper.

A compressible Couette flow problem is used to verify the directional feature detective ability of the current local solve procedure. In this case, the laminar flow is driven by viscous force in the space between two parallel moving plates. The speed of the upper wall is $U = 0.3$ with constant temperature $T_1 = 0.85$. The lower wall is fixed and the temperature is enforced

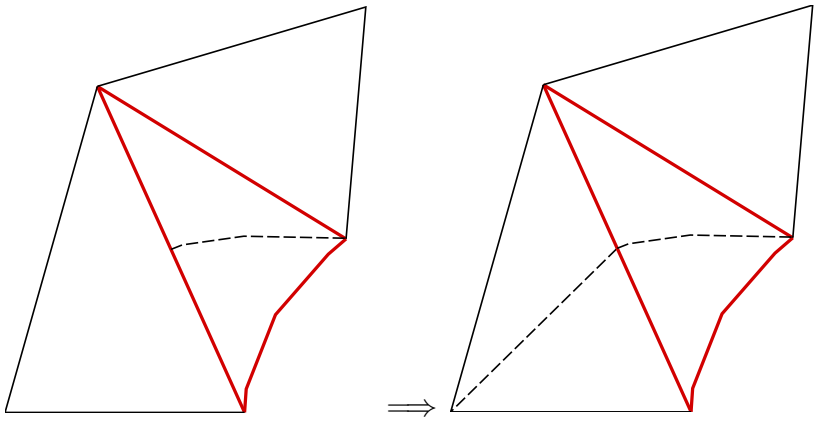

(a) Remove hanging nodes, 1 edge

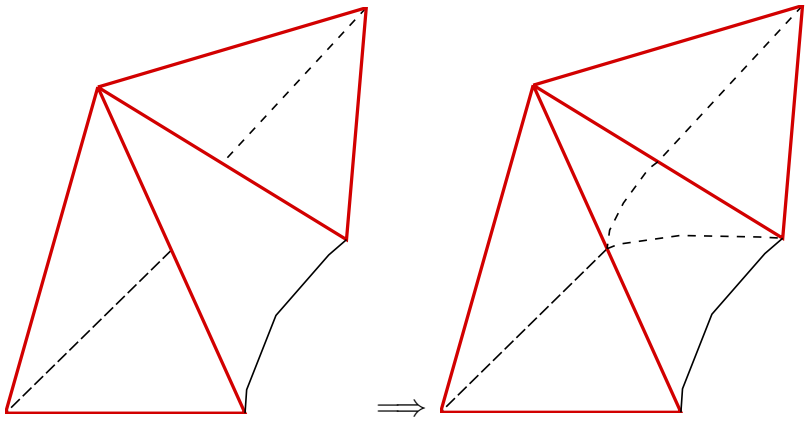

(b) Remove hanging nodes, 2 edges

Figure 5.4: Remove hanging nodes during the refinements.

to $T_0 = 0.8$. The dynamic viscosity of the fluid is $\mu = 0.01$. The analytic solution for this problem is:

$$u = \frac{U}{H}y, \quad v = 0, \tag{5.5}$$

$$p = Const, \quad \rho = \frac{p}{RT}, \tag{5.6}$$

$$T = T_0 + \frac{y}{H}(T_1 - T_0) + \frac{\mu U^2}{2k}\left(1 - \frac{y}{H}\right), \tag{5.7}$$

where R is the gas constant and k is the thermal conductivity. So the solution is only changed along the y direction. Figure 5.5a shows the initial mesh. For the purpose of the verification, on every adaptation stage, all of the current cells are marked as the candidate elements to do the refinement. The unweighted residual-based local error sampling procedure, which

means adjoint $\hat{\psi} = 1$ in Eqn. 5.3.,is used to find the best refinement opition for every element. Figure 5.5b presents the adapted mesh on the final stage. The result indicates that the optimal mesh along the x direction is generated from the local solve procedure. No refinement in the x direction are performed. Figure 5.5c plots the estimate merit indicator for each refinement option. Compared with the isotropic refinement, the huge degree of freedom saving per $L2$ density error from the local sampling procedure are obtained, as shown in Figure 5.5d.

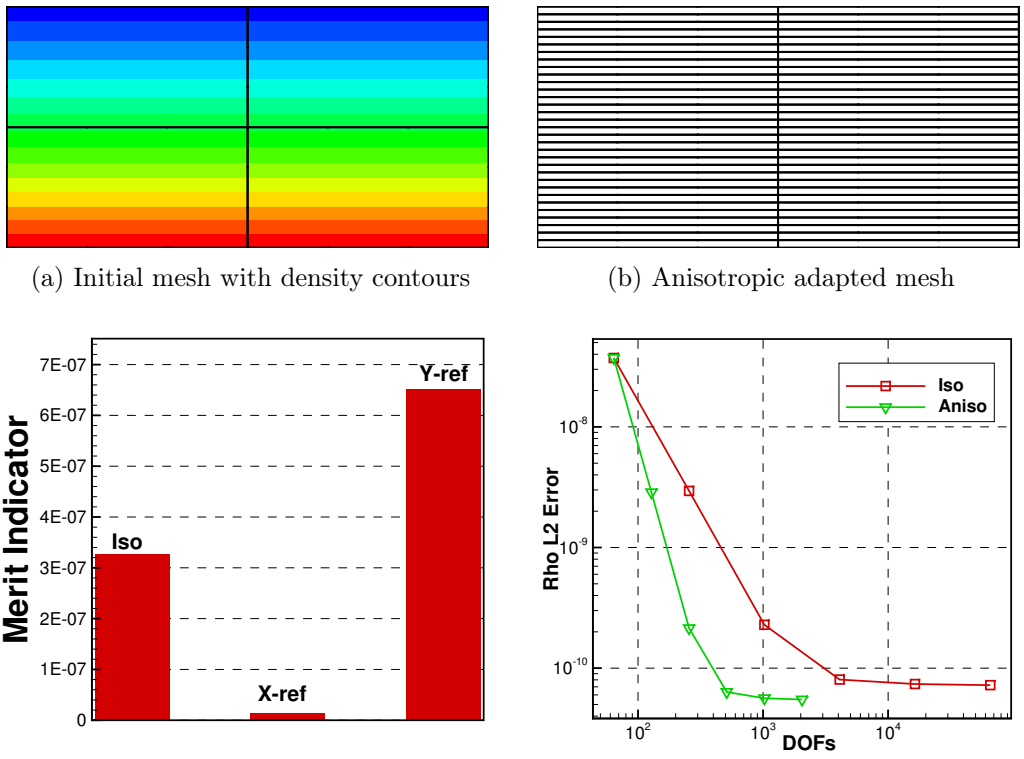

(a) Initial mesh with density contours

(b) Anisotropic adapted mesh

(c) Local error estimation for one cell

(d) L_2density error

Figure 5.5: Local error sampling refinements for the compressible Couette flow ($k = 3$).

5.3 Non-conforming Interface

Non-conforming interfaces between cells with different h or p levels are created during the adaptations. See Figure 5.6 on page 105. As mentioned previously, only one level difference of h and p between neighboring cells are allowed. Special treatment is required when computing the common numerical flux on those non-conforming interfaces with hanging nodes. The "mortar" element method developed by Kopriv[60] is used here. Basically, a L_2 projection is used to preserve the global conservation and maintain the accuracy. For a non-conforming interface, a "mortar" face is introduced to link the unmatched elements, whose space are always chosen as the higher h or p space of the two sides. First, the solution from the left and right sides of the face are prolongated to the mortar surface by a simple interpolation process (see Figure 5.7a on page 105). Then, the common flux are computed by solving the Riemann problem on the mortar surface. The last step is to project the common flux on the mortar surface back to the original space. Here, the standard L_2 projection is utilized to preserve the average.

Let's take a 2D non-conforming h-surface as a example to illustrate the projection procedure. Here, one mortar element links one coarse surface denoted by σ on one side and multiple finner surfaces denoted by σ_k on the other side (see Figure 5.7b on page 105). Denote the DOFs on the coarse surface σ by Q_j and its basis function by ϕ_j, $j = 1, ..., K$, where K is the number of FPs on that surface. In addition, let $\hat{Q}_{k,j}$ and $\hat{\phi}_{k,j}$ stand for the DOFs and its basis on the k_{th} finner surface σ_k, where $j = 1, ..., K$. The standard L_2 projection from the finner space to the coarse space can be written as,

$$\sum_{k=1}^{nk}\sum_{,j=1}^{K}(\int_{\sigma_k}\phi_i\hat{\phi}_{k,j}d\xi d\eta)\hat{Q}_{k,j} = \sum_{j=1}^{K}(\int_{\sigma}\phi_i\phi_j d\xi d\eta)Q_j,$$

where nk stands for the number of the finner surface connected to the mortar element, which is equal to 2 in 2D and 4 in 3D. Note that the integral on the RHS is the mass matrix evaluated on the coarse space. If the standard Gauss quadrature points are used as the FPs,

the shape function ϕ_i defined on each FP is orthogonal to each other, which leads to

$$\int_{\sigma} \phi_i \phi_j d\xi d\eta = \delta_{i,j},$$

where

$$\delta_{i,j} = \begin{cases} 0 & i \neq j \\ 1 & i = j \end{cases}$$

is the Kronecker delta function.

Thus, the DOFs on the coarse space can be obtained by

$$\sum_{k=1}^{nk} \sum_{,j=1}^{K} \mathbf{R}_{i,(k,j)} \hat{Q}_{k,j} = Q_i.$$

Note $\mathbf{R}_{i,(k,j)}$ stands for the restriction matrix defined as

$$\mathbf{R}_{i,(k,j)} = \int_{\sigma_k} \phi_i \hat{\phi}_{k,j} d\xi d\eta,$$

which can be computed and stored in the preprocessing stage. Similar procedures can be obtained for the non-conforming p-interface. Detailed discussion of the "mortar" method can be found in Ref. [34, 59].

To assess the accuracy of the mortar method, the 3D vortex propagation case described in section 3.5.6 is simulated on a hexahedral grid with hanging nodes. The hanging nodes are generated randomly on the initial mesh across the whole computational domain. Then, the uniform h-refinement study is performed for the CPR method with $k = 1 \sim 5$. Figure 5.8 shows the density contours with $k = 1$ to $k = 5$ on the coarsest mesh. The solution is quite smooth, which indicates that the flow field is not degenerated by the non-conforming surfaces. Figure displays the L2 density error. The optimal orders of accuracy are obtained for the CPR method with the mortar element.

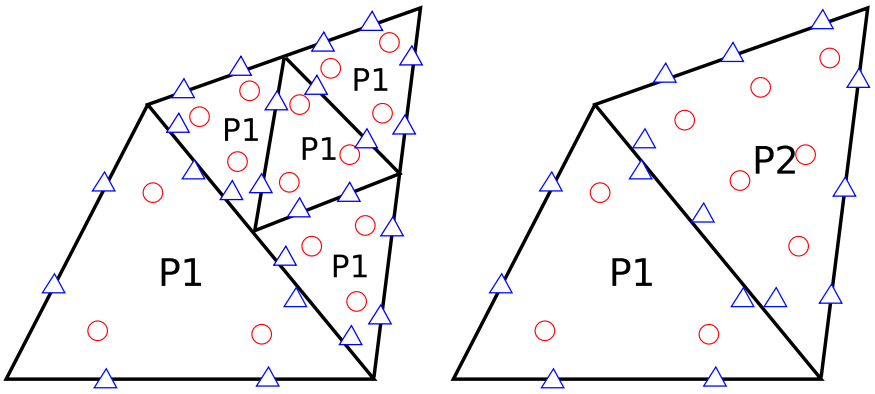

(a) Non-conforming h-surfaces (b) Non-conforming p-surfaces

Figure 5.6: Non-conforming interfaces with the hp-adaptation (◯: SPs, △: FPs).

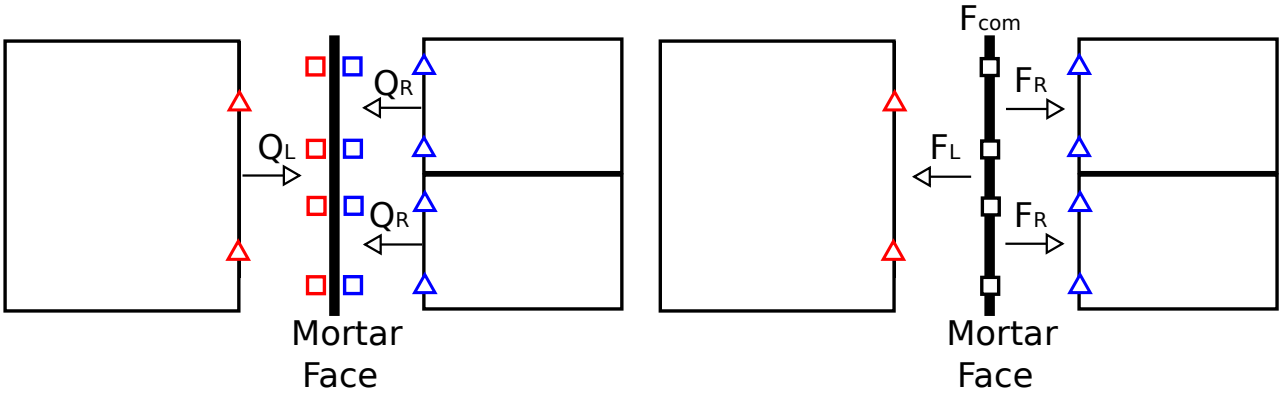

(a) Solution prolongation (b) Common flux restriction

Figure 5.7: The mortar face method for non-conforming faces ($k = 1$, △: FPs, □: DOFs on the mortar face).

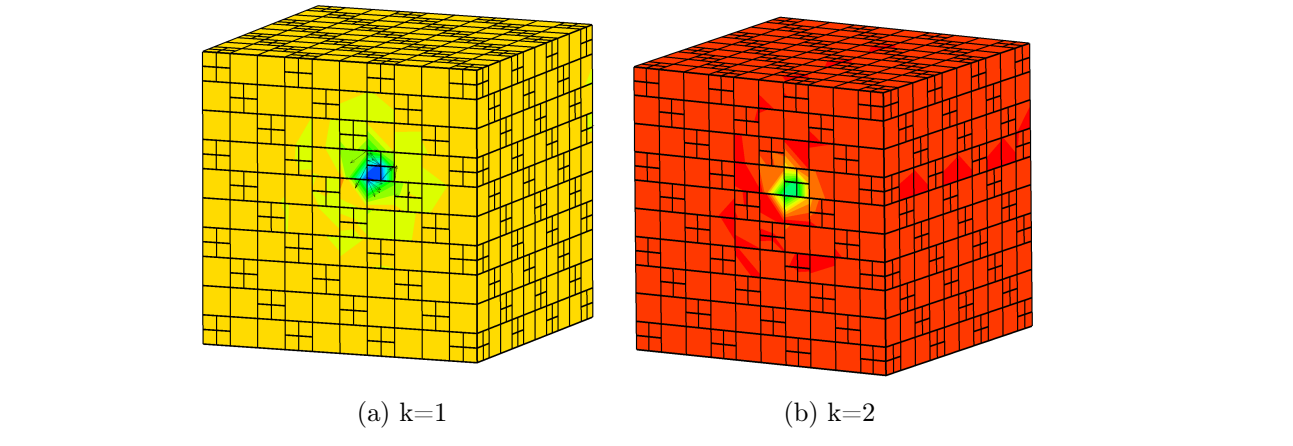

(a) k=1 (b) k=2

(c) k=3 (d) k=4 (e) k=5

Figure 5.8: Density contours of the vortex propagation with non-conforming interfaces.

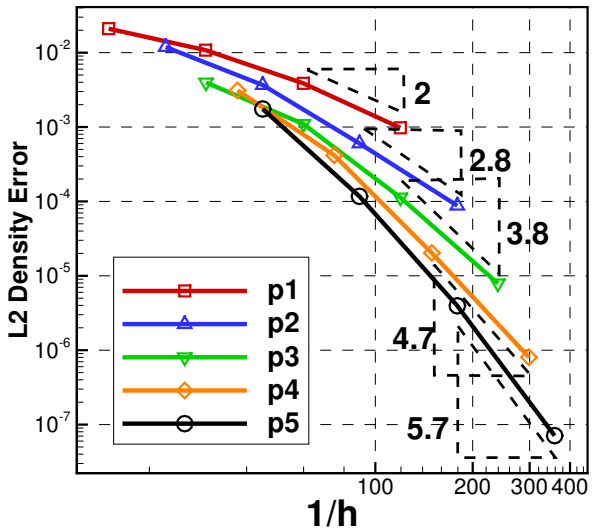

Figure 5.9: L2 density error of the vortex propagation with hanging nodes.

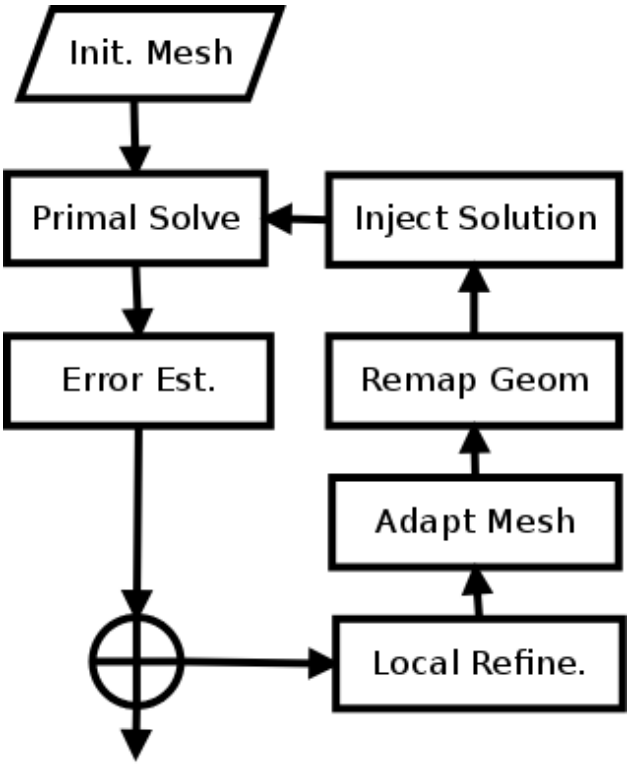

Figure 5.10: The procedure of the adjoint-based h-adaptation.

5.4 Adaptation procedure

Figure 5.10 shows the procedures of the adjoint-based h-adaptation. A fixed-fraction hanging-node h-adaptation strategy is used in the present study. At each adaptation step, a fixed fraction f of the candidate elements with the largest error indicators are adapted. The marked elements are refined through its local mapping functions. As a result, the newly inserted boundary points may not lie on the geometry. In order to ensure the accuracy of the geometry approximation, all of the newly inserted boundary points are remapped to the real geometry by querying the stored geometry information for each boundary element. Then the coordinates of the interior points of the modified elements are updated by a transfinite

interpolation from the boundary points.

Chapter 6

Numerical Results

6.1 Inviscid Flow over the Gaussian-shaped Bump

The test case of inviscid flow over a Gaussian-shaped bump is used to assess the effectiveness of h- and p-adaptation. The geometry of the bump surface and boundary conditions are chosen to be the same as the section 3.5.2. Only the residual-based error estimation is used to drive the adaptation. The simulation starts from a uniform 2^{nd} order scheme ($k = 1$), and then performs five loops of adaptations. A fixed fraction of adaptation on each level is chosen to be $f = 0.1$. As shown in Figure 6.1 on the next page, both of h- and p-adaptation are mainly performed around the bump surface. The result shows that the residual-based indicator clearly identifies the error source, which is the bump surface in this case. After performing 5 adaptation iterations, the non-conforming surfaces with h and p hanging nodes do not pollute the solution smoothness. Compared with the result of uniform 2^{nd} order scheme, the flow field at the final adaptation level is much more smooth especially in the adapted area. L_2 entropy error over the whole domain is used as a measure of accuracy, which is defined as

$$\|Error\|_{L_2} = \sqrt{\frac{\int_\Omega (\frac{p/\rho^\gamma - p_\infty/\rho_\infty^\gamma}{p_\infty/\rho_\infty^\gamma})^2 \mathrm{d}V}{\int_\Omega \mathrm{d}V}}. \tag{6.1}$$

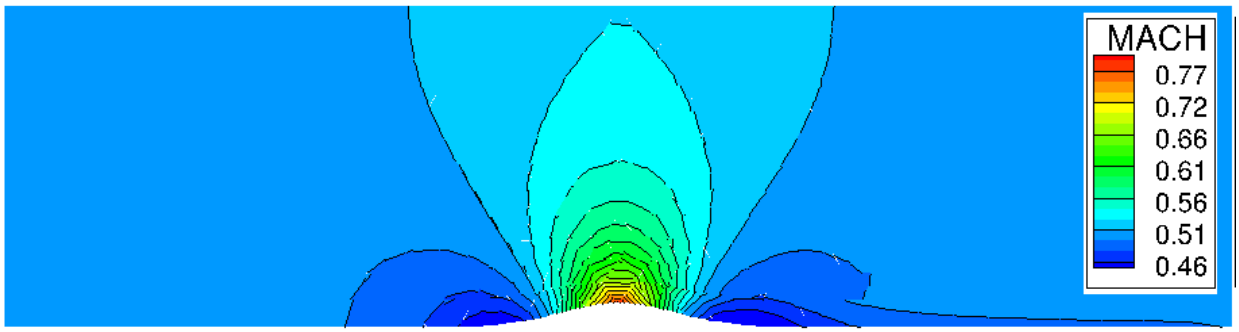

(a) Mach number, the initial mesh, $p = 1$

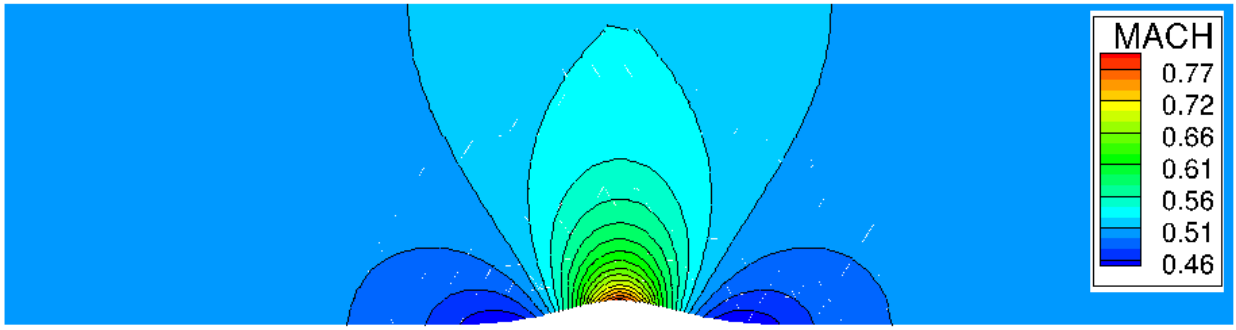

(b) Mach number, 5 levels of p-adaptation

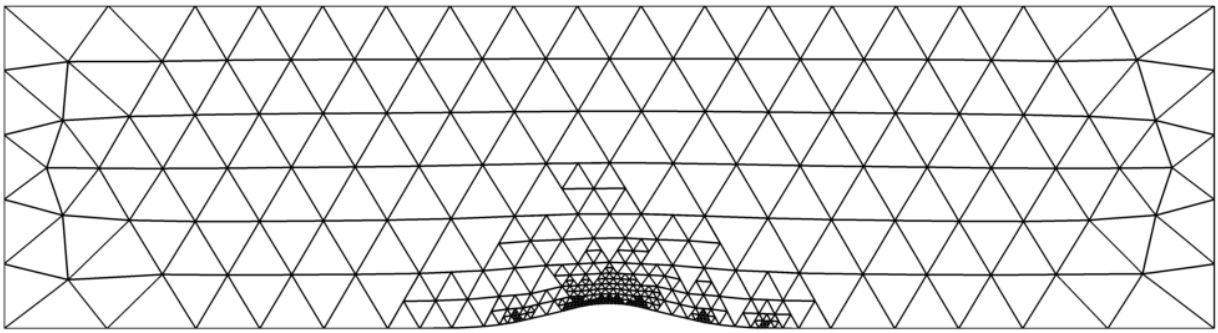

(c) The final h-adapted mesh

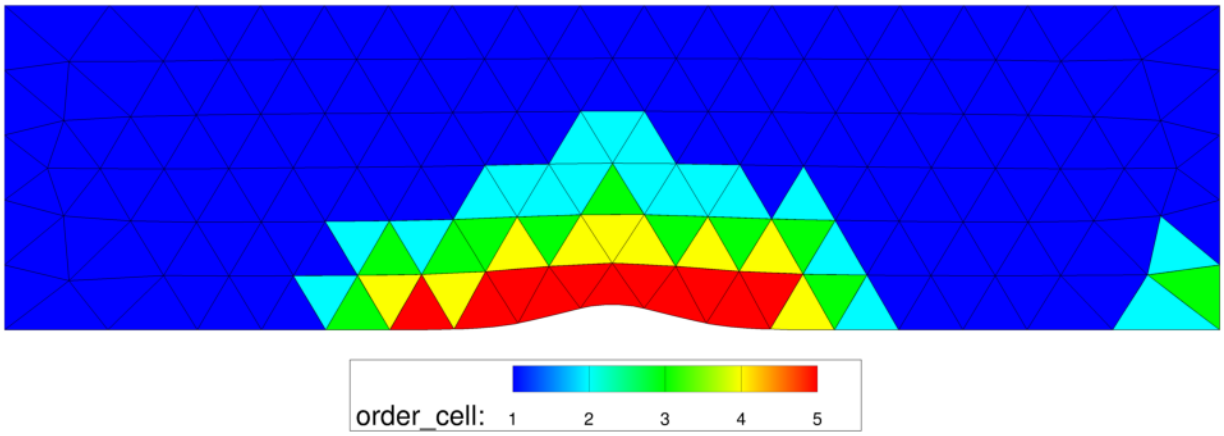

(d) The order distributions on the final p-adaptation

Figure 6.1: The residual-based h and p-adaptation for subsonic flow over a Gaussian-shaped bump.

For this simple case, the bump surface is quite smooth, which indicates a p-adaptation is preferred. Figure 6.2 shows the L_2 entropy error versus degrees of freedom with the residual-based h- and p-adaptation. Results of uniform h and p refinements are given for comparison too. Both of the h-adaptation and p-adaptation demonstrate better performance than their corresponding uniform refinements. As expected, p-adaptation is more effective than the h-adaptation in terms of the entropy error per degrees of freedom for this particular smooth problem. Furthermore, the uniform p refinement outperforms the uniform h refinement, which indicates the advantage of high-order discretizations in smooth regions.

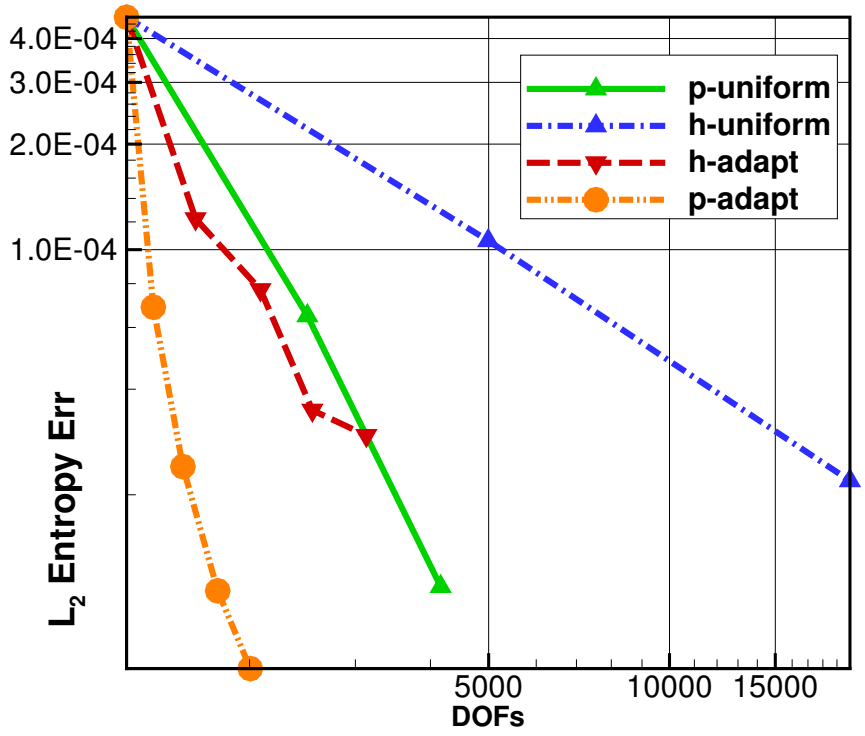

Figure 6.2: The L_2 entropy error of subsonic flow over a Gaussian-shaped bump.

6.2 Inviscid Flow over the NACA 0012 Airfoil

The next test case involves subsonic flow over a NACA 0012 airfoil with a free-stream Mach number of $M_\infty = 0.5$ and an angle of attack, $\alpha = 2°$. To assess the effectiveness of different error indicators, h-adaptations with C_L and C_D as the output of interest are performed on a quadrilateral grid. We use the 4^{th} order CPR scheme with the Gauss points as the SPs/FPs and the LP approach. The newly inserted grid points on every adaptation stage are remapped to the real NACA0012 airfoil to reduce the geometry approximation error. The initial mesh consists of 560 $p4$ curved elements. The start mesh and the final adapted meshes using the lift and drag adjoint are shown in Figure 6.3. It is well-known that the trailing edge singularity can generate spurious entropy. Therefore, refinements near the trailing edge are very important to predict an accurate drag value. Figure 6.4 shows the regions near the trailing edge and around the airfoil surface are refined persistently. Adaptations using the lift adjoint added some degrees of freedom on the stagnation streamlines, where the lift adjoint solution is singular and oscillatory. Figure 6.5 displays the Mach and adjoint solution contours on the initial and adapted mesh. Note the significant improvements of the solution smoothness on the adapted mesh. This is due to the present adaptation framework considers both of the primal and adjoint solutions.

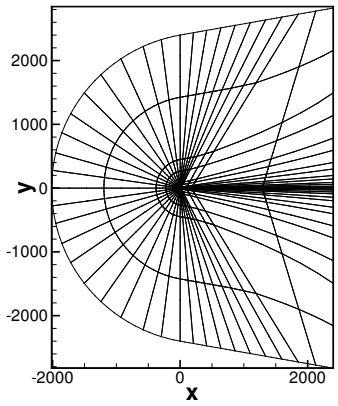

(a) The initial $p4$ mesh

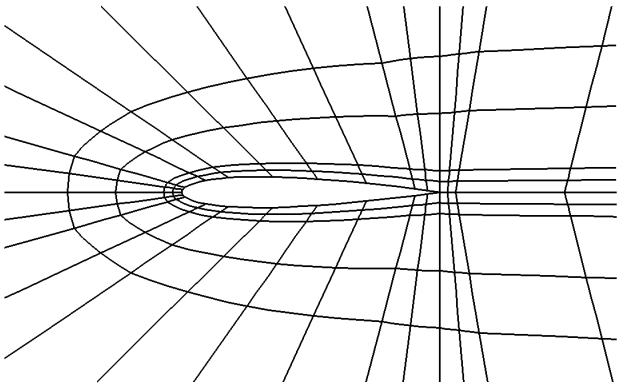

(b) The initial $p4$ mesh, zoom in

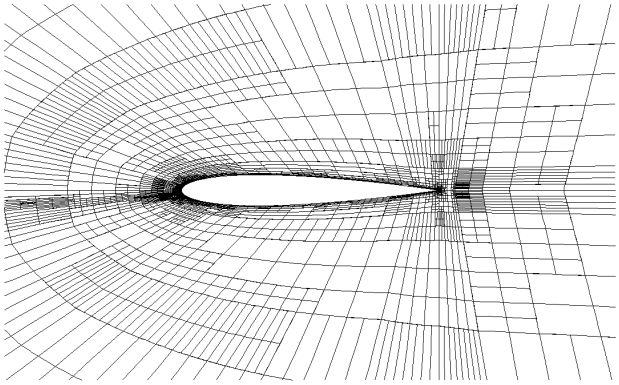

(c) C_L Adjoint

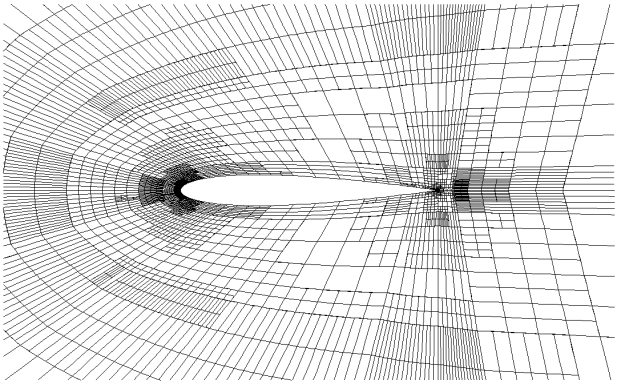

(d) C_D Adjoint

Figure 6.3: Adapted mesh for the adjoint-based h-adaptation for a inviscid NACA 0012 airfoil at $M_0 = 0.5,\ \alpha = 2^\circ$ $(k = 3)$.

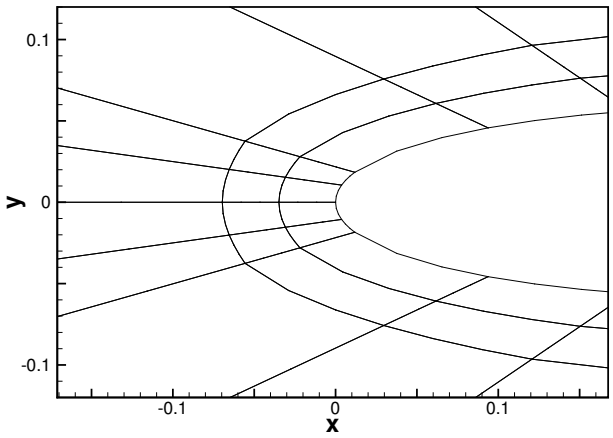

(a) Initial mesh near the leading edge

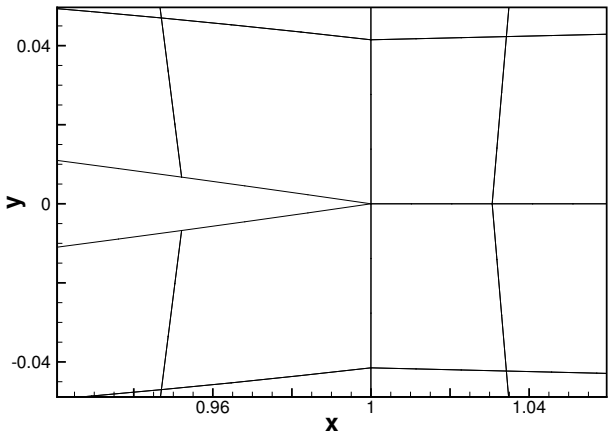

(b) Initial mesh near the trailing edge

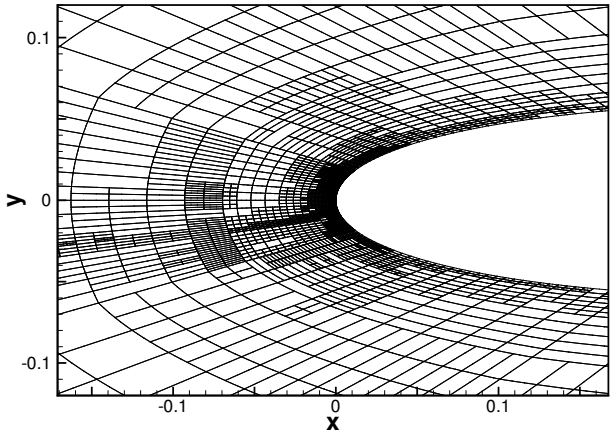

(c) Adapted mesh near the leading edge, C_L adjoint

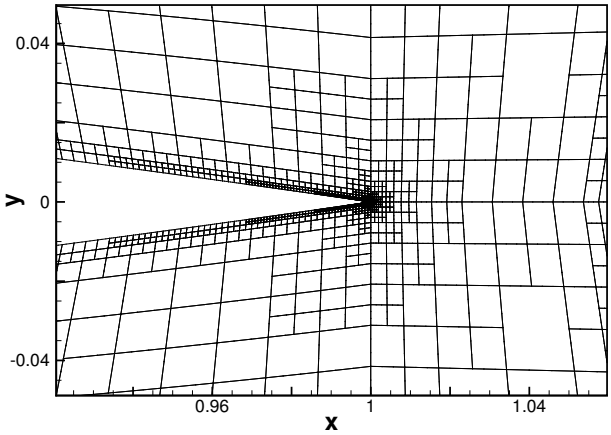

(d) Adapted mesh near the trailing edge, C_L adjoint

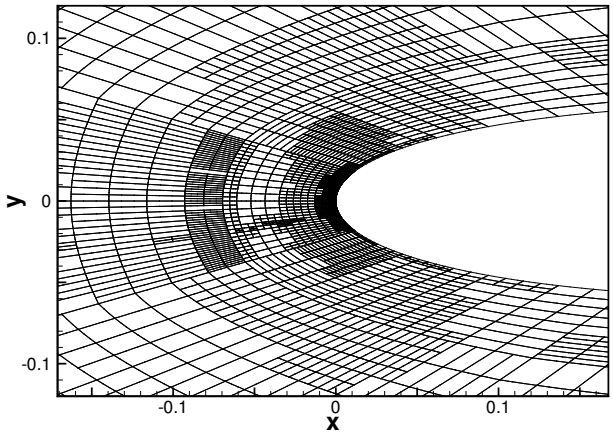

(e) Adapted mesh near the leading edge, C_D adjoint

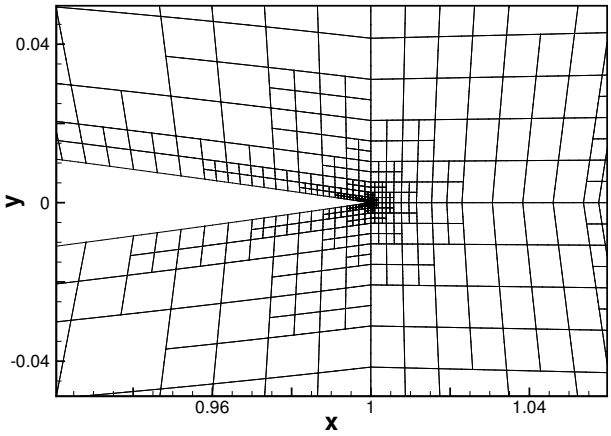

(f) Adapted mesh near the trailing edge, C_D adjoint

Figure 6.4: Detailed adapted mesh after 10 levels h-adaptation for a inviscid NACA 0012 airfoil at $M_0 = 0.5,\ \alpha = 2^\circ$ $(k = 3)$.

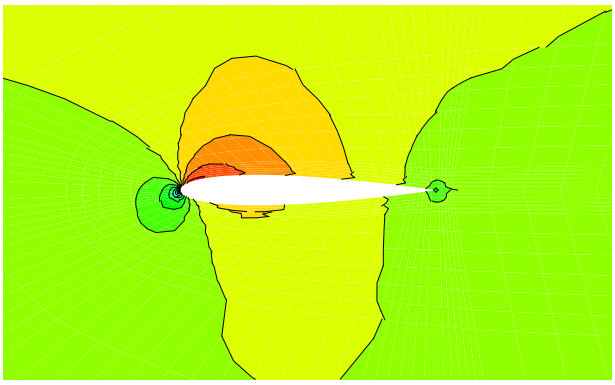

(a) Mach contours on the initial mesh

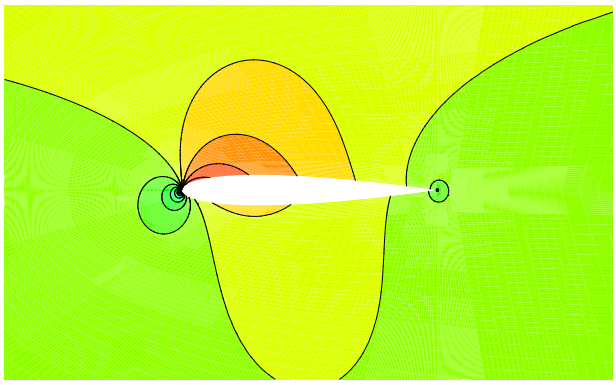

(b) Mach contours on the adapted mesh

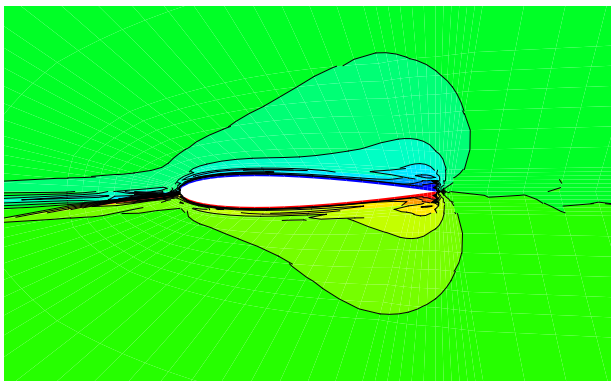

(c) C_L adjoint ψ_2 on the initial mesh

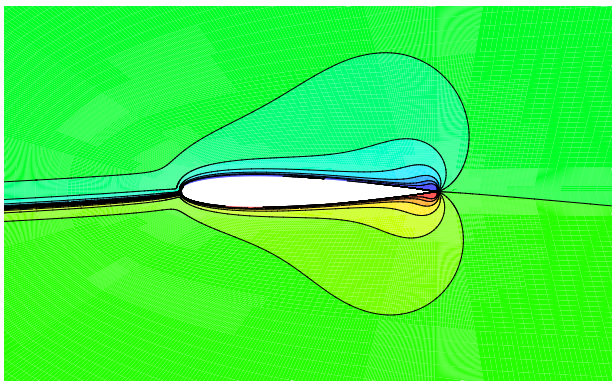

(d) C_L adjoint ψ_2 on the adapted mesh

Figure 6.5: Primal and adjoint solution of the adjoint-based h-adaptation for a inviscid NACA 0012 airfoil at $M_0 = 0.5,\ \alpha = 2^\circ$ $(k = 3)$.

The convergence histories of the lift and drag coefficients are shown in Figure 6.6. The corrected outputs are computed using the adjoint-based error estimates. The results show that the corrected coefficients converge much faster than the uncorrected ones, and all converge to the same value. The estimated error at the last adaptation stage is around 10^{-10}. So the C_L and C_D on the final adaptation stage are chosen as the truth value. Figure 6.7 shows the output error from the adaptation and the uniform refinements. An effective convergence rate of 6 is achieved for both C_L and C_D with h-adaptation. It is clear that the adjoint based

h-adaptation framework can reduce the computational cost by orders of magnitude in terms of the number of DOFs.

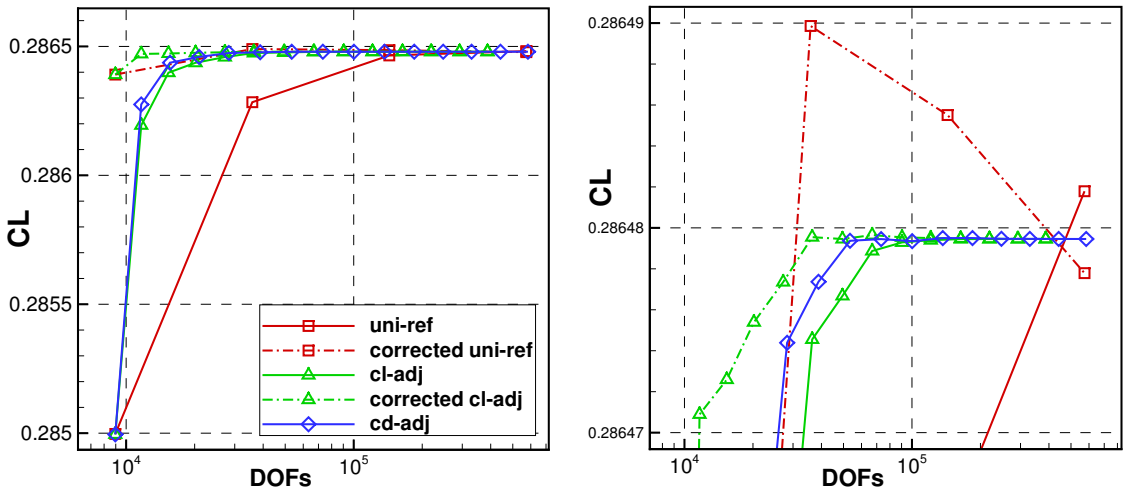

(a) C_L (b) C_L zoom in

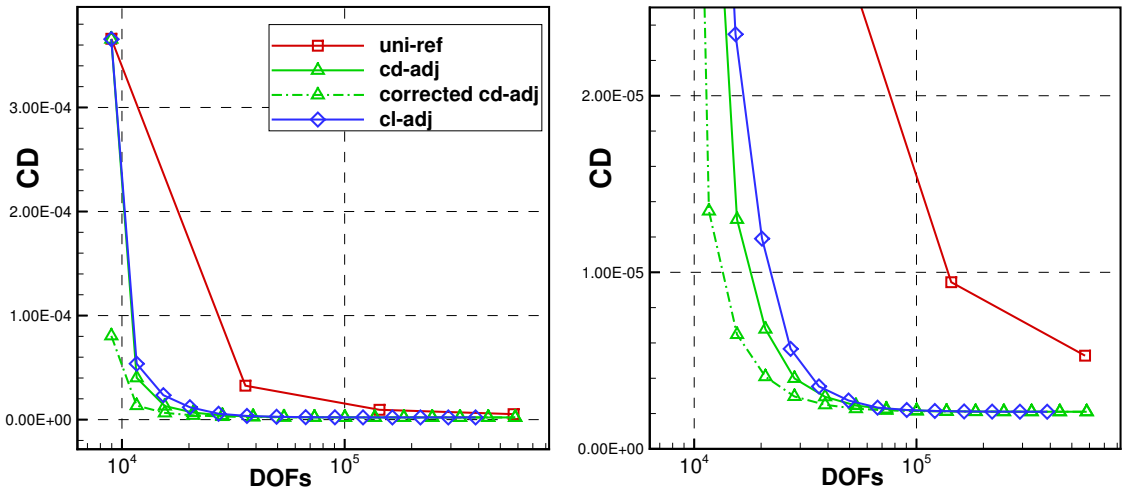

(c) C_D (d) C_D zoom in

Figure 6.6: C_L and C_D convergence of the adjoint-based h-adaptation for a NACA 0012 airfoil at $M_0 = 0.5,\ \alpha = 2^\circ$ $(k = 3)$.

Next, the performance of the h- and p-adaptations are compared on simplex meshes. The initial mesh is shown in 6.8. The adaptation starts from a 2^{nd} order CPR scheme, undergoes

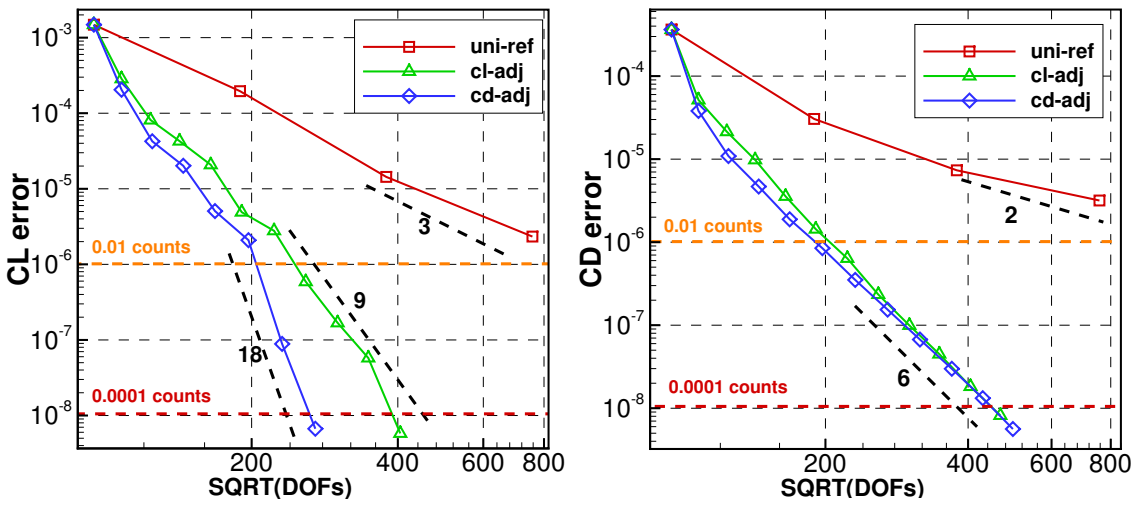

(a) C_L Error (b) C_D Error

Figure 6.7: C_L and C_D error of the adjoint-based h-adaptation for a NACA 0012 airfoil at $M_0 = 0.5,\ \alpha = 2^\circ\ (k = 3)$.

five levels of h-adaptation and p-adaptation separately with an adaptation fraction $f = 0.1$ on each stage. Both of the adjoint-based adaptation and the unweighted residual-based adaptation are tested. The drag coefficient and the lift coefficient are considered as the output of interest in this case.

The final adapted meshes and the order distributions are shown in Figure 6.11. The regions near the trailing edge and the leading edge are adapted consistently for all types of error indicators. However, only the drag adjoint-based adaptation targets the stagnation streamline to perform mesh refinements or solution order increments. This is due to the singularity of the drag adjoint solution along the stagnation streamlines. [39] Another different refinement regions between the output-based adaptation and the residual-based adaptation are the upper and lower surfaces of the airfoil. Intuitively, those areas are important for accurate prediction of the outputs related to the total force. Both of the adjoint-based adaptations with lift and drag coefficient as output correctly target those areas, whereas the residual-based adaptations leaves those region relatively coarse. In general, adjoint-based adaptations demonstrate the capability of capturing the error propagation effects inherent

in the Euler equations.

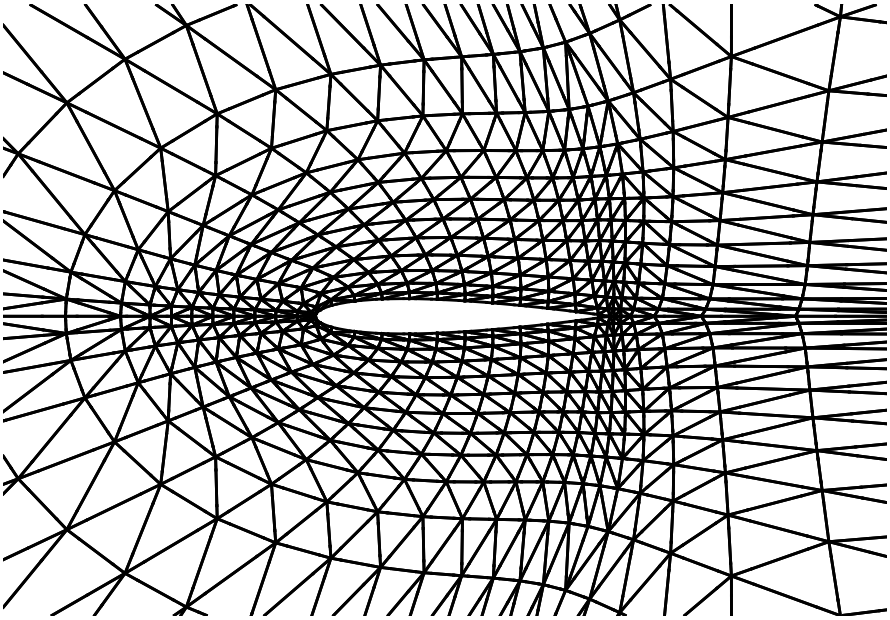

Figure 6.8: The initial $p2$ triangle mesh.

Figure 6.9 compares the lift coefficient error, the drag coefficient error and the entropy error of the different adaptation strategies. It is clear to see that the adaptive methods could produce much more efficient error reductions in terms of the DOFs. The adjoint-based adaptations with lift coefficient and drag coefficient as the output perform similarly, which are better than the residual-based adaptations. For this problem, the p-adaptation performs better than the h-adaptation due to the smoothness of the solution.

Further comparisons of the h-adaptations with different approximation orders are shown in Figure 6.10. It is well known that the solution discontinuities can affect the optimal order of accuracy for the high-order methods. Since there is a geometry singularity point at the

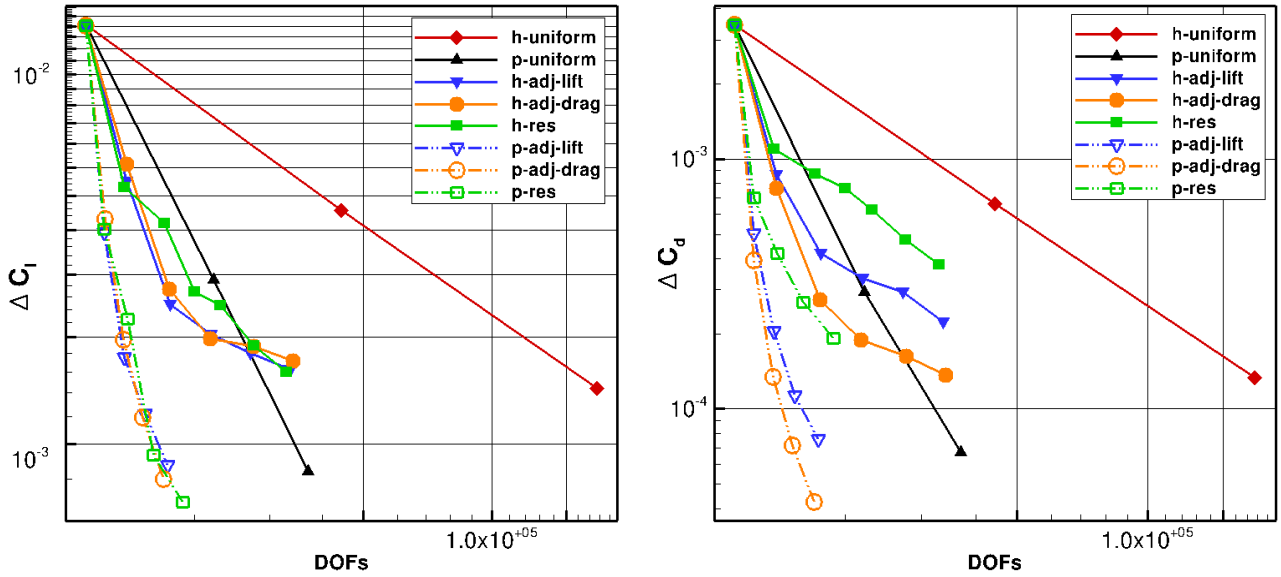

(a) The C_L error

(b) The C_D error

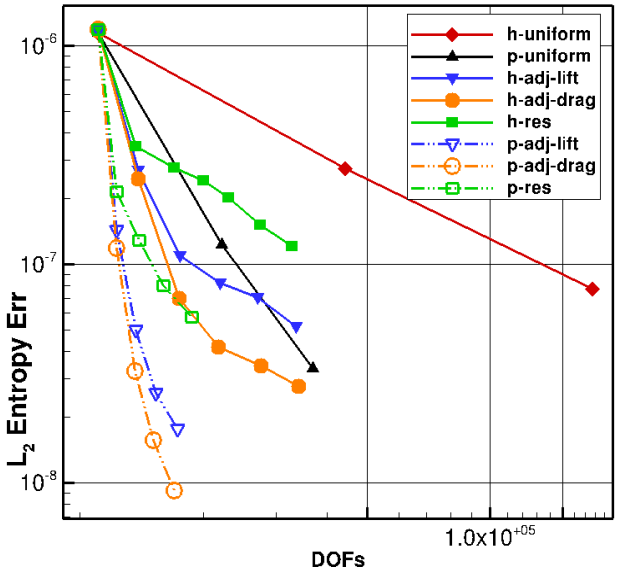

(c) The Entropy error

Figure 6.9: H- and p-adaptation for a NACA 0012 airfoil at $M_0 = 0.5,\ \alpha = 2^\circ$ $(k = 2)$.

trailing edge of the airfoil, the uniform mesh refinements cannot achieve the optimal convergence rate. The current results show that the h-adaptations successively refine the mesh around the trailing edge; therefore it could reduce the effect of this geometry singularity and reveal the potential accuracy from the high-order CPR method. As shown in the Figure 6.10, the accuracy per DOFs from the h-adaptations with 3^{rd} order schemes are much better than the h-adaptations with 2^{nd} order schemes, which demonstrates the benefits of performing h-adaptation with high-order approximations.

6.3 Laminar Flow over the Flat Plate

This case considers subsonic, laminar flow over a flat plate. The problem is solved on a rectangular domain of size $[-1.25, 1.0] \times [0, 2]$. The plate length is 1, which spanning from $x = 0.0$ to 1.0. The freestream Mach number is $M_0 = 0.5$, the Reynolds number based on the plate length is $Re = 10^6$, and the Prandtl number is set to be $Pr = 0.72$. The adiabatic no-slip wall boundary condition is enforced along the plate, and a symmetry boundary condition is specified on the first part of the lower boundary. Therefore, the leading edge of the plate is a singularity point between the symmetry boundary condition and the no-slip boundary condition. The focus of this problem is to test the ability of the current adaptation framework to generate anisotropic elements inside the boundary layer and to control the singularity effect from the leading edge.

The 4th order CPR scheme ($k = 3$) with the Gauss points as the SPs/FPs and the LP approach is used in the discretization. The truth $CD = 0.00131119952$ are from the 1st high-order CFD workshop. Here, the drag coefficient is chosen as the output of interest. The initial coarse mesh is shown in Figure 6.14a. Isotropic and anisotropic h-adaptions driven by the drag adjoint error estimate are tested. Figure 6.14 shows the adapted mesh

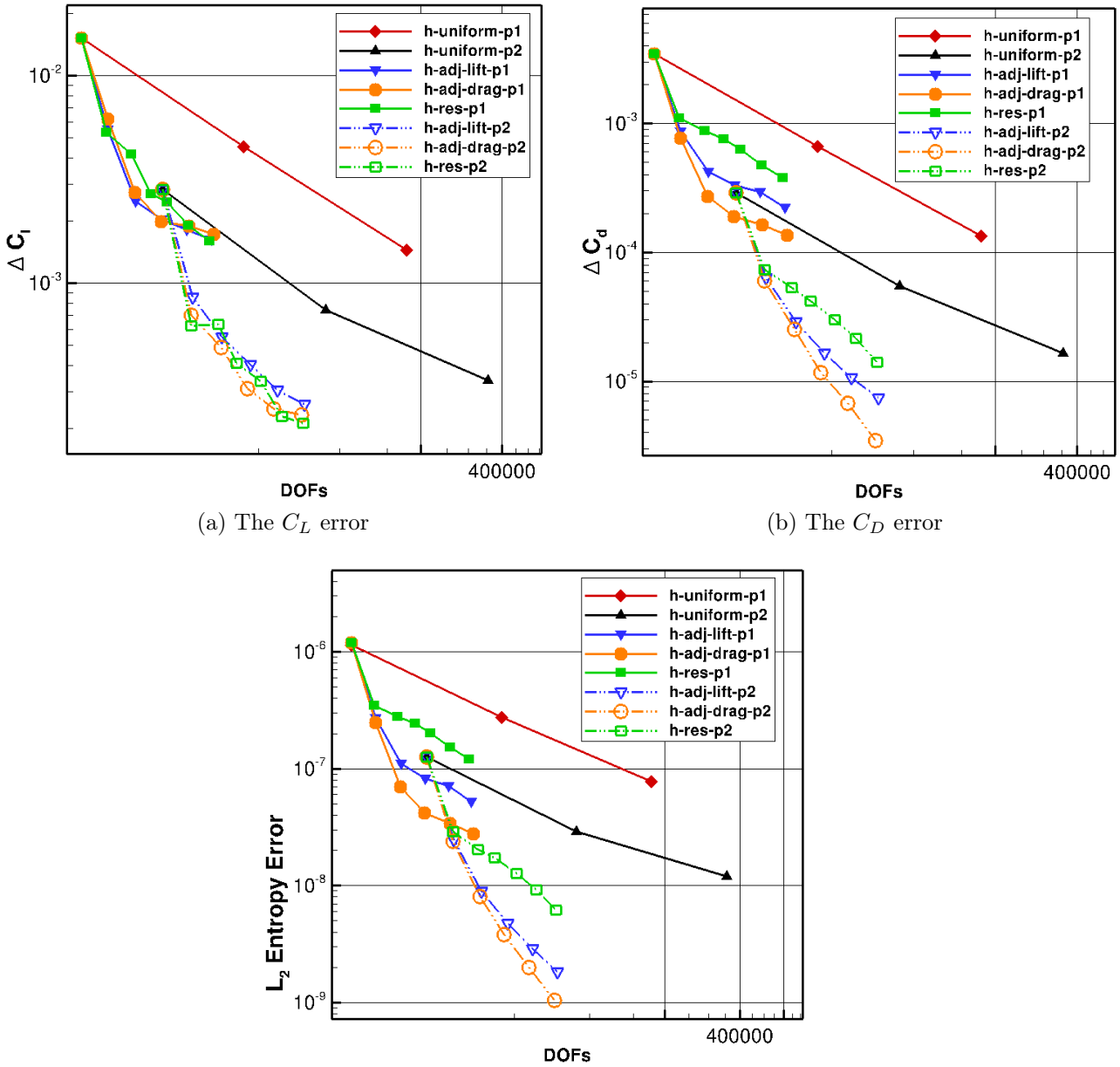

(a) The C_L error

(b) The C_D error

(c) The Entropy error

Figure 6.10: The results of h-adaptation with $k = 1$ and $k = 2$ for a NACA 0012 airfoil at $M_0 = 0.5,\ \alpha = 2°$.

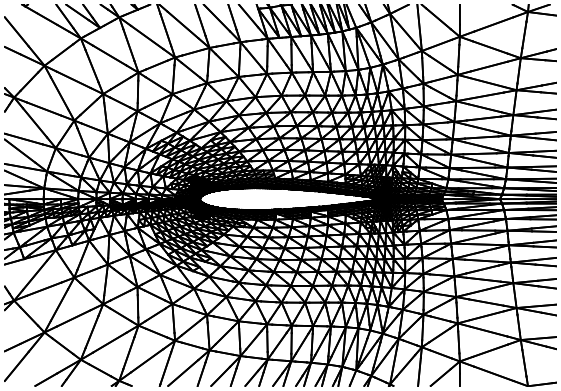

(a) H-adaptation with the lift adjoint

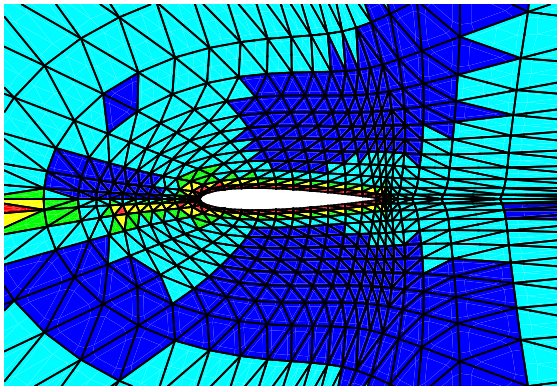

(b) P-adaptation with the lift adjoint

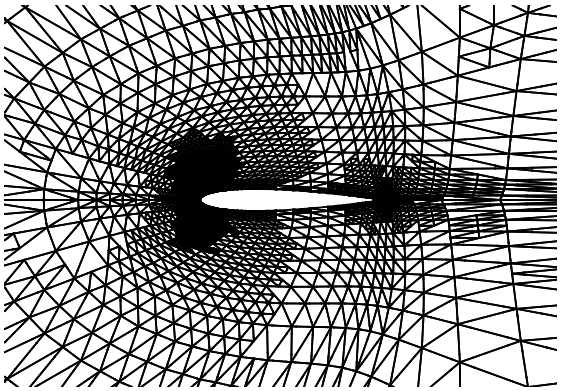

(c) H-adaptation with the drag adjoint

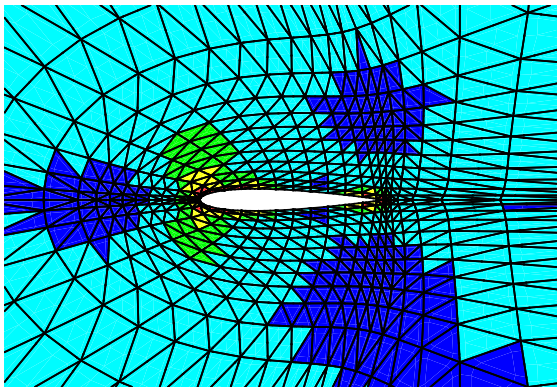

(d) P-adaptation with the drag adjoint

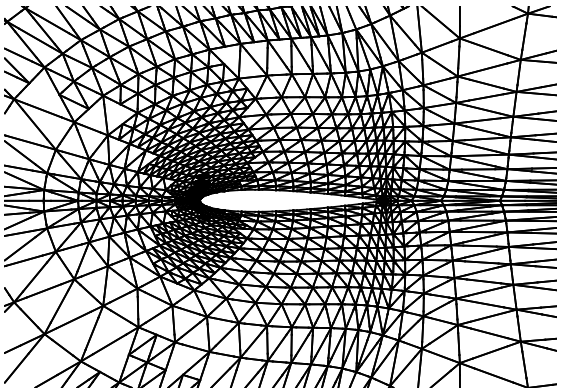

(e) H-adaptation with a residual-based indicator

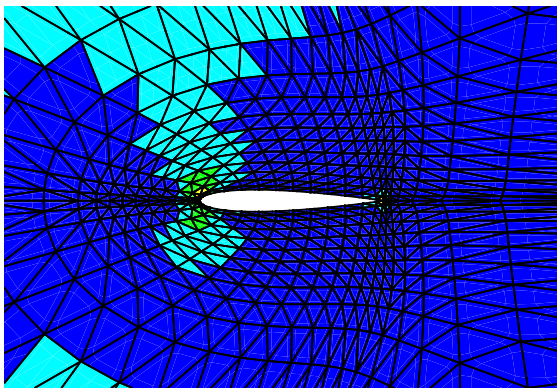

(f) P-adaptation with a residual-based indicator

Figure 6.11: 5 level adaptations for a NACA 0012 airfoil with $M_\infty = 0.5,\ \alpha = 2°$.

with different adaptation strategies. Mach contours are displayed in Figure 6.12.The leading edge and the elements around the lower boundary are refined repeatedly on each adaptation level. For anisotropic adaptation, the local output error estimates automatically considers the behaviors from the primal solution and the adjoint solution by the local error sampling procedure, which generates anisotropic elements in the boundary layer. The largest aspect ratio of the elements generated by the current anisotropic adaptation strategy for this case is around 1500 on the final adaptation stage. For the singularity point, both of the current anisotropic and isotropic adaptation try to refine around it isotropically to control its effect. Figure 6.13 shows the CD error for those adaptation strategies with the uniform refinement results. The convergence history shows that the anisotropic adaptation uses less degrees of freedom and produces smaller drag error than the isotropic adaptation. In addition, compared with the isotropic cells, the high aspect ratio elements generated by the anisotropic adaptation toward the boundary layer speeds up the convergence of the nonlinear solver dramatically.

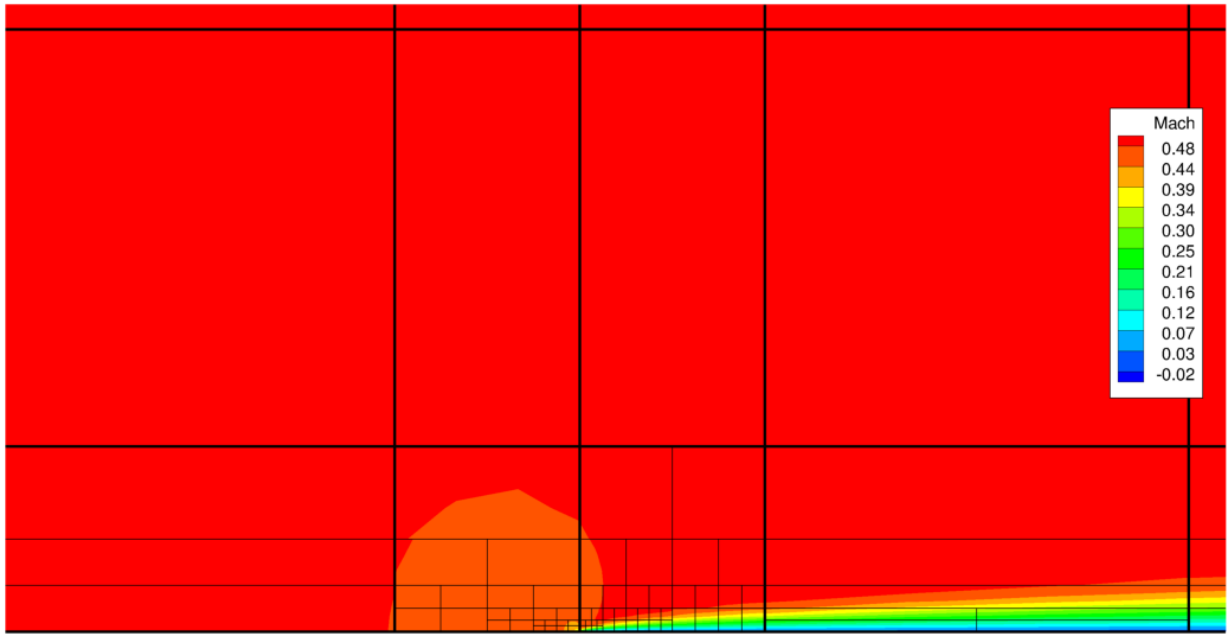

Figure 6.12: Mach number contours for the laminar flat plate problem on the adapted mesh at $M_0 = 0.5$, $Re = 10^6$.

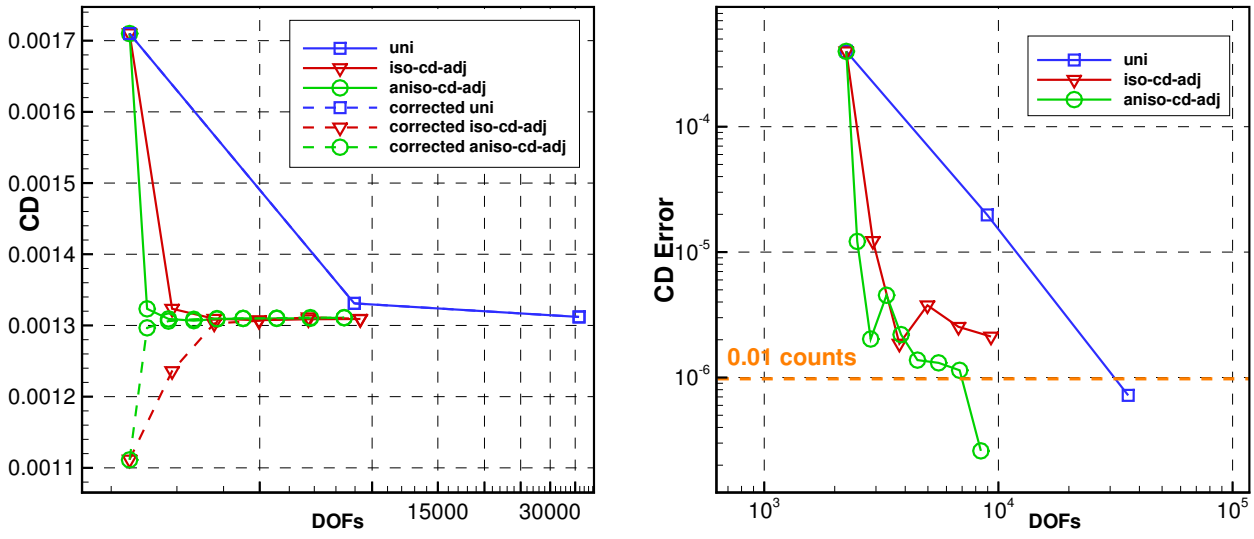

(a) CD

(b) CD

Figure 6.13: CD convergence for the laminar flat plate problem at $M_0 = 0.5, Re = 10^6$ ($k = 3$).

6.4 Laminar Flow over the NACA 0012 Airfoil

In this case, we consider subsonic laminar flow over a NACA 0012 airfoil at a free-stream $M_0 = 0.5$ and an angle of attack $\alpha = 1°$. The Reynolds number based on the chord length of the airfoil is $Re = 5000$. The same mesh for the inviscid NACA 0012 airfoil test case are used. The drag coefficient and the lift coefficient are considered as the outputs of interest. Adjoint-based isotropic and anisotropic adaptations are driven by the output-based error indicator. Additionally, uniform h-refinement is performed to compare those adaptation strategies. The 4^{th} order CPR scheme ($k = 3$) with the Gauss points as the SPs/FPs and the LP approach is used in the discretization. All adaptations start from a mesh of 560 $p4$ quadrilateral elements.

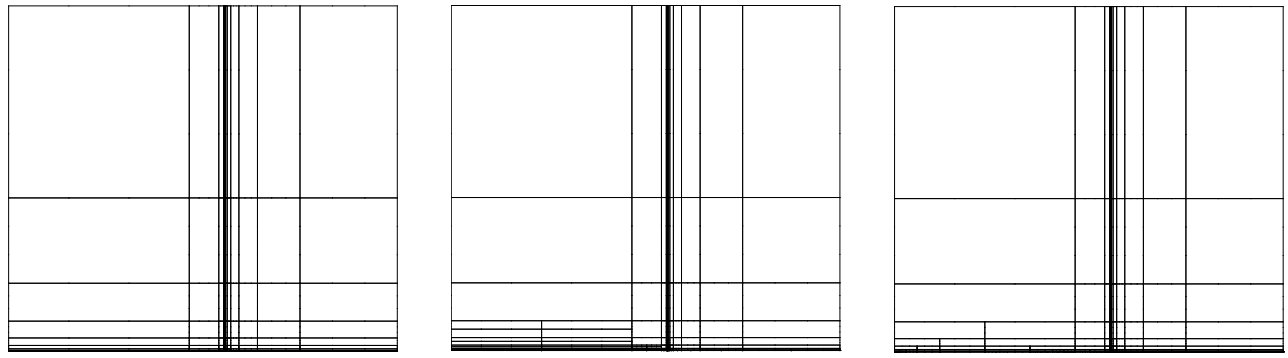

(a) The initial mesh (b) Isotropic adapted mesh (c) Anisotropic adapted mesh

(d) Zoom in, initial mesh

(e) Zoom in, isotropic adapted mesh

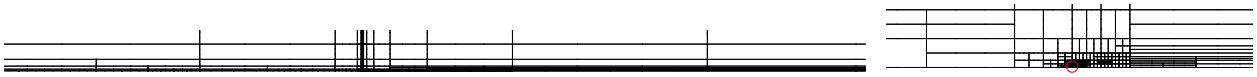

(f) Zoom in, initial mesh

Figure 6.14: Isotropic and anisotropic adapted mesh for the laminar flat plate problem at $M_0 = 0.5, Re = 10^6$. Red circle indicates the leading edge ($k = 3$).

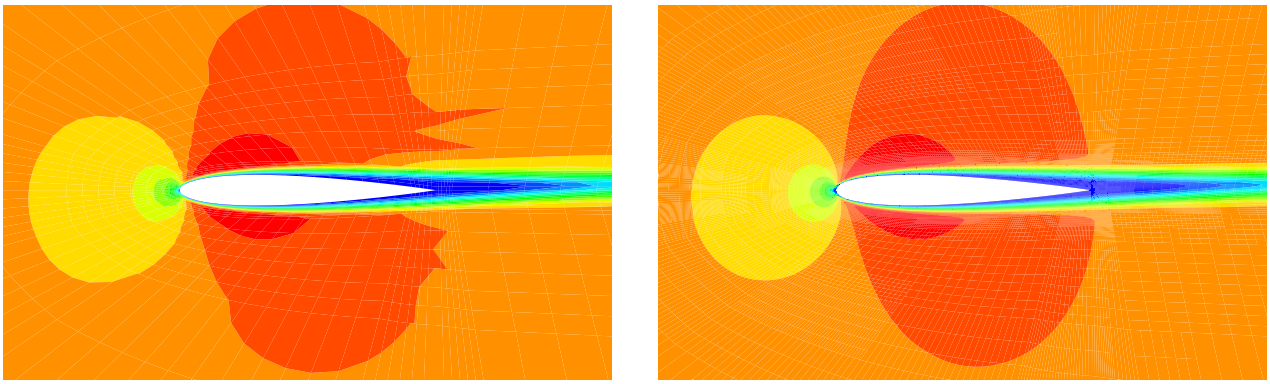

(a) Mach contours on the initial mesh

(b) Mach contours on the adapted mesh

Figure 6.15: Mach contours for a NACA 0012 airfoil at $M_0 = 0.5,\ \alpha = 1°, Re = 5000$ ($k = 3$).

Figure 6.15 and Figure 6.16 compare the Mach contours on the initial mesh and adapted mesh and presents the adapted meshes from the tested adaptation strategies. Some common regions like stagnation lines and boundary layer are targeted for refinements by both of isotropic and anisotropic adaptations. The trailing edge is isotropically refined repeatedly to reduce its singularity effect, see Figure 6.18. At this Reynolds number, the flow field generate a very thin boundary layer, which indicates the anisotropic adaptation should be much more efficient than the isotropic one. The adapted mesh shows that the local solve procedure correctly detects the anisotropic behavior of the flow and produces the required anisotropic elements in the boundary layer (Figure 6.18).

Figure 6.17 shows the lift coefficient and drag coefficient convergence with corresponding corrected values by adjoint-based error estimates, in terms of number of degrees of freedom. Results show that both of the lift coefficient and the drag coefficient, from all of those adaptation strategies, try to converge to the same value. The corrected outputs by the error estimates converge faster than the uncorrected ones. Therefore, the truth outputs are chosen from those output-based isotropic h-adaptive simulations, whose estimate error is less than

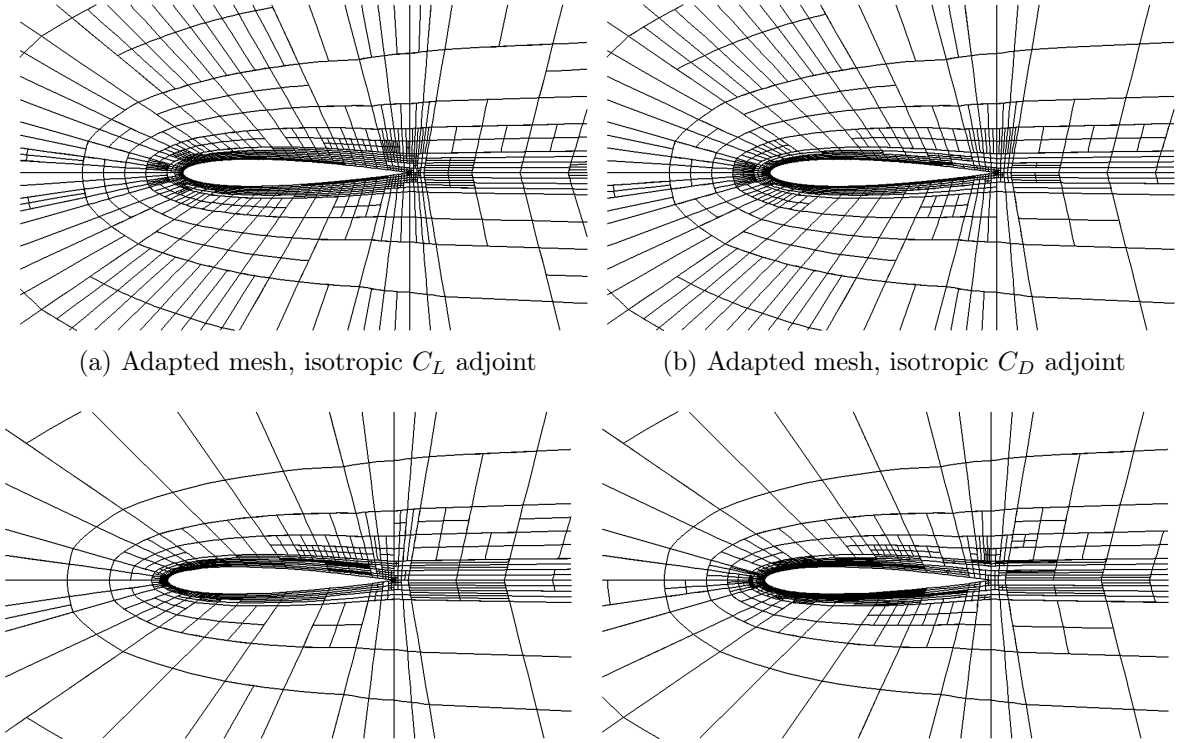

(a) Adapted mesh, isotropic C_L adjoint

(b) Adapted mesh, isotropic C_D adjoint

(c) Adapted mesh, anisotropic C_L adjoint

(d) Adapted mesh, anisotropic C_D adjoint

Figure 6.16: Adjoint-based h-adapted mesh for a NACA 0012 airfoil at $M_0 = 0.5$, $\alpha = 1°, Re = 5000$ $(k = 3)$.

10^{-8} on the final stage. Figure 6.19 shows the CL and CD error of all tested adaptation strategies with results from the uniform h-refinements. Anisotropic adaptations converge much faster than the isotropic ones. It uses less degrees of freedom and produces smaller output error. A significant saving in the number of DOFs is observed when it comes to the lift coefficient. The results shows that the isotropic adaptation can waste some degree of freedom in the direction which does not changes too much from a byproduct of the refinement in the other direction.

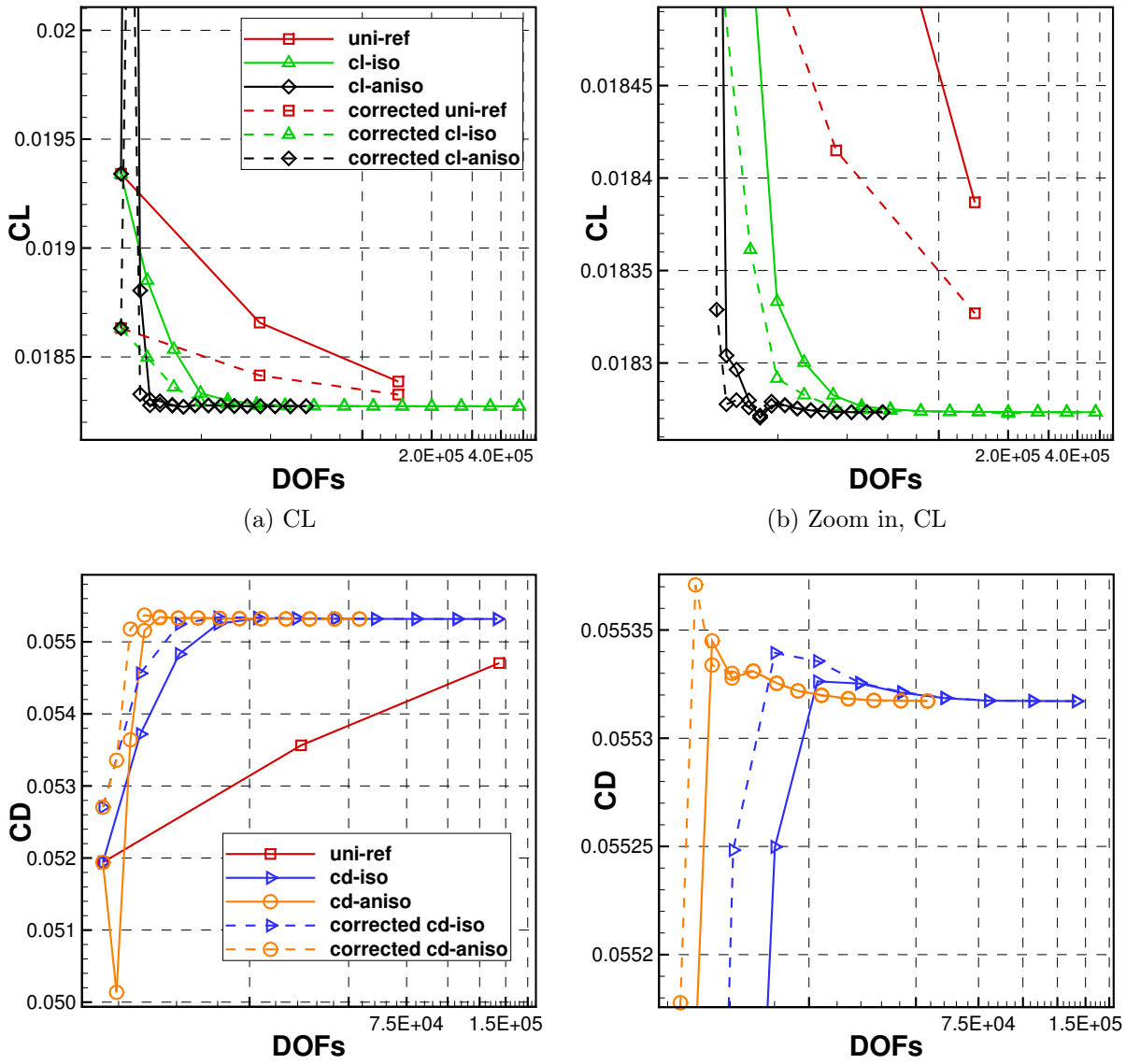

(a) CL

(b) Zoom in, CL

(c) CD

(d) Zoom in, CD

Figure 6.17: CL and CD convergence for a NACA 0012 airfoil at $M_0 = 0.5,\ \alpha = 1°, Re = 5000$ $(k = 3)$.

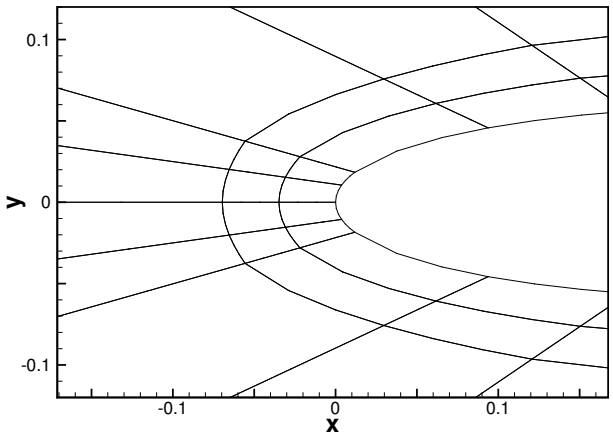

(a) Initial mesh near the leading edge

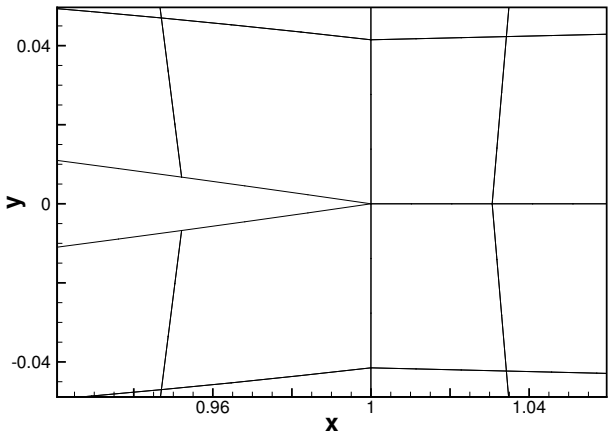

(b) Initial mesh near the trailing edge

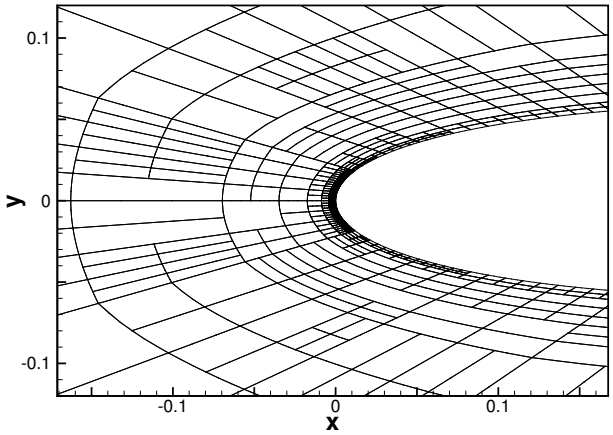

(c) Adapted mesh near the leading edge, iso

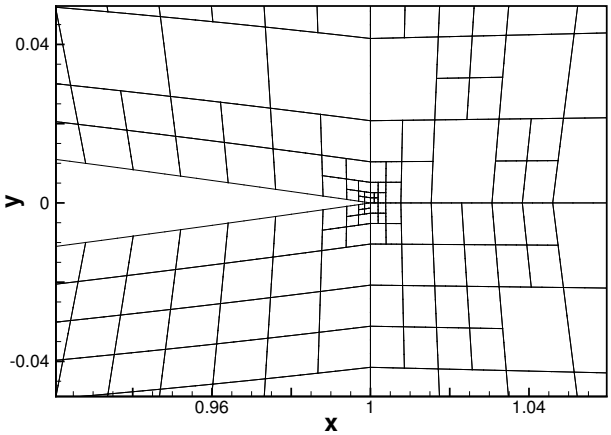

(d) Adapted mesh near the trailing edge, iso

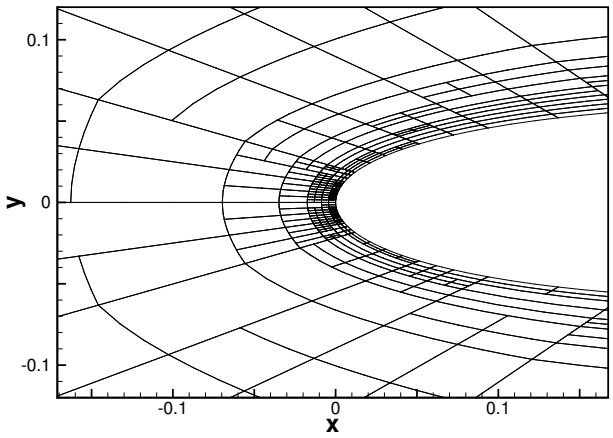

(e) Adapted mesh near the leading edge, aniso.

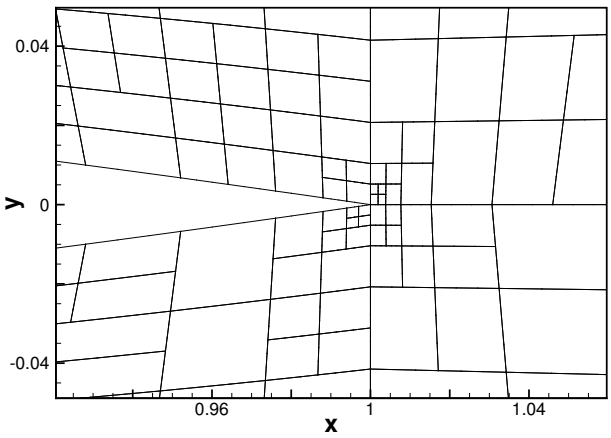

(f) Adapted mesh near the trailing edge, aniso.

Figure 6.18: Detailed adapted mesh with C_L adjoint for a NACA 0012 airfoil at $M_0 = 0.5,\ \alpha = 1°, Re = 5000$ $(k = 3)$.

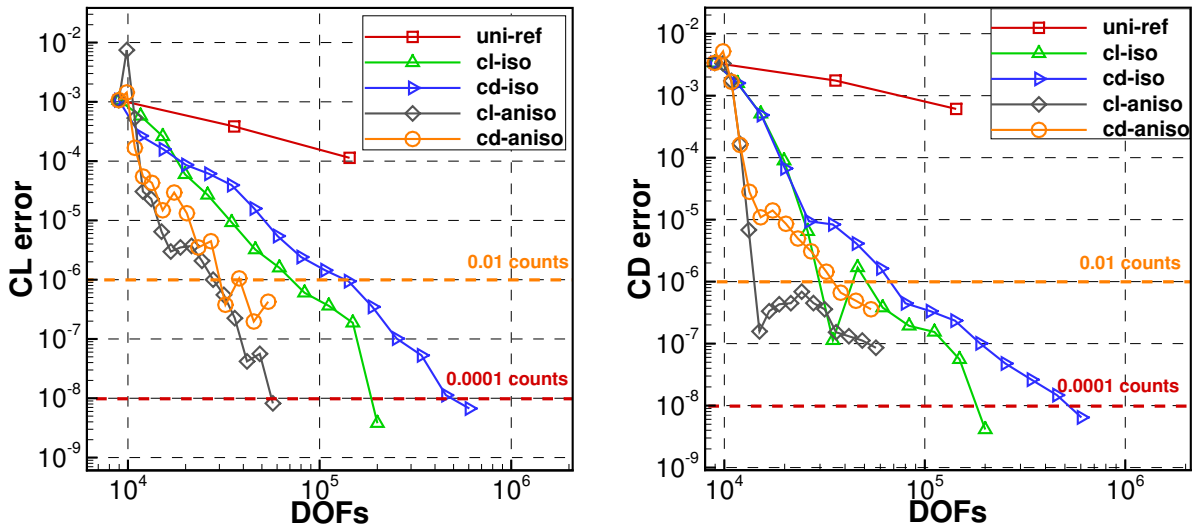

(a) CL error

(b) CD error

Figure 6.19: CL and CD error for a NACA 0012 airfoil at $M_0 = 0.5$, $\alpha = 1°, Re = 5000$ ($k = 3$).

6.5 Inviscid Flow over a Sphere

The current adjoint-based error estimation and adaptation method is extended to 3D. Here, we consider subsonic inviscid flow over a sphere of radius 1. The p3 hexahedral mesh is used for this simulation. Figure 6.21 shows the outline of the computational domain and the initial surface mesh on the sphere. The initial mesh contains a total of 480 p3 hexahedral elements. The 3^{rd} order CPR scheme with the Gauss points as the SPs/FPs and the LP approach is used. The inflow Mach number is set to be 0.3 with an angle of attack $\alpha = 2°$.

The adaptation is driven by the adjoint-based error indicator with drag as the output of interest. On each adaptation level, 10% of the current elements with the largest error are marked to be refined. The adapted mesh and the Mach contours on each adaptation level are shown in Figure 6.20. Regions around the sphere surface are refined persistently. Figure

6.22 compares the drag coefficient error of the adaptation with the result from the uniform h-refinements. It is clear to see that the current adaptive method could produce much more efficient error reductions in terms of the number of the DOFs. An convergence order of 6 is obtained through the adaptation, which is much faster than the uniform refinements, whose order of accuracy is around 2. This preliminary adaptation results demonstrates the effectiveness of the current adaptive method for a 3D problem.

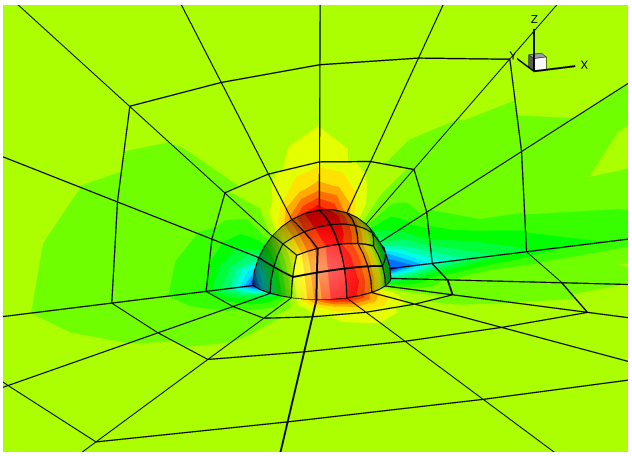

(a) Adaptation level 1

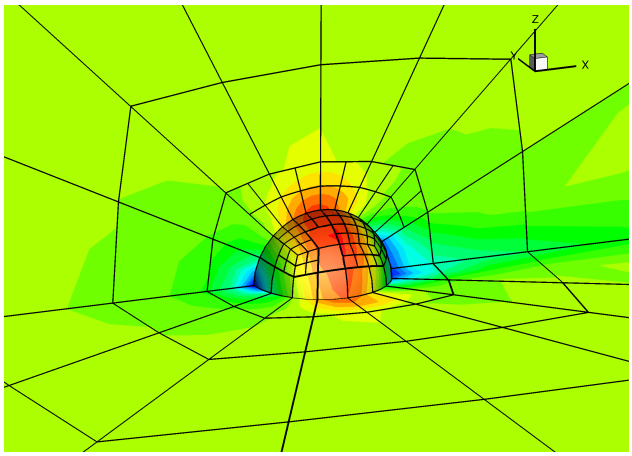

(b) Adaptation level 2

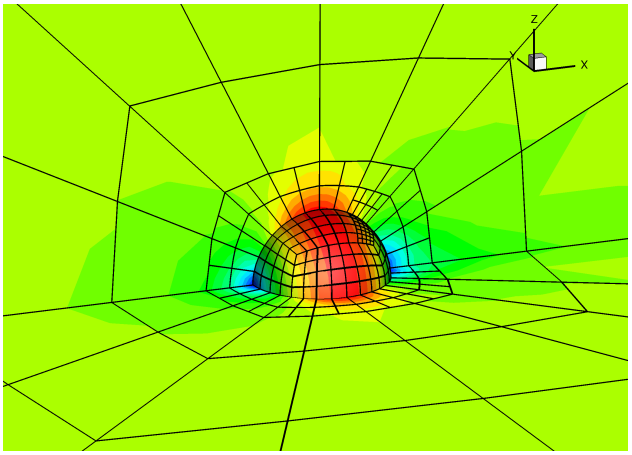

(c) Adaptation level 3

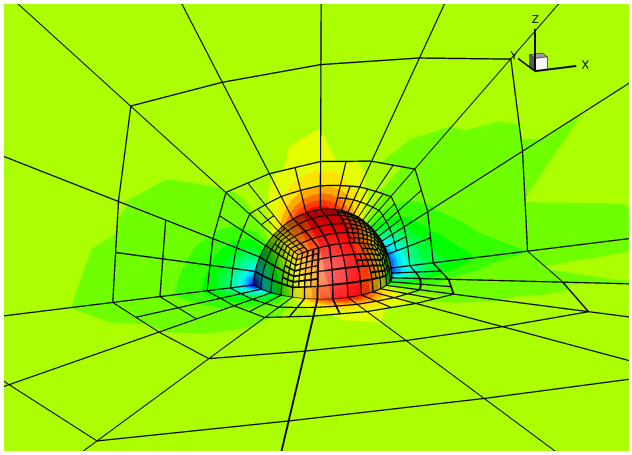

(d) Adaptation level 4

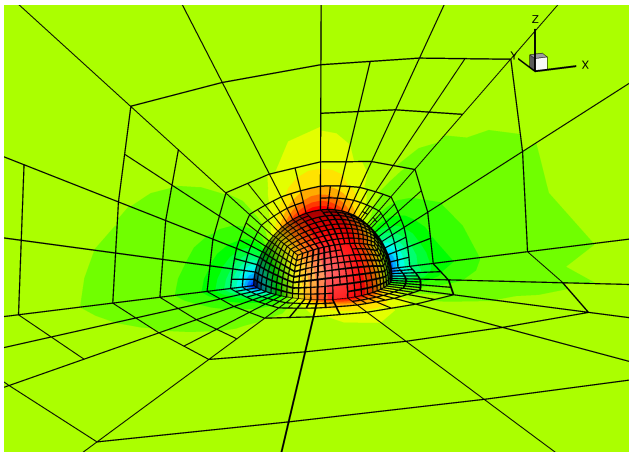

(e) Adaptation level 5

Figure 6.20: Mach contours on the adapted mesh for the inviscid flow over a sphere at $M_0 = 0.3$, $\alpha = 2^\circ$ ($k = 2$).

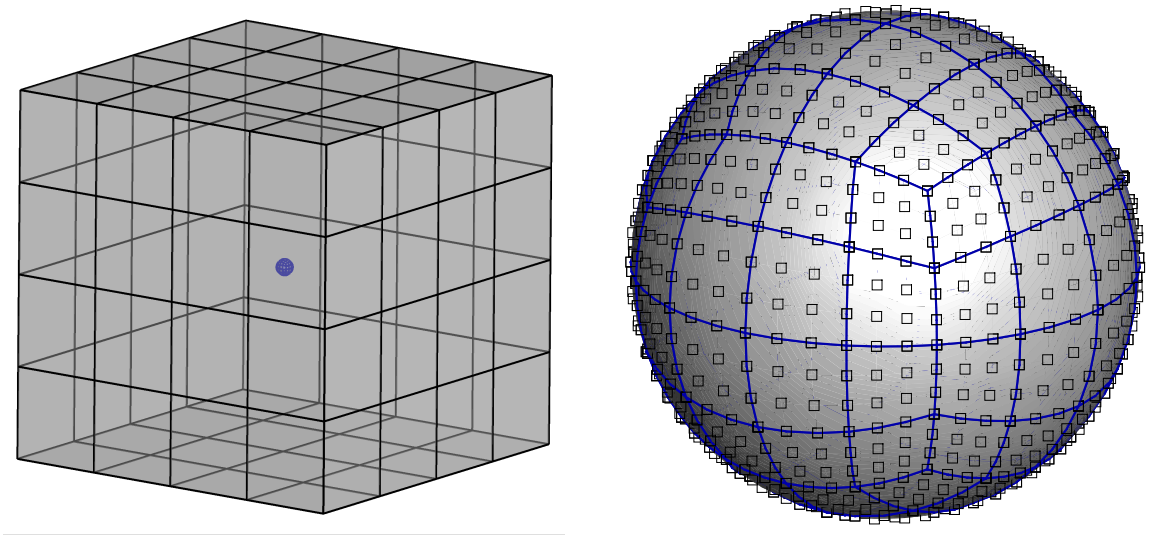

Figure 6.21: The initial $p3$ curved hexahedral mesh for the inviscid flow over a sphere problem.

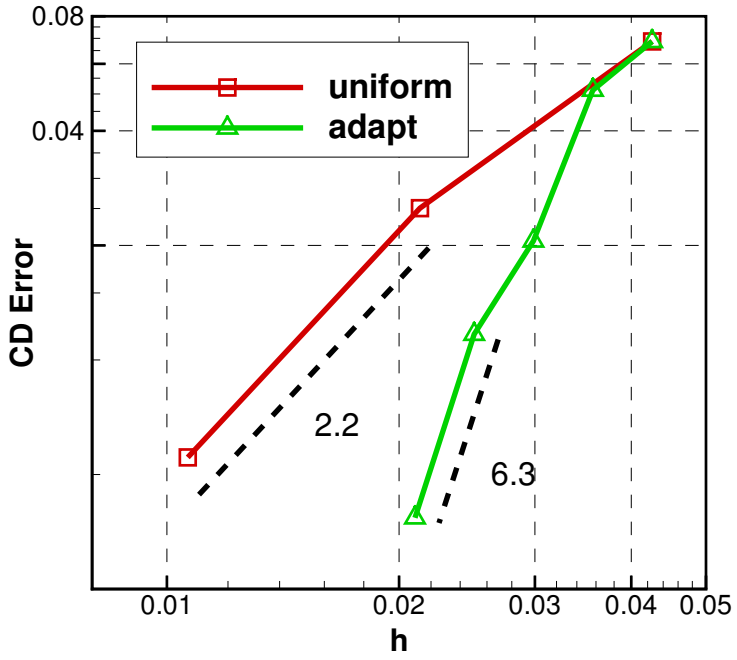

Figure 6.22: CD errors of the inviscid flow over the sphere at $M_0 = 0.3$, $\alpha = 2°(k = 2)$.

Chapter 7

Conclusions and Future Work

7.1 Summary and Conclusions

This thesis presents a robust and efficient adjoint-based adaptive high-order differential formulation for the compressible Navier-Stokes equations, which can rapidly determine accurate estimates of engineering outputs within a prescribed error threshold.

In the process, we developed a $P_N P_M - CPR$ framework for the hyperbolic conservation laws. The formulation is an extension of $P_N P_M$ method to the CPR framework. It is a hybrid finite volume and discontinuous Galerkin method, in which neighboring cells are used to build a higher order polynomial than the solution representation in the cell under consideration. We presented several $P_N P_M$ schemes under the CPR framework. Many interesting schemes with various orders of accuracy and efficiency are developed. The dispersion and dissipation properties of those methods are investigated through a Fourier analysis, which shows that the $P_N P_M - CPR$ method is dependent on the position of the solution points. Optimal solution points for 1D $P_N P_M - CPR$ schemes which can produce expected order of accuracy are identified. In addition, the $P_N P_M - CPR$ method is extended to solve the Navier-Stokes equations.

To estimate the error of an engineering output, we extended the dual-weighted residual

method originally developed in the variational framework to the high-order CPR method which is in the differential form. A dual-consistent CPR formulation of hyperbolic conservation laws is developed and its dual consistency is analyzed. Super-convergent functional and error estimate for the output with the CPR method are obtained. Factors affecting the dual consistency, such as the solution point distribution, correction functions, boundary conditions and the discretization approach for the non-linear flux divergence term, are studied.

Next, we developed a parallel adjoint-based adaptive CPR solver with the capability of handling any element-based error estimate and arbitrary discretization orders for mixed grids. For anisotropic h-adaptations, we use a local output error sampling procedure to find the optimal refinement option. The current method have been applied to aerodynamic flows and challenging engineering applications. Numerical tests show that significant savings in the number of DOFs can be achieved through the adjoint-based adaptation.

7.2 Future Work

Several potential areas of future work are identified during the course of this work:

1. Extend the current adjoint-based adaptation method to unsteady problems.

2. Consider the refinement and coarsening at the same adaptation stage.

3. Adapt the location of the grid node position by obtaining an adjoint solution for the grid points.

4. Extend the current adaptation method to the RANS solver for turbulent flows.

5. Use more general geometry representation, e.g., a CAD geometry kernel, to enforce the geometry constraint after the mesh adaptation.

References

[1] M. Ainsworth and J.T. Oden. A unified approach to a posteriori error estimation using element residual methods. *Numerische Mathematik*, 65(1):23–50, 1993.

[2] Timothy J. Baker. Mesh adaptation strategies for problems in fluid dynamics. *Finite Elements in Analysis and Design*, 25(3-4):243–273, 1997.

[3] T.J. Barth and P.O. Frederickson. Higher order solution of the euler equations on unstructured grids using quadratic reconstruction. *AIAA paper 1990-0013*, 1990.

[4] T.J. Barth. Numerical methods for gasdynamic systems on unstructured meshes. *An Introduction to Recent Developments in Theory and Numerics for Conservation Laws*, 5:195–285, 1998.

[5] F. Bassi and S. Rebay. A high-order accurate discontinuous finite element method for the numerical solution of the compressible navier–stokes equations. *Journal of Computational Physics*, 131(2):267–279, 1997.

[6] F. Bassi and S. Rebay. High-order accurate discontinuous finite element solution of the 2d euler equations. *Journal of Computational Physics*, 138(2):251–285, 1997.

[7] F. Bassi and S. Rebay. Gmres discontinuous galerkin solution of the compressible navier-stokes equations. *Lecture Notes in Computational Science and Engineering*, 11:197–208, 2000.

[8] C.E. Baumann and J.T. Oden. A discontinuous hp finite element method for the euler and navier–stokes equations. *International Journal for Numerical Methods in Fluids*, 31(1):79–95, 1999.

[9] Roland Becker and Rolf Rannacher. A feed-back approach to error control in finite element methods: Basic analysis and examples. *East-West J. Numer. Math*, 4:237–264, 1996.

[10] Roland Becker and Rolf Rannacher. An optimal control approach to a posteriori error estimation in finite element methods. *Acta Numerica*, 10:1–102, 2001.

[11] Jens Berg and Jan NordstrÃ¶m. Duality based boundary conditions and dual consistent finite difference discretizations of the navier-stokes and euler equations. *Journal of Computational Physics*, 259(0):135 – 153, 2014.

[12] M.J. Berger and P. Colella. Local adaptive mesh refinement for shock hydrodynamics. *Journal of computational Physics*, 82(1):64–84, 1989.

[13] Nick Burgess. *An Adaptive Discontinuous Galerkin Solver for Aerodynamic Flows*. PhD thesis, University of Wyoming, 2011.

[14] J.S. Cagnone and S.K. Nadarajah. A stable interface element scheme for the p-adaptive lifting collocation penalty formulation. *Journal of Computational Physics*, 231(4):1615 – 1634, 2012.

[15] J.S. Cagnone, B.C. Vermeire, and S. Nadarajah. A p-adaptive {LCP} formulation for the compressible navier-stokes equations. *Journal of Computational Physics*, 233(0):324 – 338, 2013.

[16] P. Castonguay, P. E. Vincent, and A. Jameson. A new class of high-order energy stable flux reconstruction schemes for triangular elements. *J. Sci. Comput.*, 51(1):224–256, April 2012.

[17] P. Castonguay, D.M. Williams, P.E. Vincent, and A. Jameson. Energy stable flux reconstruction schemes for advection-diffusion problems. *Computer Methods in Applied Mechanics and Engineering*, 267(0):400 – 417, 2013.

[18] M. J. Castro-Diaz, F. Hecht, B. Mohammadi, and O. Pironneau. Anisotropic unstructured mesh adaption for flow simulations. *International Journal for Numerical Methods in Fluids*, 25(4):475–491, 1997.

[19] Marco Ceze and Krzysztof J Fidkowski. Anisotropic hp-adaptation framework for functional prediction. *AIAA Journal*, 51(2):492–509, 2012.

[20] B. Cockburn and C.W. Shu. The local discontinuous galerkin method for time-dependent convection-diffusion systems. *SIAM Journal on Numerical Analysis*, pages 2440–2463, 1998.

[21] B. Cockburn and C.W. Shu. The runge–kutta discontinuous galerkin method for conservation laws v: multidimensional systems. *Journal of Computational Physics*, 141(2):199–224, 1998.

[22] B. Cockburn, S.Y. Lin, and C.W. Shu. Tvb runge-kutta local projection discontinuous galerkin finite element method for conservation laws iii: one-dimensional systems. *Journal of Computational Physics*, 84(1):90–113, 1989.

[23] P. Devloo, J. Tinsley Oden, and P. Pattani. An hp adaptive finite element method for the numerical simulation of compressible flow. *Computer methods in applied mechanics and engineering*, 70(2):203–235, 1988.

[24] J. Dompierre, M.G. Vallet, Y. Bourgault, M. Fortin, and W.G. Habashi. Anisotropic mesh adaptation: towards user-independent, mesh-independent and solver-independent cfd. part iii. unstructured meshes. *International journal for numerical methods in fluids*, 39(8):675–702, 2002.

[25] M. Dumbser, D.S. Balsara, E.F. Toro, and C.D. Munz. A unified framework for the construction of one-step finite volume and discontinuous galerkin schemes on unstructured meshes. *Journal of Computational Physics*, 227(18):8209–8253, 2008.

[26] M. Dumbser. Pnpm schemes on unstructured meshes for time-dependent partial differential equations. *Adaptive High-Order Methods in Computational Fluid Dynamics*, 2:203, 2011.

[27] J.A. Ekaterinaris. High-order accurate, low numerical diffusion methods for aerodynamics. *Progress in Aerospace Sciences*, 41(3-4):192–300, 2005.

[28] K.J. Fidkowski and D.L. Darmofal. A triangular cut-cell adaptive method for high-order discretizations of the compressible navier-stokes equations. *Journal of Computational Physics*, 225(2):1653–1672, 2007.

[29] KJ Fidkowski and PL Roe. Entropy-based mesh refinement, i: The entropy adjoint approach, 2009.

[30] K.J. Fidkowski and P.L. Roe. An entropy adjoint approach to mesh refinement. *SIAM Journal on Scientific Computing*, 32(3):1261–1287, 2010.

[31] K.J. Fidkowski. *A High-Order Discontinuous Galerkin Multigrid Solver for Aerodynamic Applications*. PhD thesis, Massachusetts Institute of Technology, 2004.

[32] Krzysztof Fidkowski. Review of output-based error estimation and mesh adaptation in computational fluid dynamics. *AIAA Journal*, 49(4):673–694, 2011.

[33] Luca Formaggia, Stefano Micheletti, and Simona Perotto. Anisotropic mesh adaptation in computational fluid dynamics: Application to the advection-diffusion-reaction and the stokes problems. *Applied Numerical Mathematics*, 51(4):511 – 533, 2004. Applied Scientific Computing: Advances in Grid Generatuion, Approximation and Numerical Modeling.

[34] H. Gao and Z. J. Wang. A residual-based procedure for hp-adaptation on 2d hybrid meshes. *AIAA Paper 2011-492*, 2011.

[35] H. Gao and Z. J. Wang. A conservative correction procedure via reconstruction formulation with the chain-rule divergence evaluation. *Journal of Computational Physics*, 232:7–13, January 2013.

[36] H. Gao and Z. J. Wang. Differential formulation of discontinuous galerkin and related methods for the navier-stokes equation. *Commun. Comput. Phys.*, 13:1013–1044, 2013.

[37] G.J. Gassner, F. Lörcher, C.D. Munz, and J.S. Hesthaven. Polymorphic nodal elements and their application in discontinuous galerkin methods. *Journal of Computational Physics*, 228(5):1573–1590, 2009.

[38] Emmanuil H. Georgoulis, Edward Hall, and Paul Houston. Discontinuous galerkin methods on hp-anisotropic meshes ii: a posteriori error analysis and adaptivity. *Appl. Numer. Math.*, 59(9):2179–2194, September 2009.

[39] M.B. Giles and N.A. Pierce. Adjoint equations in cfd: duality, boundary conditions and solution behaviour. *AIAA paper 97-1850*, 1997.

[40] M. Giles and N.A. Pierce. Adjoint error correction for integral outputs. 2001.

[41] T. Haga, H. Gao, and Z. J. Wang. A high-order unifying discontinuous formulation for the navier-stokes equations on 3d mixed grids. *Mathematical Modelling of Natural Phenomena*, 6:28–56, 2011.

[42] R.E. Harris and Z. J. Wang. High-order adaptive quadrature-free spectral volume method on unstructured grids. *Computers & Fluids*, 38(10):2006–2025, 2009.

[43] Ralf Hartmann and Paul Houston. Adaptive discontinuous galerkin finite element methods for the compressible euler equations. *Journal of Computational Physics*, 183(2):508 – 532, 2002.

[44] Ralf Hartmann. Adjoint consistency analysis of discontinuous Galerkin discretizations. *SIAM J. Numer. Anal.*, 45(6):2671–2696, 2007.

[45] J.S. Hesthaven and T. Warburton. *Nodal discontinuous Galerkin methods: algorithms, analysis, and applications*, volume 54. Springer-Verlag New York Inc, 2008.

[46] J.E. Hicken and D.W. Zingg. Summation-by-parts operators and high-order quadrature. *Journal of Computational and Applied Mathematics*, 237(1):111 – 125, 2013.

[47] J.E. Hicken. Output error estimation for summation-by-parts finite-difference schemes. *Journal of Computational Physics*, 231(9):3828 – 3848, 2012.

[48] Paul Houston and Endre Süli. hp-adaptive discontinuous galerkin finite element methods for first-order hyperbolic problems. *SIAM Journal on Scientific Computing*, 23(4):1226–1252, 2001.

[49] Weizhang Huang and Robert D Russell. *Adaptive moving mesh methods*, volume 174. Springer, 2010.

[50] Z. J. Wang Huynh, H. T. and P. E. Vincent. High-order methods for computational fluid dynamics: A brief review of compact differential formulations on unstructured grids. *Computers & Fluids*, 98(0):209–220, 2014.

[51] H. T. Huynh. A flux reconstruction approach to high-order schemes including discontinuous galerkin methods. Aiaa paper 2007-4079, 2007.

[52] H. T. Huynh. A reconstruction approach to high-order schemes including discontinuous galerkin for diffusion. Aiaa paper 2009-403, 2009.

[53] H. T. Huynh. High-order methods by correction procedures using reconstructions. *Adaptive High-Order Methods in Computational Fluid Dynamics*, 2:391, 2011.

[54] A. Jameson, P. E. Vincent, and P. Castonguay. On the non-linear stability of flux reconstruction schemes. *J. Sci. Comput.*, 50(2):434–445, February 2012.

[55] C. Johnson. Adaptive finite element methods for conservation laws. *Advanced numerical approximation of nonlinear hyperbolic equations*, pages 269–323, 1998.

[56] F. Palacios K. Duraisamy, J. J. Alonso and P. Chandrashekar. Error estimation for high speed flows using continuous and discrete adjoints. Aiaa paper 2010–128, 2010.

[57] Miyaji K. On the compressible flow simulations with shocks by a flux reconstruction approach. *AIAA Paper 2011-3057*, 2011.

[58] G. Karniadakis and S.J. Sherwin. *Spectral/hp element methods for CFD*. Oxford University Press, USA, 1999.

[59] D.A. Kopriva and J.H. Kolias. A conservative staggered-grid chebyshev multidomain method for compressible flows. *Journal of computational physics*, 125(1):244–261, 1996.

[60] David A. Kopriva. A conservative staggered-grid chebyshev multidomain method for compressible flows. ii. a semi-structured method. *Journal of Computational Physics*, 128(2):475 – 488, 1996.

[61] B. Van Leer. Towards the ultimate conservative difference scheme v. a second order sequel to godunov's method. *J. Comput. Phys.*, 32:101–136, 1979.

[62] Tobias Leicht and Ralf Hartmann. Anisotropic mesh refinement for discontinuous galerkin methods in two-dimensional aerodynamic flow simulations. *International Journal for Numerical Methods in Fluids*, 56(11):2111–2138, 2008.

[63] Tobias Leicht and Ralf Hartmann. Error estimation and anisotropic mesh refinement for 3d laminar aerodynamic flow simulations. *J. Comput. Phys.*, 229(19):7344–7360, September 2010.

[64] Y. Li, Yves Allaneau, and A. Jameson. Continuous adjoint approach for adaptive mesh refinement. *AIAA Paper 2010-3982*, 2010.

[65] Y. Li, S. Premasuthan, and A. Jameson. Comparison of h-and p-adaptations for spectral difference methods. *AIAA Paper 2010-4435*, 2010.

[66] Chunlei Liang, Antony Jameson, and Z. J. Wang. Spectral difference method for compressible flow on unstructured grids with mixed elements. *J. Comput. Phys.*, 228(8):2847–2858, May 2009.

[67] Chunlei Liang, Christopher Cox, and Michael Plesniak. A comparison of computational efficiencies of spectral difference method and correction procedure via reconstruction. *Journal of Computational Physics*, 239(0):138 – 146, 2013.

[68] Chunlei Liang, Koji Miyaji, and Bin Zhang. An efficient correction procedure via reconstruction for simulation of viscous flow on moving and deforming domains. *Journal of Computational Physics*, 256(0):55 – 68, 2014.

[69] Y. Liu, M. Vinokur, and Z. J. Wang. Spectral (finite) volume method for conservation laws on unstructured grids v: extension to three-dimensional systems. *Journal of Computational Physics*, 212(2):454–472, 2006.

[70] G. Lodato and A. Jameson. Les modeling with high-order flux reconstruction and spectral difference schemes. *7th International Conference on Computational Fluid Dynamics, ICCFD7-2201*, 2012.

[71] Guido Lodato, Patrice Castonguay, and Antony Jameson. Discrete filter operators for large-eddy simulation using high-order spectral difference methods. *International Journal for Numerical Methods in Fluids*, 72(2):231–258, 2013.

[72] Rainald Lohner, Ken Morgan, Jaime Peraire, and Mehdi Vahdati. Finite element flux-corrected transport (fem-fct) for the euler and navier-stokes equations. *International Journal for Numerical Methods in Fluids*, 7(10):1093–1109, 1987.

[73] A. Loseille, A. Dervieux, and F. Alauzet. Fully anisotropic goal-oriented mesh adaptation for 3d steady euler equations. *J. Comput. Phys.*, 229(8):2866–2897, April 2010.

[74] James Ching-Chieh Lu. *An a posteriori Error Control Framework for Adaptive Precision Optimization using Discontinuous Galerkin Finite Element Method.* PhD thesis, Massachusetts Institute of Technology, 2005.

[75] H. Luo, L. Luo, R. Nourgaliev, V.A. Mousseau, and N. Dinh. A reconstructed discontinuous galerkin method for the compressible navier–stokes equations on arbitrary grids. *Journal of Computational Physics*, 229(19):6961–6978, 2010.

[76] H. Luo, Luqing Luo, and Robert Nourgaliev. A reconstructed discontinuous galerkin method for the euler equations on arbitrary grids. *Commun. Comput. Phys.*, 12(5):1495–1519, 2012.

[77] Dimitri J MAVRIPLIS. Third drag prediction workshop results using the nsu3d unstructured mesh solver. *Journal of aircraft*, 45(3):750–761, 2008.

[78] G. May and A. Jameson. A spectral difference method for the euler and navier-stokes equations on unstructured meshes. *AIAA paper 2006-304*, 2006.

[79] M.A. Park. Adjoint-based, three-dimensional error prediction and grid adaptation. In *AIAA paper 2002*. Citeseer, 2002.

[80] J. Peraire and P.O. Persson. The compact discontinuous galerkin (cdg) method for elliptic problems. *Arxiv preprint math/0702353*, 2007.

[81] J Peraire, M Vahdati, K Morgan, and O.C Zienkiewicz. Adaptive remeshing for compressible flow computations. *Journal of Computational Physics*, 72(2):449 – 466, 1987.

[82] Marc Van Raalte and Bram Van Leer. Bilinear forms for the recovery-based discontinuous galerkin method for diffusion. *Commun. Comput. Phys.*, 5:683–693, 2009.

[83] W. H. Reed and T. R. Hill. Triangular mesh methods for the neutron transport equation. 1973.

[84] Jochen SchÃŒtz and Georg May. An adjoint consistency analysis for a class of hybrid mixed methods. *IMA Journal of Numerical Analysis*, 2013.

[85] Lei Shi and Z. J. Wang. Adjoint based anisotropic mesh adaptation for the cpr method. *AIAA Paper 2013-2869*, 2013.

[86] Lei Shi and Z. J. Wang. Adjoint based error estimation and hp-adaptation for the high-order cpr method. *AIAA Paper 2013-0999*, 2013.

[87] Lei Shi and Z. J. Wang. Adjoint based anisotropic mesh adaptation for the correction procedure via reconstruction method. *The Eighth International Conference on Computational Fluid Dynamics(ICCFD8)*, 2014.

[88] Lei Shi, Z. J. Wang, Song Fu, and L.P. Zhang. A pnpm-cpr method for navier-stokes equations. *AIAA Paper 2012-460*, 2012.

[89] Lei Shi, Z. J. Wang, L.P. Zhang, Wei Liu, and Song Fu. A pnpm-cpr framework for hyperbolic conservation laws. *Journal of Scientific Computing*, pages 1–27, 2014.

[90] T. Shih and Y. Qin. A posteriori method for estimating and correcting grid-induced errors in cfd solutions–part 1: Theory and method. *AIAA Paper 2007-100*, 2007.

[91] C.-W. Shu. Total-variation-diminishing time discretizations. *SIAM Journal on Scientific and Statistical Computing*, 9(6):1073–1084, 1988.

[92] C.-W. Shu. Essentially non-oscillatory and weighted essentially non-oscillatory schemes for hyperbolic conservation laws. Technical report, 1997.

[93] Haga T, Kuzuu K, Takaki R, and Shima E. Development of a high-order flux reconstruction scheme for body-fitted cartesian unstructured grids. *AIAA Paper 2013-0409*, 2013.

[94] H. Gao T. Haga and Z. J. Wang. A high-order unifying discontinuous formulation for the navier-stokes equations on 3d mixed grids. *Math. Model. Nat. Phenom.*, 6(03):28–56, 2011.

[95] H. TAKAMI and H.B. KELLER. Steady two-dimensional viscous flow of an incompressible fluid past a circular cylinder. *Phys. Fluids Suppl.*, 2(6):51–56, 1969.

[96] M.A. Taylor and Wingate. Several new quadrature formulas for polynomial integration in the triangle. *ArXiv Mathematics e-prints*, January 2005.

[97] D.J. Tritton. Experiments on the flow past a circular cylinder at low reynolds numbers. *Journal of Fluid Mechanics*, 6(6):547–567, 1959.

[98] R. Rannacher V. Heuveline. Duality-based adaptivity in the hp-finite element method. *Journal of Numerical Mathematics*, (2):95–113, 2003.

[99] K. Van den Abeele, C. Lacor, and Z. J. Wang. On the stability and accuracy of the spectral difference method. *Journal of Scientific Computing*, 37(2):162–188, 2008.

[100] Wim M. van Rees, Anthony Leonard, D.I. Pullin, and Petros Koumoutsakos. A comparison of vortex and pseudo-spectral methods for the simulation of periodic vortical flows at high reynolds numbers. *Journal of Computational Physics*, 230(8):2794 – 2805, 2011.

[101] John C Vassberg. Grid generation requirements for accurate drag predictions based on overflow calculations john c. vassberg* phantom works the boeing company. 2003.

[102] David A. Venditti and David L. Darmofal. Adjoint error estimation and grid adaptation for functional outputs: application to quasi-one-dimensional flow. *J. Comput. Phys.*, 164(1):204–227, October 2000.

[103] D.A. Venditti and D.L. Darmofal. Anisotropic grid adaptation for functional outputs: application to two-dimensional viscous flows. *Journal of Computational Physics*, 187(1):22–46, 2003.

[104] David A. Venditti and David L. Darmofal. Anisotropic grid adaptation for functional outputs: application to two-dimensional viscous flows. *J. Comput. Phys.*, 187(1):22–46, May 2003.

[105] P.E. Vincent, P. Castonguay, and A. Jameson. Insights from von neumann analysis of high-order flux reconstruction schemes. *Journal of Computational Physics*, 230(22):8134 – 8154, 2011.

[106] P.E. Vincent, P. Castonguay, and A. Jameson. A new class of high-order energy stable flux reconstruction schemes. *Journal of Scientific Computing*, 47(1):50–72, 2011.

[107] Z. J. Wang and H. Gao. A unifying lifting collocation penalty formulation including the discontinuous galerkin, spectral volume/difference methods for conservation laws on mixed grids. *Journal of Computational Physics*, 228:8161–8186, 2009.

[108] Z. J. Wang and Y. Liu. Spectral (finite) volume method for conservation laws on unstructured grids: Ii. extension to two-dimensional scalar equation. *Journal of Computational Physics*, 179(2):665–697, 2002.

[109] L. Wang and D.J. Mavriplis. Adjoint-based hp adaptive discontinuous galerkin methods for the 2d compressible euler equations. *Journal of Computational Physics*, 228(20):7643–7661, 2009.

[110] Li Wang and Dimitri J. Mavriplis. Adjoint-based h-p adaptive discontinuous galerkin methods for the 2d compressible euler equations. *J. Comput. Phys.*, 228(20):7643–7661, November 2009.

[111] Z. J. Wang, H. Gao, and T. Haga. A unifying discontinuous formulation for hybrid meshes. *Adaptive High-Order Methods in Computational Fluid Dynamics*, page 423, 2011.

[112] Z. J. Wang, Lei Shi, H.X. Zhang, Song Fu, and L.P. Zhang. A pnpm-cpr framework for hyperbolic conservation laws. *AIAA Paper 2011-3227*, 2011.

[113] Z. J. Wang, K. Fidkowski, R. Abgrall, F. Bassi, D. Caraeni, A. Cary, H. Deconinck, R. Hartmann, K. Hillewaert, H. T. Huynh, N. Kroll, G. May, P.-O. Persson, B. van Leer, and M. Visbal. High-order CFD methods: current status and perspective. *International Journal for Numerical Methods in Fluids*, 72:811–845, July 2013.

[114] Z. J. Wang. Spectral (finite) volume method for conservation laws on unstructured grids. basic formulation:: Basic formulation. *Journal of Computational Physics*, 178(1):210–251, 2002.

[115] Z. J. Wang. High-order methods for the euler and navier-stokes equations on unstructured grids. *Progress in Aerospace Sciences*, 43(1-3):1–41, 2007.

[116] Z. J. Wang. *Adaptive High-Order Methods in Computational Fluid Dynamics*, volume 2. World Scientific Pub Co Inc, 2011.

[117] T. Warburton. An explicit construction of interpolation nodes on the simplex. *Journal of engineering mathematics*, 56(3):247–262, 2006.

[118] G.P. Warren, W.K. Anderson, J.L. Thomas, and S. Krist. Grid convergence for adaptive methods. In *10th AIAA Computational Fluid Dynamics Conference*, 1991.

[119] D.M. Williams, P. Castonguay, P.E. Vincent, and A. Jameson. Energy stable flux reconstruction schemes for advection-diffusion problems on triangles. *Journal of Computational Physics*, 250(0):53 – 76, 2013.

[120] Li-Jun Xuan and Jie-Zhi Wu. A weighted-integral based scheme. *J. Comput. Phys.*, 229(17):5999–6014, August 2010.

[121] X. Yang, W. Huang, and J. Qiu. A moving mesh weno method for one-dimensional conservation laws. *SIAM Journal on Scientific Computing*, 34(4):A2317–A2343, 2012.

[122] Masayuki Yano and David L. Darmofal. An optimization-based framework for

anisotropic simplex mesh adaptation. *J. Comput. Phys.*, 231(22):7626–7649, September 2012.

[123] Meilin Yu, Z. J. Wang, and Yen Liu. On the accuracy and efficiency of discontinuous galerkin, spectral difference and correction procedure via reconstruction methods. *Journal of Computational Physics*, 259:70–95, 2014.

[124] X.D. Zhang, M.-G. Vallet, J. Dompierre, P. Labbe, D. Pelletier, and J.-Y. Trepanier. Mesh adaptation using different error indicators for the euler equations. Aiaa paper 2001-2549, 2001.

[125] Laiping Zhang, Wei Liu, Lixin He, and Xiaogang Deng. A class of hybrid dg/fv methods for conservation laws iii: two-dimensional euler equations. *Commun. Comput. Phys.*, 12:284–314, 2012.

[126] Laiping Zhang, Wei Liu, Lixin He, Xiaogang Deng, and Hanxin Zhang. A class of hybrid dg/fv methods for conservation laws i: Basic formulation and one-dimensional systems. *J. Comput. Phys.*, 231(4):1081–1103, February 2012.

[127] Laiping Zhang, Wei Liu, Lixin He, Xiaogang Deng, and Hanxin Zhang. A class of hybrid dg/fv methods for conservation laws ii: Two-dimensional cases. *Journal of Computational Physics*, 231(4):1104–1120, 2012.

ACKNOWLEDGEMENTS

I would like to take this opportunity to thank the many people who made this thesis possible. First and foremost, I would like to express my most sincere thanks to my adviser, Professor Z.J. Wang, for his guidance and support throughout my graduate study. It is my honor being part of his research group. I would like to thank my committee members, Professor Saeed Farokhi, Professor Weizhang Huang, Professor Ray Taghavi, Professor Xuemin Tu and Professor Zhongquan Zheng for their efforts, very useful comments and critical suggestions to this work.

Thanks are also given to my fellow group members Haiyang Gao, Ying Zhou, Takanori Haga, Varun Vikas, Meilin Yu, Yanan Li, Cheng Zhou, Ben Zimmerman, Zhaowen Duan, Jeremy Ims and Feilin Jia for their support and insight provided throughout the years. Special thanks to my families for their support all these years.